

NASA Contractor Report CR-187106

Investigation of Advanced Counterrotation Blade Configuration Concepts for High Speed Turboprop Systems

Task II - Unsteady Ducted Propfan Analysis
Final Report

Edward J. Hall, Robert A. Delaney, and James L. Bettner
Allison Gas Turbine Division of General Motors
Indianapolis, Indiana

May 1991



Prepared for
Lewis Research Center
Under Contract NAS3-25270

(NASA-CR-187106) INVESTIGATION OF ADVANCED
COUNTERROTATION BLADE CONFIGURATION CONCEPTS
FOR HIGH SPEED TURBOPROP SYSTEMS. TASK 2:
UNSTEADY DUCTED PROPFAN ANALYSIS Final
Report (General Motors Corp.) 132 p

N91-25115

Unclass

G3/02 0020327

PAGE ii INTENTIONALLY BLANK

iii

CONFIDENTIAL
UNCLASSIFIED

Preface

This manual was prepared by Edward J. Hall, Robert A. Delaney, and James L. Bettner of the Allison Gas Turbine Division, General Motors Corporation, Indianapolis, IN. The work was performed under NASA Contract NAS3-25270 from March, 1990 to March, 1991. The grid generation, flow code theory, and programming modifications necessary for the analysis of ducted propfans were performed by Edward J. Hall. The Allison program manager for this contract was James L. Bettner. The NASA program manager for this contract was Christopher J. Miller.

Acknowledgements

The authors would like to express their appreciation to the following NASA personnel who contributed to this program:

Mark Celestina for his helpful suggestions concerning the development of the viscous solver.

Dr. John J. Adamczyk for the many helpful technical discussions concerning the development of the computer codes.

Dr. Cristopher J. Miller for his suggestions and critical review of the program.

Dr. David P. Miller for the use of his grid generation code, *TIGGERC*

Christopher E. Hughes for his helpful comments and suggestions

The services of the NASA Numerical Aerodynamic Simulation (NAS) facilities

and personnel are gratefully acknowledged.

UNIX is a trademark of AT&T

IRIS is a trademark of Silicon Graphics, Inc.

UNICOS is a trademark of Cray Computers

PostScript is a trademark of Adobe Systems, Inc.

TABLE OF CONTENTS

NOTATION	xv
1. SUMMARY	1
2. INTRODUCTION	3
3. GRID GENERATION ALGORITHM	9
3.1 Computational Domain	9
3.2 Unducted Propfan Grid Generation	12
3.3 Ducted Propfan Grid Generation	18
4. 3D EULER/NAVIER-STOKES NUMERICAL ALGORITHM .	29
4.1 Nondimensionalization	29
4.2 Governing Equations	30
4.3 Runge-Kutta Time Integration	34
4.4 Fluid Properties	37
4.5 Turbulence Model	37
4.6 Artificial Dissipation	41
4.7 Implicit Residual Smoothing	43
4.8 Boundary Conditions	46

4.9	Multiple-Block Coupling	48
4.10	Solution Procedure	49
5.	RESULTS	51
5.1	SR7 2-Bladed Propfan Modane Tests	52
5.2	SR7 8-Bladed Propfan	68
5.3	Ducted Propfan Test Case	80
5.4	NASA 1.15 Pressure Ratio Fan	87
6.	CONCLUSIONS	109
	REFERENCES	111
	APPENDIX A. <i>ADPAC</i> DISTRIBUTION LIST	115

LIST OF FIGURES

Figure 2.1:	Ducted propfan aerodynamic characteristics	6
Figure 3.1:	Ducted propfan analysis computational domain	11
Figure 3.2:	Meridional plane projection grid generation subregions for an unducted propeller	13
Figure 3.3:	Sample grid for an unducted propfan	19
Figure 3.4:	Axisymmetric plane projection grid generation subregions for a ducted propeller	21
Figure 3.5:	Sample multiple-block C-grid for a ducted propfan	28
Figure 4.1:	Three-dimensional finite volume cell	35
Figure 5.1:	SR7 propfan design characteristics	53
Figure 5.2:	2-bladed SR7 propfan geometry and steady state inviscid cal- culation grid for Modane test comparison	56
Figure 5.3:	2-bladed SR7 propfan geometry and steady state viscous cal- culation grid for Modane test comparison	57
Figure 5.4:	Comparison of predicted and experimental airfoil surface static pressure coefficient distributions for 2-bladed SR7 propfan Modane test (28.4% span)	58

Figure 5.5:	Comparison of predicted and experimental airfoil surface static pressure coefficient distributions for 2-bladed SR7 propfan Modane test (93.1% span)	59
Figure 5.6:	Comparison of predicted and experimental airfoil suction surface static/total pressure ratio contours for 2-bladed SR7 propfan	60
Figure 5.7:	Illustration of predicted turbulent flow leading edge vortex particle trajectory traces for for 2-bladed SR7 propfan . . .	61
Figure 5.8:	Comparison of laminar and turbulent predicted suction surface shear flow patterns and static/total pressure ratio contours for 2-bladed SR7 propfan	62
Figure 5.9:	Comparison of predicted and experimental airfoil surface static/total pressure ratio distributions for 2-bladed SR7 propfan (28.4% span, $M=0.5$, $J=3.06$).	65
Figure 5.10:	Comparison of predicted and experimental airfoil surface static/total pressure ratio distributions for 2-bladed SR7 propfan (94.4% span, $M=0.5$, $J=3.06$).	66
Figure 5.11:	Comparison of predicted and experimental airfoil surface time-dependent static/total pressure ratio history for 2-bladed SR7 propfan (suction side, 4.9% chord, 64.0% span, 3 degrees angle of attack)	69

- Figure 5.12: Comparison of predicted and experimental airfoil surface time-dependent static/total pressure ratio history for 2-bladed SR7 propfan (suction side, 36.7% chord, 64.0% span, 3 degrees angle of attack) 70
- Figure 5.13: Comparison of predicted and experimental airfoil surface time-dependent static/total pressure ratio history for 2-bladed SR7 propfan (pressure side, 4.9% chord, 64.0% span, 3 degrees angle of attack) 71
- Figure 5.14: Comparison of predicted and experimental airfoil surface time-dependent static/total pressure ratio history for 2-bladed SR7 propfan (pressure side, 10.0% chord, 64.0% span, 3 degrees angle of attack) 72
- Figure 5.15: Comparison of predicted and experimental airfoil surface time-dependent static/total pressure ratio history for 2-bladed SR7 propfan (pressure side, 63.3% chord, 64.0% span, 3 degrees angle of attack) 73
- Figure 5.16: Comparison of predicted and experimental airfoil surface time-dependent static/total pressure ratio history for 2-bladed SR7 propfan (suction side, 27.9% chord, 91.0% span, 3 degrees angle of attack) 74

Figure 5.17: Comparison of predicted and experimental airfoil surface time-dependent static/total pressure ratio history for 2-bladed SR7 propfan (suction side, 69.8% chord, 91.0% span, 3 degrees angle of attack)	75
Figure 5.18: Comparison of predicted and experimental airfoil surface time-dependent static/total pressure ratio history for 2-bladed SR7 propfan (pressure side, 27.9% chord, 91.0% span, 3 degrees angle of attack)	76
Figure 5.19: Comparison of predicted and experimental airfoil surface time-dependent static/total pressure ratio history for 2-bladed SR7 propfan (pressure side, 89.8% chord, 91.0% span, 3 degrees angle of attack)	77
Figure 5.20: Instantaneous propfan surface static/total pressure ratio contours and blade tip particle trajectories for 2-bladed SR7 propfan at angle of attack ($M=0.5$, $J=3.06$, angle of attack = 3 degrees).	78
Figure 5.21: Full rotor grid for SR7 time-dependent inviscid calculations .	81
Figure 5.22: Predicted instantaneous propfan inviscid blade passage static pressure contours for 8-bladed SR7 propfan at angle of attack ($M=0.8$)	82
Figure 5.23: Predicted instantaneous propfan surface static/total pressure ratio contours for 8-bladed SR7 propfan at angle of attack ($M=0.8$, angle of attack = 4.6 degrees)	83

Figure 5.24: Predicted rotational single blade power coefficient histories for 8-bladed SR7 propfan at angle of attack ($M=0.8$, angle of attack = 4.6 degrees)	84
Figure 5.25: Full rotor grid system for ducted SR7 propfan geometry . . .	88
Figure 5.26: Instantaneous blade passage static pressure contours for ducted SR7 propfan geometry ($M=0.8$).	89
Figure 5.27: Comparison of time-average and unsteady blade section static pressure distributions for ducted SR7 propfan (90% span). . .	90
Figure 5.28: Predicted surface static pressure contours for ducted SR7 propfan geometry at angle of attack ($M=0.8$).	91
Figure 5.29: Predicted single blade power coefficient rotational histories for ducted and unducted 8-bladed SR7 propfans at angle of attack ($M=0.8$).	92
Figure 5.30: NASA 1.15 pressure ratio fan stage geometry (dimensions in cm)	94
Figure 5.31: NASA 1.15 pressure ratio fan viscous flow grid system	95
Figure 5.32: Predicted cowl surface velocity vectors in the vicinity of the outer surface shock for the NASA 1.15 pressure ratio fan stage geometry ($M=0.85$)	96
Figure 5.33: Comparison of viscous and inviscid predicted and experimental cowl surface leading edge static pressure ratio coefficient distributions for NASA 1.15 pressure ratio fan ($M=0.75$) . .	98

Figure 5.34: Comparison of viscous and inviscid predicted and experimental cowl surface leading edge static pressure ratio coefficient distributions for NASA 1.15 pressure ratio fan ($M=0.85$) . . .	99
Figure 5.35: Full rotor grid system for NASA 1.15 pressure ratio fan . . .	100
Figure 5.36: Predicted viscous instantaneous static pressure contours for NASA 1.15 pressure ratio fan at angle of attack. ($M=0.20$) .	101
Figure 5.37: Comparison of viscous predicted time-averaged and unsteady envelope blade surface static pressure ratio distributions for NASA 1.15 pressure ratio fan at angle of attack (10% span, $M=0.20$)	102
Figure 5.38: Comparison of viscous predicted time-averaged and unsteady envelope blade surface static pressure ratio distributions for NASA 1.15 pressure ratio fan at angle of attack (50% span, $M=0.20$)	103
Figure 5.39: Comparison of viscous predicted time-averaged and unsteady envelope blade surface static pressure ratio distributions for NASA 1.15 pressure ratio fan at angle of attack (90% span, $M=0.20$)	104
Figure 5.40: Comparison of experimental and viscous predicted instantaneous fan face total pressure ratio contours for NASA 1.15 pressure ratio fan ($M=0.2$, angle of attack = 40 degrees). . .	106

Figure 5.41: Comparison of experimental and instantaneous viscous predicted cowl windward side internal static/inlet total pressure ratio distribution for NASA 1.15 pressure ratio fan ($M=0.2$, angle of attack = 40 degrees) 107

LIST OF TABLES

Table 5.1:	Summary of computational characteristics for <i>ADPAC</i> test cases	52
------------	--	----

NOTATION

A list of the symbols used throughout this document and their definitions is provided below for convenience. Parameter values are shown in parentheses.

Roman Symbols

- a ... speed of sound
- c_p ... specific heat at constant pressure
- c_v ... specific heat at constant volume
- e ... internal energy
- i ... z index of numerical solution
- j ... r index of numerical solution
- k ... θ index of numerical solution or thermal conductivity
- l ... turbulence model damping function
- n ... time step index of numerical solution or rotational speed (revolutions/sec)
- \vec{n} ... outward unit normal vector
- p ... pressure
- r ... radius or radial coordinate
- t ... time
- v ... velocity

z ... axial coordinate
 A ... surface area
 A^+ ... turbulence model parameter (26)
 $ADPAC$... Advanced Ducted Propfan Analysis Codes
 AOA ... Angle of Attack aerodynamic analysis code
 $AOAPLOT$... Ducted propfan automated plotting program
 $ASCII$... American Standard Code for Information Interchange
 B ... number of propeller blades
 C_p ... power coefficient ($C_p = P/\rho n^3 D^5$)
 C_t ... thrust coefficient ($C_t = T/\rho n^2 D^4$)
 C_{cp} ... turbulence model parameter (1.6)
 C_{kleb} ... turbulence model parameter (0.3)
 C_{wake} ... turbulence model parameter (0.25)
 CFL ... Courant-Freidrichs-Levy number ($\Delta t/\Delta t_{max,stable}$)
 $CHGRIDV2$... Ducted propfan grid generation code
 D ... dissipation flux vector, turbulent damping parameter, or diameter
 $DELTA$... adjacent cell grid spacing
 $DELTA_{LE}$... adjacent cell grid spacing at leading edge
 $DELTA_{TE}$... adjacent cell grid spacing at trailing edge
 F ... flux vector in z direction or turbulence model function
 G ... flux vector in r direction
 H ... flux vector in θ direction
 H_t ... total enthalpy

J ... advance ratio ($J = U/nD$)
 K ... source term flux vector or turbulence model parameter (0.0168)
 L ... length
 M ... Mach number
 O ... orthogonality
 P ... power
 Pr ... Prandtl number
 $Pr_{turbulent}$... turbulent Prandtl number (0.9)
 Q ... vector of dependent variables
 R ... gas constant or residual or maximum radius
 RAT ... maximum ratio of adjacent cell grid spacings
 $ROTCGRID$... Ducted propfan full rotor grid rotation program
 $ROTCFLOW$... Ducted propfan full rotor flow rotation program
 $SDBLIB$... Scientific DataBase Library (binary file formats)
 S ... arc length or pertaining to surface area normal
 T ... temperature or torque
 U ... flight velocity
 V ... volume

Greek Symbols

α ... time-stepping factor
 β ... local propfan blade angle
 $\beta_{\frac{3}{4}}$... 3/4 radius propfan blade setting angle

ϵ^2	... modified second-order damping coefficient
ϵ^4	... modified fourth-order damping coefficient
ρ	... density
κ^2	... second-order damping coefficient
κ^4	... fourth-order damping coefficient
γ	... specific heat ratio
δ	... spatial second-order central difference operator
λ	... blockage factor
λ_v	... second coefficient of viscosity ($= -\frac{2}{3}\mu$)
μ	... coefficient of viscosity
η	... radial transformed variable
ξ	... axial transformed variable
ζ	... circumferential transformed variable
ν	... damping factor
Υ	... boundary layer dissipation factor
Δ	... increment of change

Special Symbols

∇	... spatial vector gradient operator
Δ	... spatial forward difference operator
∇	... spatial backward difference operator

Superscripts

- $[\overline{\quad}] \dots$ averaged variable
- $[\sim] \dots$ dimensional variable
- $[\hat{\quad}] \dots$ implicitly smoothed variable
- $[\vec{\quad}] \dots$ vector variable
- $[\quad]^* \dots$ intermediate variable
- $[\quad]^n \dots$ time step index of variable

Subscripts

- $[\quad]_{effective} \dots$ effective flow value
- $[\quad]_{i,j,k} \dots$ grid point index of variable
- $[\quad]_{laminar} \dots$ laminar flow value
- $[\quad]_{max} \dots$ maximum value
- $[\quad]_{min} \dots$ minimum value
- $[\quad]_p \dots$ related to pressure
- $[\quad]_{ps} \dots$ pressure (high pressure) surface
- $[\quad]_{ss} \dots$ suction (low pressure) surface
- $[\quad]_t \dots$ total quantity
- $[\quad]_z \dots$ derivative or value with respect to z
- $[\quad]_r \dots$ derivative or value with respect to r
- $[\quad]_\theta \dots$ derivative or value with respect to θ
- $[\quad]_{turbulent} \dots$ turbulent flow value
- $[\quad]_\infty \dots$ freestream value
- $[\quad]_{ref} \dots$ reference value
- $[\quad]_{kleb} \dots$ Klebanoff intermittency factor

[]_{wake} ... turbulent flow wake parameter

[]₂ ... second-order value

[]₄ ... fourth-order value

1. SUMMARY

The primary objective of this study was the development of a time-dependent three-dimensional Euler/Navier-Stokes aerodynamic analysis to predict unsteady compressible transonic flows about ducted and unducted propfan propulsion systems at angle of attack. The computer codes resulting from this study are part of a group of codes referred to as *ADPAC* (Advanced Ducted Propfan Analysis Codes). This document is the final report detailing the development and application of the *ADPAC* codes developed under Task II of NASA Contract NAS3-25270, Unsteady Ducted Propfan Analysis.

Aerodynamic calculations were based on a four-stage Runge-Kutta time-marching finite volume solution technique with added numerical dissipation. A time-accurate implicit residual smoothing operator was utilized for unsteady flow predictions. A single H-type grid was used to discretize each blade passage for unducted propfans. For ducted propfans, a coupled system of five grid blocks utilizing an embedded C-grid about the cowl leading edge were used to discretize each blade passage. Grid systems were generated by a combined algebraic/elliptic algorithm developed specifically for ducted propfans. Numerical calculations were compared with experimental data for both ducted and unducted propfan flows. The solution scheme demonstrated efficiency and accuracy comparable with other schemes of this class.

PRECEDING PAGE BLANK NOT FILMED

2. INTRODUCTION

The development and demonstration of propfan propulsion systems in the last decade can be cited as a prime example of aerodynamic technology which has directly benefitted from the use of computational fluid dynamics (CFD) tools (see Hager and Vrabel [1]). The highly three-dimensional nature of the blade designs do not lend themselves easily to standard two-dimensional design philosophies, and therefore require advanced CFD analysis techniques to verify the performance of candidate designs. Numerical analyses for steady propfan flows in three spatial dimensions have been given by Barton et al. [2], Usab et al. [3], Saito et al. [4], Matsuo et al. [5], Kobayawa and Hatano [6], Celestina et al. [7], Whitfield et al. [8] and others.

Recently, the concept of utilizing a ducted propfan (ultra high bypass fan) as a primary propulsion system has been considered, and has also been an area of intense CFD study. The ducted propfan utilizes the blade design concepts of the unducted propfan, while incorporating a thin profile cowl which aids in maintaining the aerodynamic loading in the blade tip region. An illustration of the aerodynamic characteristics associated with ducted propfans is given in Fig. 2.1. The (efficiency) and bypass ratio (BPR) of a ducted propfan are expected to lie somewhere in between the performance of current high bypass ratio turbofan engines (BPR 4-8) and recent unducted propfan demonstrator engines (BPR 25-40). In addition, ducted propfans

are expected to improve static thrust and acoustic signatures compared to unducted propfans, while permitting more flexible installation configurations.

The advantages of the ducted propfan concept are offset by the additional drag imposed by the relatively large diameter cowl. Accurate prediction of the cowl drag has been the primary factor motivating the study of this concept in the CFD community. A three-dimensional analysis for steady ducted propfan flows was recently presented by Hall and Delaney [9], and Hall et al. [10]. Williams et al. [11] utilized a frequency-domain panel method for predicting both steady and unsteady ducted propfan flows. Unfortunately, their analysis was limited to zero thickness airfoils and ducts, and cannot accurately account for the transonic, vortical nature of high speed ducted propfan flowfields.

With the acceptance of CFD as a design analysis tool, the trend in CFD research has been to examine more demanding flow conditions and provide some insight into the complex flow physics which are often assumed away in the normal design analysis process. In the investigation of propfan aerodynamics, one area of advanced CFD research is aimed at gaining an understanding of the time-dependent velocity and pressure fields generated when the axis of the propeller is inclined at an angle of attack to the incoming freestream. While the freestream flow may be uniform, the flow relative to the rotating blades varies with circumferential position, and the resulting flow is inherently unsteady due to this nonaxial inflow. This is clearly an area of importance since aircraft engine propeller installations rarely operate under ideal (zero incidence angle) conditions. The periodic unsteady flow generated by the angle of attack operation may generate undesirable structural/aerodynamic interactions

and/or unacceptable acoustic noise levels, and therefore must be considered in the design process. Numerical methods for predicting the flow about unducted propfans at angle of attack have been demonstrated by Whitfield et al. [8] and Nallasamy and Groeneweg [12].

This document contains the Final Report for the *ADPAC* (Advanced Ducted Propfan Analysis Codes) 3D Euler/Navier-Stokes aerodynamic and grid generation analyses developed by the Allison Gas Turbine Division of the General Motors Corporation under Task II of NASA Contract NAS3-25270. The objective of this study was to develop a three-dimensional time-dependent Euler/Navier-Stokes analysis for high-speed ducted propfan aircraft propulsion systems operating at angle of attack. This analysis consists of a grid generation scheme coupled with an advanced aerodynamic analysis code. The grid generation scheme is referred to as *ADPAC-CHGRIDV2* or simply *CHGRIDV2*. The aerodynamic analysis is referred to as *ADPAC-AOA* or simply *AOA*. *AOA* utilizes a finite volume multiple-block four-stage Runge-Kutta numerical algorithm to predict the aerodynamics of ducted fan flows. Of particular interest was the ability to accurately predict the unsteady aerodynamics due to the angle of attack, and the complicated viscous flow interactions occurring between the rotating fan and the cowl. The use of a multiple grid block arrangement simplifies the calculation of the full rotor geometry required for angle of attack flows, and permits some unique grid arrangements for complicated ducted propfan geometries.

Unducted propfans are analyzed using a single sheared H-type grid for each blade passage. The analysis for ducted propfans is based on a numerically coupled multiple-block grid arrangement with a body-centered C-type grid about the cowl, surrounded

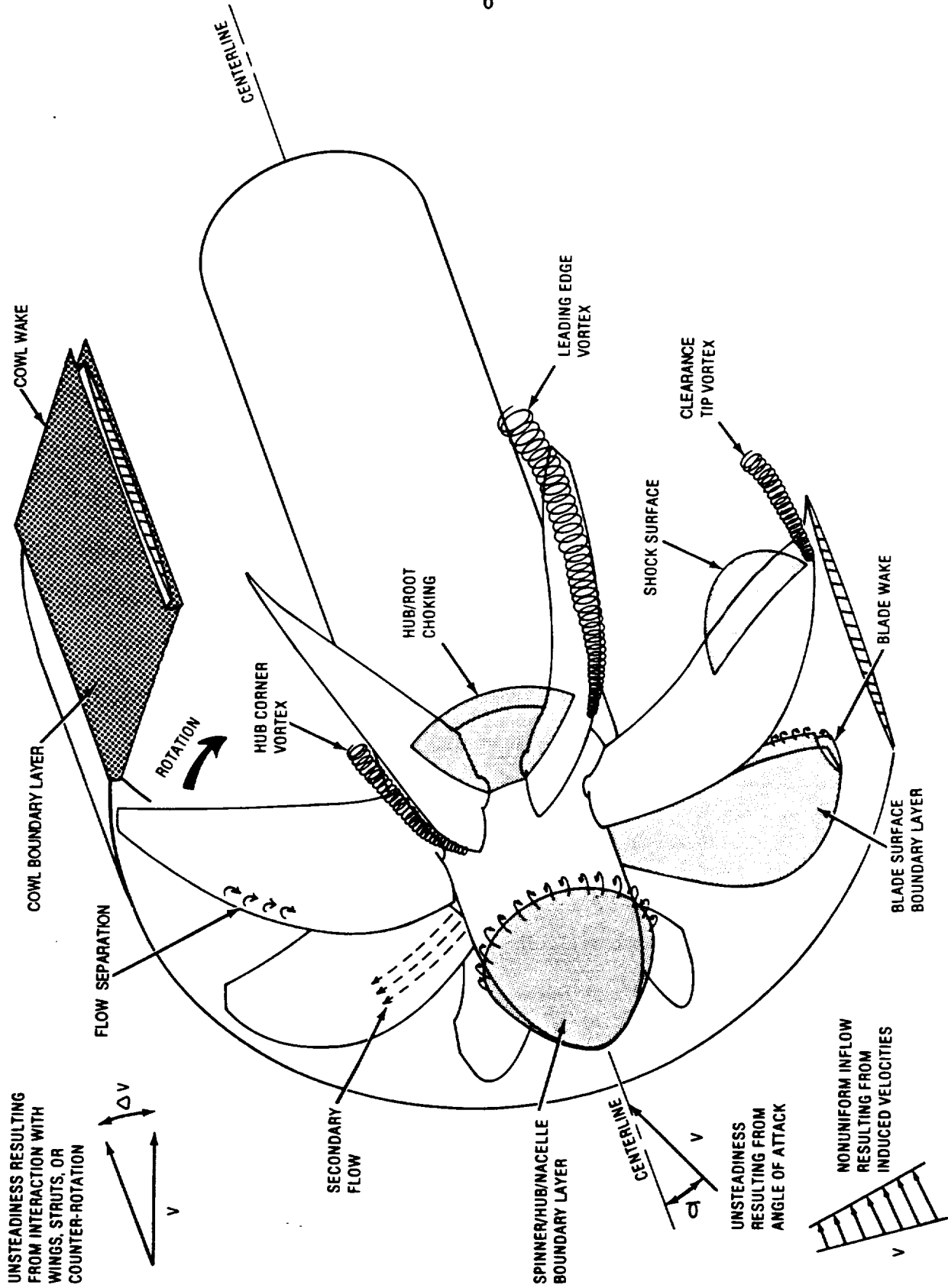


Figure 2.1: Ducted propfan aerodynamic characteristics

by four H-type grid blocks for each blade passage. Predicted results using both grid systems were compared with available experimental data for several cases including a high-speed, high bypass 1.15 pressure ratio fan.

To predict the flow about a ducted propfan at angle of attack using the analyses described in this document, the necessary sequence is:

1. Define the geometry
2. Generate a numerical grid for the domain of interest using *CHGRIDV2*.
3. Run the Euler/Navier-Stokes code *ADPAC-AOA* to predict the steady aerodynamics.
4. Rotate and duplicate the single-passage grid and steady state results using *ADPAC-ROTCGRID* and *ADPAC-ROTCFLOW* to provide full rotor initial data for the unsteady solution.
5. Run the Euler/Navier-Stokes code *ADPAC-AOA* to predict the unsteady aerodynamics.
6. Plot and process the results as needed using *ADPAC-AOAPLOT* or other codes.

Separate sections are provided in the chapters which follow to describe the basis and operation of the codes used in the steps above. A theoretical development of the grid generation algorithms for both ducted and unducted architectures is given in Chapter 2. The 3-D time-marching Euler/Navier-Stokes analysis is detailed in Chapter 3. In Chapter 4, a summary of the predicted results and verification studies

performed to validate the accuracy of the analysis is presented. A summary of the conclusions of this study is given in Chapter 5.

It is worthwhile mentioning that the development and application of the codes described in this manual were performed on UNIX-based computers. All files are stored in machine-independent format. Small files utilize standard ASCII format, while larger files, which benefit from some type of binary storage, are written in a machine-independent format through the Scientific DataBase Library (SDBLIB) routines [13]. The SDBLIB format utilizes machine-dependent input/output routines which permit machine independence of the binary data file. The SDBLIB routines are under development at the NASA Lewis Research Center.

Most of the plotting and graphical postprocessing of the solutions was performed on graphics workstations. Presently, the *PLOT3D* [14], *SURF* [15], and *FAST* [16] graphics software packages developed at the NASA Ames Research Center are being extensively used for this purpose, and plot output has been tailored for this software. In addition, due to the increasing popularity of the *PostScript* page description language, and the variety of devices which can display *PostScript*-based output, a number of plotting procedures included in the *ADPAC* package utilize standard *PostScript* routines.

3. GRID GENERATION ALGORITHM

In this chapter, the numerical algorithm forming the basis of the ducted/unducted propfan analysis grid generation scheme is described. The geometry and computational domain are briefly described in the first section below.

3.1 Computational Domain

The problem of interest is either a ducted or unducted propfan geometry operating at angle of attack, as shown in Fig 3.1. Geometric parameters are expressed in a cylindrical coordinate system referenced to the propfan axis. The axial coordinate lies along the propeller axis of rotation, the radial coordinate is perpendicular to the axis of rotation, and the circumferential coordinate sweeps in the counter-clockwise direction when viewed down the axis of rotation (i.e. looking downstream). This coordinate system is illustrated in Fig. 3.1. The hub and duct contours are assumed to be axisymmetric surfaces (no circumferential variation). This is presently a limitation of the grid generation scheme only. The aerodynamic analysis can be applied to nonaxisymmetric duct geometries presuming a suitable grid system can be generated. It is further assumed that the airfoil tips are fully enclosed within the duct for ducted configurations (although this limitation could be easily relaxed). For steady flow and

a periodic geometry, the computational domain may be reduced to a single blade passage, circumferentially, as shown in Fig. 3.1. The problem is further simplified by fixing the computational domain to the rotating blade elements. The resulting flow predictions are therefore based on the steady flow relative to the rotating blade. At angle of attack, however, we no longer expect the flow to be spatially periodic with respect to the blade pitch (circumferential spacing), and therefore the computational domain must be expanded to include the entire propfan.

In order to implement a finite volume numerical solution of the unsteady aerodynamics for a complete rotor system, the flowpath must be subdivided into a finite number of smaller elements within the overall region of interest. To enhance the quality of the numerical solution, we further specify that these subdivisions be constructed in a relatively smooth and orderly manner with some arbitrary limitation on both the relative spacing between cells and the total number of cells in the computational domain. Each of these subdivisions will be used to define an elemental computational cell which will form the geometric basis of the finite volume aerodynamic solver to be described in a later chapter.

The methods by which the computational cells are constructed differs slightly for ducted and unducted propfans. Unducted propfans utilize a single H-type grid per blade passage. This grid is then duplicated circumferentially to construct a multiple-grid block system for the complete rotor. Ducted propfans utilize a coupled system of five grid blocks per blade passage. An embedded C-type grid is wrapped about the leading edge of the cowl to enhance the resolution and accuracy of the aerodynamic predictions in this critical area. The C-type grid is surrounded by a network of

Ducted Propfan Analysis Computational Domain

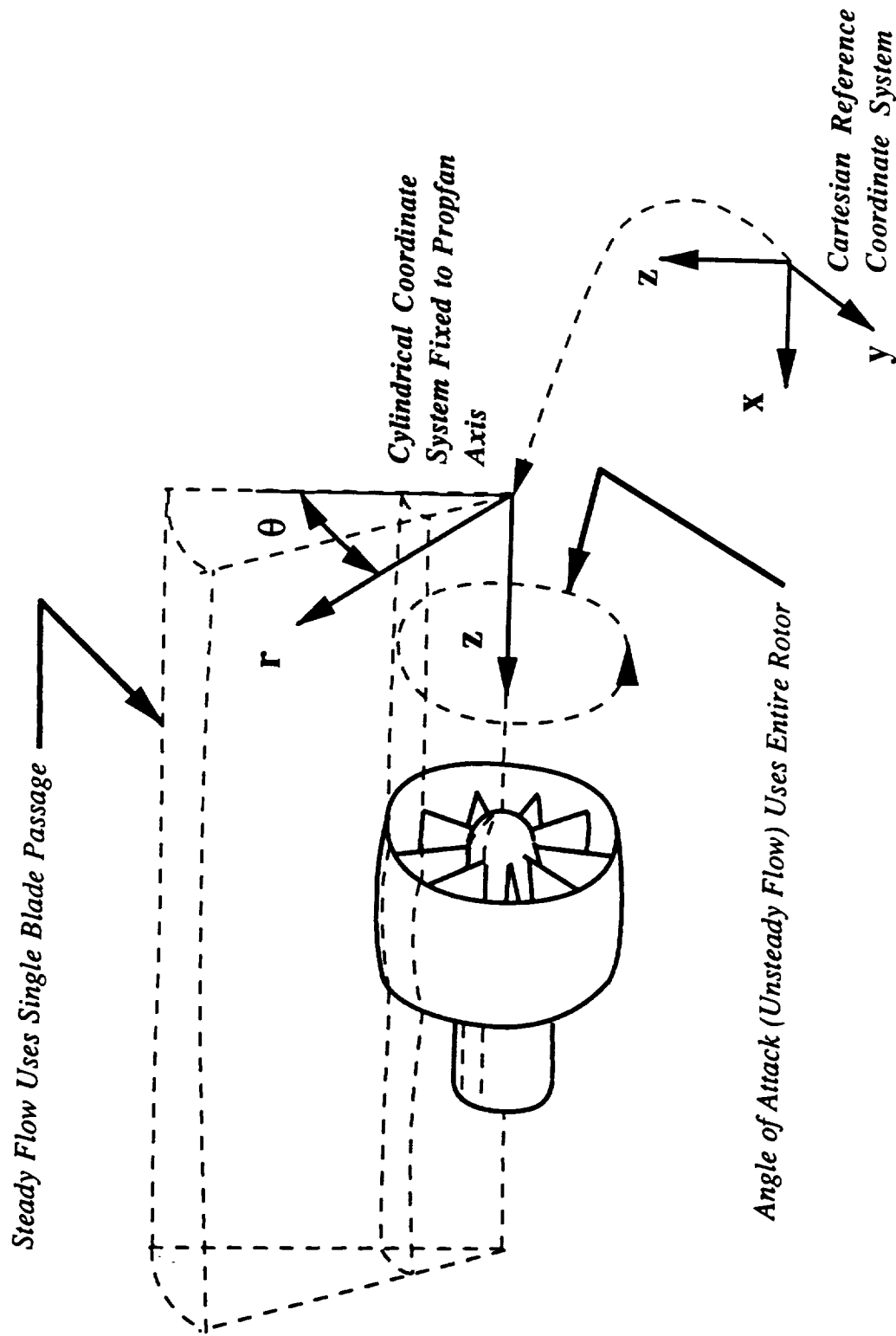


Figure 3.1: Ducted propfan analysis computational domain

four H-type grids which connect the inner C-grid to the outer computational domain boundaries. Separate sections are provided below to illustrate the details of the grid generation sequence for both unducted and ducted propfan geometries.

3.2 Unducted Propfan Grid Generation

The grid generation scheme for unducted propfans is based on a procedure originally developed by Mulac [17]. The approach here is to first construct a two-dimensional axisymmetric mesh in the meridional (z, r) plane, followed by a separate construction in the circumferential direction to determine the final three-dimensional mesh.

The two-dimensional axisymmetric mesh is constructed by dividing the meridional plane into several subregions as shown in Fig. 3.2 for an unducted propfan. The regions of interest include the inlet, blade, exit, and outer flow regions. These regions are individually gridded in the two-dimensional plane to satisfy the conditions of common grid points along region interface boundaries, and a suitable distribution of points within each region.

The various regions differed in their individual construction. The distribution of points in any region is given axially and radially by one of three point distribution routines. These routines are described in the paragraphs below. All interpolations of coordinates were performed using spline interpolation routines.

The distribution of the points on the meridional blade plane in both the radial and axial directions is determined by a simple geometric progression radiating from a symmetric centerline referred to as packing algorithm #1 described below.

Unducted Propfan H-Grid Generation Subregions

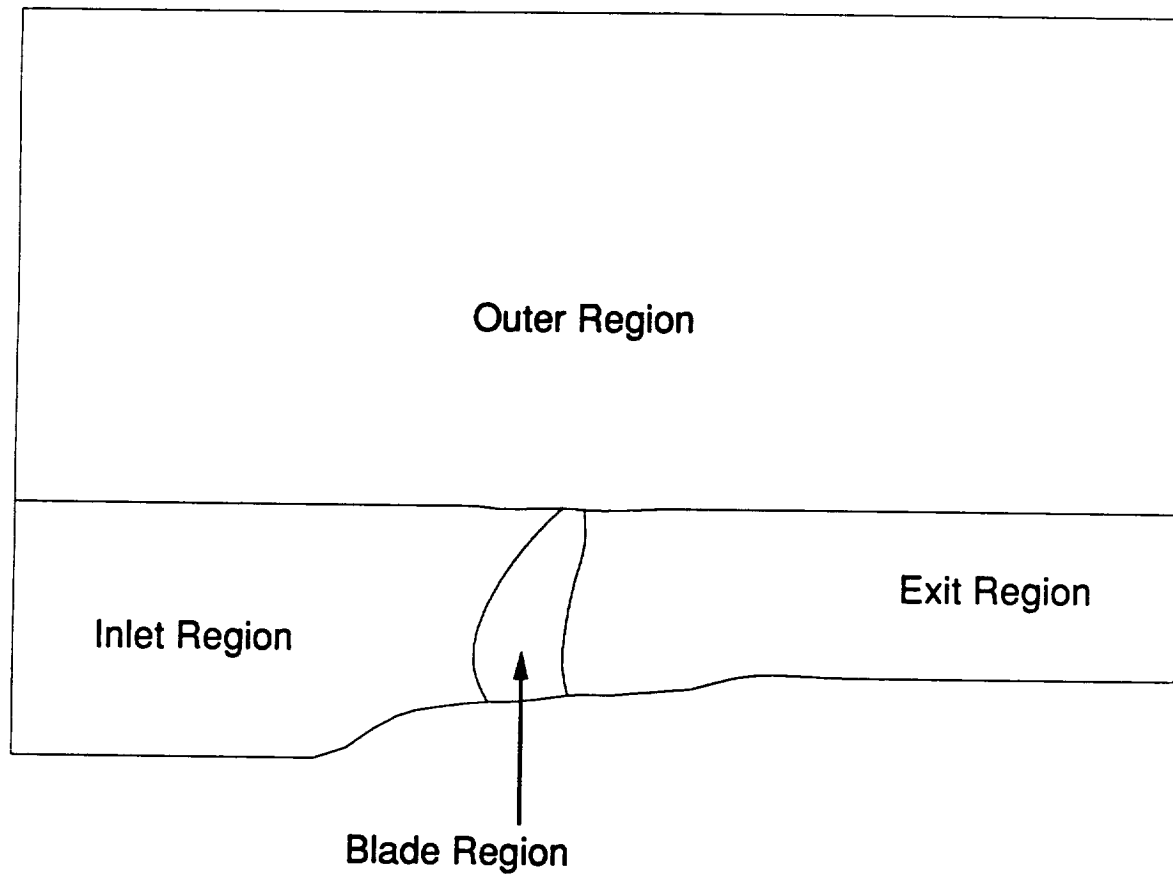


Figure 3.2: Meridional plane projection grid generation subregions for an unducted propeller

Packing algorithm #1

This algorithm packs the mesh at both ends of the point distribution based only on RAT .

Given:

D total projected length of cubic spline curve

RAT ratio of adjacent cell projected lengths

M number of points distributed across D (must be odd)

the initial cell length of the progression is calculated as

$$DEL T = \frac{\frac{D}{2}}{\sum_{i=1}^{(M/2)+1} (RAT)^i} \quad (3.1)$$

The point distribution is then given by

$$P(i) = \sum_{j=2}^i (DEL T)(RAT)^{(j-1)}; \quad i = 2, (M/2) + 1 \quad (3.2)$$

The remaining points ($i = (M/2) + 2, M$) are determined from the known symmetry of the point distribution.

Packing algorithm #2

The second construction utilizes a slightly different packing algorithm. This algorithm packs the mesh either at the initial end of the point distribution ($RAT > 1$) or at the terminal end ($RAT < 1$). In this case, D , RAT , and $DEL T$ are specified along with N , the total number of curves in the region upon which the points are to

be distributed, leaving M to be determined. The value of M is calculated iteratively until the the following conditions are satisfied:

$$\left(\frac{D}{DEL T}\right)_{max} = \sum_{i=1}^M (RAT)^i$$

$$\left(\frac{D}{DEL T}\right)_{min} = \sum_{i=1}^M (RAT)^{-i}$$

where

$$\left(\frac{D}{DEL T}\right)_{max} = \max \left(\frac{D}{DEL T}\right)_{j=1,N}$$

$$\left(\frac{D}{DEL T}\right)_{min} = \min \left(\frac{D}{DEL T}\right)_{j=1,N} \quad (3.3)$$

These conditions guarantee that neither the adjacent cell ratios, nor their inverses, exceed RAT . The resulting point distribution is then given by

$$P(i) = \sum_{j=2}^i (DEL T)(RAT)^j, 2 = 1, M \quad (3.4)$$

This approach is used axially in the inlet and exit regions, and radially in the outer boundary region.

Packing algorithm #3

The third packing algorithm is used to determine the axial point distribution between blade rows. This algorithm packs the mesh at both ends of the point distribution based on RAT and a given initial spacing at each end. The packing is denser at the ends for $RAT > 1$, and denser in the middle for $RAT < 1$.

Given:

D total projected length of cubic spline curve

RAT maximum ratio of adjacent cell projected lengths

DELTTE initial cell width (forward blade row trailing edge)

DELTLE initial cell width (aft blade row leading edge)

N total number of curves upon which the points are to be distributed

the following values are then calculated:

$$DTE = \left(\frac{DELTTE}{DELTTE + DELTLE} \right) D \quad (3.5)$$

$$DLE = \left(\frac{DELTLE}{DELTTE + DELTLE} \right) D \quad (3.6)$$

The value of *M* is determined iteratively until the following conditions are satisfied:

$$\left(\frac{D}{DELT} \right)_{max} \leq \sum_{i=1}^M RAT^i \quad (3.7)$$

$$\left(\frac{D}{DELT} \right)_{min} \geq \sum_{i=1}^M RAT^{-i} \quad (3.8)$$

where:

$$\left(\frac{D}{DELT} \right)_{max} = max \left(\frac{DTE}{DELTTE} \right) \left(\frac{DLE}{DELTLE} \right), j = 1, N \quad (3.9)$$

$$\left(\frac{D}{DELT} \right)_{min} = min \left(\frac{DTE}{DELTTE} \right) \left(\frac{DLE}{DELTLE} \right), j = 1, N \quad (3.10)$$

Again, this ensures that neither the adjacent cell ratios, nor their inverses exceed *RAT*. The point distribution is then given from the two ends of the curve by:

$$P(i) = \sum_{j=1}^i (DELTTE)(RAT)^j, \quad i = 1, M \quad (3.11)$$

$$P(2 * M - 1 - l) = D - \sum_{j=1}^l (DELTLE)(RAT)^j, \quad l = 1, M \quad (3.12)$$

The blade region is generated initially. This region is defined by the axisymmetric projection of the blade hub and tip boundaries, and the blade leading and trailing edges. The number of points defining the blade region axially and radially is directly specified by the user. The point distributions are determined by packing algorithm #1. Once the blade points are determined, the inlet region pictured in Fig. 3.2 is computed next using packing algorithm #2. The exit region is constructed in the same manner as the inlet region. Finally, the radial distribution of points in the outer region is determined from packing algorithm #2. Once the meridional plane grid has been calculated, the full three-dimensional grid is constructed. The blade twist and thickness distributions are used to determine the circumferential coordinates for the blade regions. The remaining circumferential coordinates are based on utilizing packing algorithm #1 in the blade-to-blade plane. The circumferential variation of grid points upstream and downstream of the blade regions is adjusted to provide a smooth transition such that the grid lines become parallel to the axis of rotation away from the blade region.

A sample grid for an unducted propfan based on this grid generation technique is given in Fig. 3.3. Once the grid for a single blade passage has been constructed, it is a simple matter to duplicate and rotate this grid circumferentially to complete the construction of the full rotor. The total number of grid blocks in this case is N , where N represents the number of rotor blades. Again, this clearly implies an axisymmetric hub surface, although the aerodynamic analysis does not require this limitation.

The emphasis in this development, as in Mulac [17], was to maintain a reasonable grid quality, rather than a specific number of grid points. Due to the algebraic

nature of the scheme, the construction is performed relatively easily and inexpensively. Unfortunately, this approach can have drawbacks under certain conditions. Since a portion of the grid generation sequence involves finding the intersection of two arbitrary curves, it has been observed that this can produce unexpected results when the two curves in question have nearly identical slopes near their intersection point. In some cases, it is possible to generate curves which have no intersection, and the grid generation scheme will clearly fail. In addition, blades or cowls with thick or blunt leading edges may not be well represented by this scheme when a relatively low number of grid points is used. Finally, the construction may occasionally have limits based on the number of grid points in a particular region due to the inability to satisfy one or more of the adjacent cell ratio constraints in the packing algorithms. In spite of these drawbacks, for most problems involving relatively conventional geometries, this approach has been found to be more than adequate.

3.3 Ducted Propfan Grid Generation

The grid generation scheme for ducted propfans utilizes a number of concepts developed in the previous section relating the construction of grids for unducted propfans. Again, the mesh for a single blade passage is generated by first constructing a two-dimensional grid in the meridional plane. For ducted propfans, a slightly different subdivision approach is utilized. Fig. 3.4 illustrates the boundaries of the various subregions used in the construction of the grids for ducted propfan geometries. The overall grid system consists of five separate grid blocks as shown by the thick lines defining the block boundaries. A single body-centered C-type grid is wrapped about

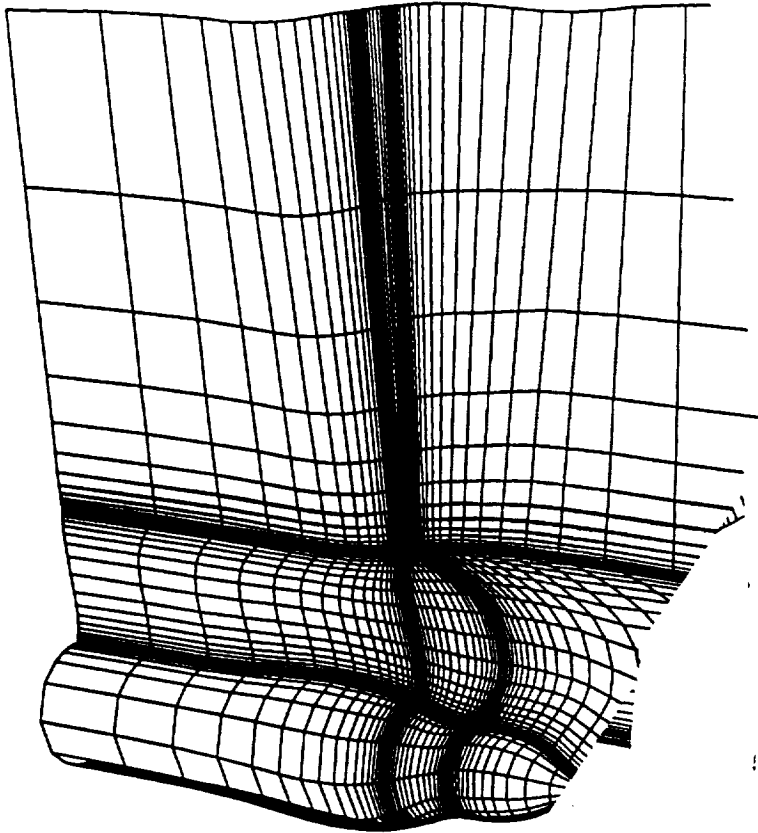


Figure 3.3: Sample grid for an unducted propfan

the leading edge of the cowl, represented by Block #3 in Fig. 3.4. The use of the body-centered grid is advantageous in that the grid skewness normally associated with simple sheared H-type grid systems in the vicinity of the cowl leading edge can be eliminated. The remaining four blocks (#1, #2, #4, and #5) are H-type grids which surround the C-type grid and connect the inner grid to the outer boundaries of the computational domain. Several of the subdomains of the individual grid blocks are similar to those used in the unducted propfan grid construction, so the extension of the algorithm for ducted propfans is obvious. The blade, mid-inlet, inlet, mid-exit, exit, and outer regions are all constructed in basically the same manner for the C-grid as they were for the H-grid. In this case, the axial locations of the upstream boundary of the mid-inlet and the downstream boundary of the mid-exit regions are specified as a fraction of the cowl axial chord upstream and downstream of the cowl leading and trailing edges, respectively. The outer boundary for the C-grid (block #3) and the upstream and downstream H-grids (blocks #2 and #4) is created from a line displaced from the outer surface of the cowl by an amount equal to the average of the blade leading edge and trailing edge tip gaps. This line is extended upstream and downstream at the radius of the ends. The near-cowl region is then discretized by the C-grid as shown in Fig. 3.4. The construction of blocks 1, 2, 4, and 5 follows directly from the development of the subregion grids for unducted propfans, so no further discussion is presented here. Instead, the underlying algorithm for the C-grid (block 3) is presented in the paragraphs below.

Grid points for the C-grid block surrounding the cowl are determined in a three-step procedure. In the first step, the inner and outer boundary points are specified.

Ducted Propfan Multiple-Block C-Grid Subregions

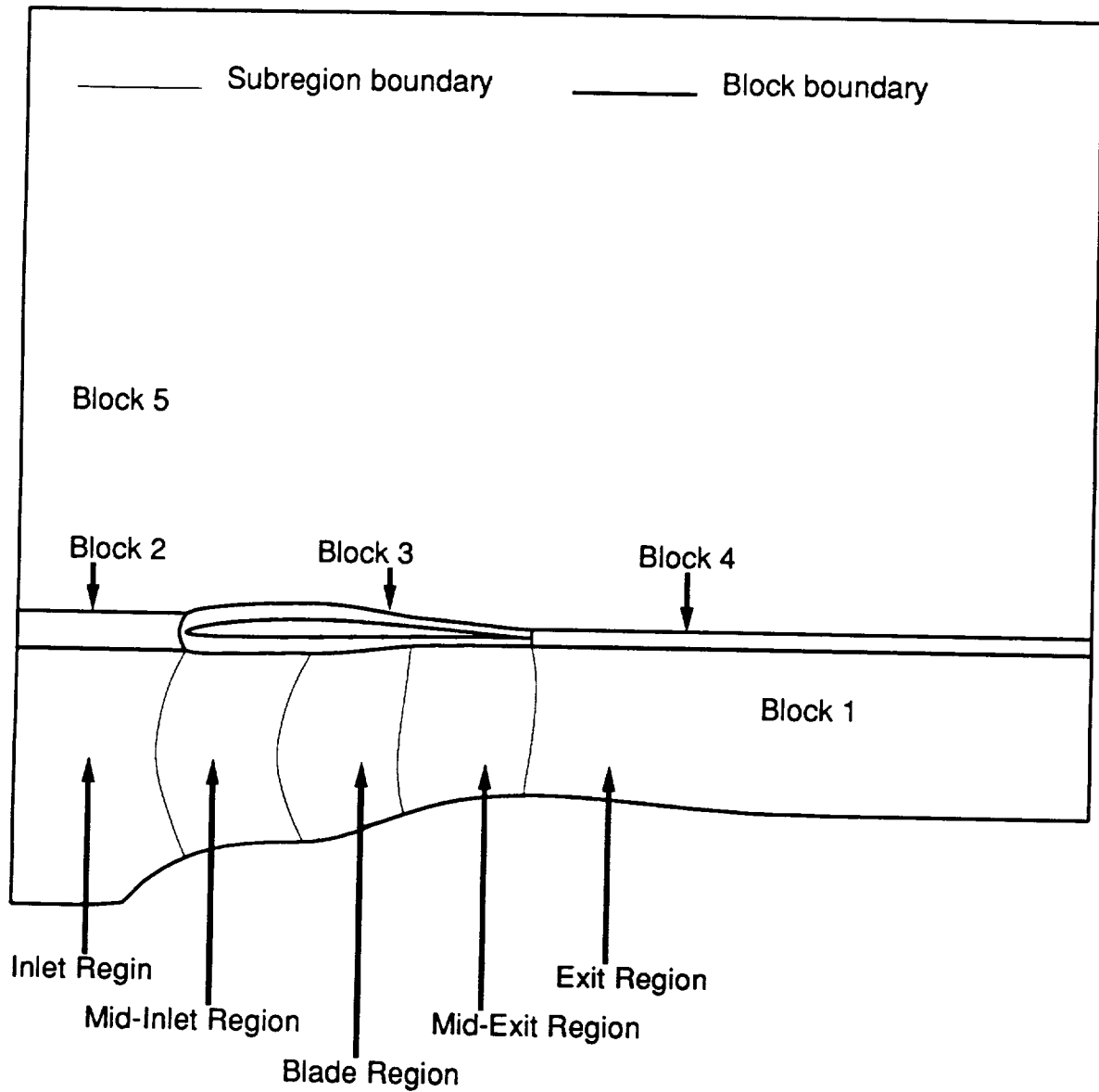


Figure 3.4: Axisymmetric plane projection grid generation subregions for a ducted propeller

In the second step, the interior points are determined. In the third step, the interior grid points are clustered near the surface of the cowl to adequately resolve the cowl boundary layer for viscous flow calculations. Each step has several options each of which is described below.

The outer boundary points of the C-grid are determined by the surrounding four blocks. This is based on the requirement of coincident points along all block boundaries. The number of points along the upstream plane of the C-grid is determined by twice the number of radial grid lines in the C-grid (NPBCAB) plus one. The number of points from the cowl surface to the outer boundary of the C-grid (NPBCAB) is specified by the user, which also fixes the number of points along the C-grid block exit plane. The cowl surface points are determined through one of two procedures. The first method performs a simple interpolation of the input coordinates based on arc length around the cowl such that the relative arc length distributions of the cowl surface points and the corresponding outer boundary points are the same. Unfortunately, this can often lead to highly skewed mesh lines near the cowl surface. To circumvent this problem, an option was provided which allows the cowl surface grid points to "float" along the contour of the cowl in a manner that would impose orthogonality at the cowl surface to a line extending from the cowl point to the corresponding outer boundary point. The movement of the cowl surface grid points is controlled by a secant iteration procedure which optimizes the orthogonality of the surface grid point location as a function of arc length along the cowl, while maintaining a smooth transition through neighboring surface grid points. The new cowl coordinates are determined from the updated value of arc length through a linear interpolation of the

arc length and cowl coordinates originally specified. The resulting grid thus possesses improved orthogonality characteristics along the cowl contour, which is desirable in terms of solution accuracy.

The secant iteration procedure described above for the cowl surface grid points is expressed as:

$$S_i^{k+1} = S_i^k + \frac{(0.0 - O_i^k)(S_i^k - S_i^{k-1})}{(O_i^k - O_i^{k-1})} \quad (3.13)$$

where S_i is arc length measured clockwise around the cowl from a fixed reference location (1) to the point (i), k is the secant iteration count, and O_i is the measure of nonorthogonality. The orthogonality measure was based on the change of arc length S_{grid} between the outer point and the corresponding inner point. The optimized point occurs when $O_i = dS_{grid}/dS^k = 0$.

The starting values for the secant iteration are determined by using an initial point distribution obtained from the cowl surface grid point distribution scheme based on arc length (the first method described above).

In order to avoid overlapping grid lines and to maintain stability, the new surface grid point locations were never allowed to migrate more than one third of the distance between the original point and the neighboring grid points.

The interior grid points of the C-grid are determined through one of two methods. The first method is a simple algebraic interpolation of coordinates between the inner and outer C-grid boundary point distributions. In the second method, the interior points are generated through the numerical solution of a set of elliptic equations controlling a weighted distribution of grid smoothness, orthogonality, and grid point density based on a variational formulation originally developed by Brackbill

and Saltzman [18]. A brief description of this scheme is given below.

For a two-dimensional grid, the following integral expressions may be derived to evaluate critical aspects of the overall grid quality in physical space:

Grid smoothness:

$$I_s = \int \int [(\nabla \xi)^2 + (\nabla \eta)^2] dz dr \quad (3.14)$$

Grid orthogonality:

$$I_o = \int \int [(\nabla \xi) \cdot (\nabla \eta)] dz dr \quad (3.15)$$

Grid point density:

$$I_w = \int \int w(z, r) J dz dr \quad (3.16)$$

where:

$$\xi = \xi(z, r) \quad \eta = \eta(z, r) \quad (3.17)$$

$$J = \frac{\partial(\xi, \eta)}{\partial(z, r)} \quad (3.18)$$

and where ∇ is the Cartesian gradient vector operator. The term $w(z, r)$ is a user-specified function the magnitude of which is proportional to the desired grid point density in physical space.

Obviously, the smoothest possible grid is obtained when I_s is minimized, the most orthogonal grid is obtained when I_o is minimized, and the grid with the most desirable point density is obtained when I_w is minimized. By minimizing a weighted sum of these terms, i.e:

$$I = I_s + C_o I_o + C_w I_w \quad (3.19)$$

the constants C_o, C_w may be used to control the relative importance of orthogonality and point density, respectively, in the overall grid point distribution. By exchange-

ing dependent and independent variables, and applying the concepts of variational calculus for minimizing functions using the Euler-Lagrange equations, the following nonlinear coupled set of equations results:

$$b_1 z_{\xi\xi} + b_2 z_{\xi\eta} + b_3 z_{\eta\eta} + a_1 r_{\xi\xi} + a_2 r_{\xi\eta} + a_3 r_{\eta\eta} = -J^2 \frac{1}{2w} \frac{\partial w}{\partial z} \quad (3.20)$$

$$a_1 z_{\xi\xi} + a_2 z_{\xi\eta} + a_3 z_{\eta\eta} + c_1 r_{\xi\xi} + c_2 r_{\xi\eta} + c_3 r_{\eta\eta} = -J^2 \frac{1}{2w} \frac{\partial w}{\partial r} \quad (3.21)$$

where the coefficients $(a_i, b_i, c_i, i = 1, 3)$ are all functions of the coordinate derivatives as:

$$\begin{aligned} a_1 &= a_{s1} + C_o a_{o1} + C_w a_{v1} \\ a_2 &= a_{s2} + C_o a_{o2} + C_w a_{v2} \\ a_3 &= a_{s3} + C_o a_{o3} + C_w a_{v3} \\ b_1 &= b_{s1} + C_o b_{o1} + C_w b_{v1} \\ b_2 &= b_{s2} + C_o b_{o2} + C_w b_{v2} \\ b_3 &= b_{s3} + C_o b_{o3} + C_w b_{v3} \\ c_1 &= c_{s1} + C_o c_{o1} + C_w c_{v1} \\ c_2 &= c_{s2} + C_o c_{o2} + C_w c_{v2} \\ c_3 &= c_{s3} + C_o c_{o3} + C_w c_{v3} \end{aligned} \quad (3.22)$$

where:

$$\begin{aligned} a_{s1} &= -(aa)\alpha, & a_{s2} &= 2(aa)\beta, & a_{s3} &= -(aa)\gamma \\ b_{s1} &= (bb)\alpha, & b_{s2} &= -2(bb)\beta, & b_{s3} &= (bb)\gamma \\ c_{s1} &= (cc)\alpha, & c_{s2} &= -2(cc)\beta, & c_{s3} &= -(cc)\gamma \end{aligned}$$

$$\begin{aligned}
a_{o1} &= z\eta r\eta, & a_{o2} &= z\xi r\eta + z\eta r\xi, & a_{o3} &= z\xi r\xi \\
b_{o1} &= z\eta^2, & b_{o2} &= 2(2z\xi z\eta + r\xi r\eta), & b_{o3} &= z\xi^2 \\
c_{o1} &= r\eta^2, & c_{o2} &= 2(z\xi z\eta + 2r\xi r\eta), & c_{o3} &= r\xi^2 \\
a_{v1} &= -z\eta r\eta, & a_{v2} &= z\xi r\eta + z\eta r\xi, & a_{v3} &= -z\xi r\xi \\
b_{v1} &= r\eta^2, & b_{v2} &= -2r\xi r\eta, & b_{v3} &= r\xi^2 \\
c_{v1} &= z\eta^2, & c_{v2} &= -2z\xi r\eta, & c_{v3} &= z\xi^2 \\
(aa) &= z\xi r\xi + z\eta r\eta, & (bb) &= r\xi^2 + r\eta^2, & (cc) &= z\xi^2 + z\eta^2 \\
\alpha &= (x\eta^2 + y\eta^2)/J^3, & \beta &= (x\xi x\eta + y\xi y\eta)/J^2, & \gamma &= (x\xi^2 + y\xi^2)/J^3
\end{aligned} \tag{3.23}$$

When $C_o = 0$ and $C_w = 0$ the standard Laplace grid generation scheme results. This system is more complex than the usual Laplace-based grid generation schemes [19], but is still solvable using standard relaxation techniques. In this case, an iterative successive overrelaxation Gauss-Seidel solution technique is applied to solve the finite-difference equations resulting from a second-order central-difference approximation of the resulting equations. For example:

$$x_{\xi\xi} \approx \frac{x_{i+1,j} - 2x_{i,j} + x_{i-1,j}}{(\Delta\xi)^2} \tag{3.24}$$

$$x_{\xi\eta} \approx \frac{x_{i+1,j+1} - x_{i+1,j-1} + x_{i-1,j-1} - x_{i-1,j+1}}{(\Delta\xi\Delta\eta)} \tag{3.25}$$

Normally, the recommended approach is to set $C_o, C_w = 0$ which effectively reduces the scheme to a Laplace solver. The additional complexity of the variational approach is presented here for completeness, but has not been found to be particularly useful for the present applications.

Once the interior points of the C-grid have been generated through the sequence just described, a reinterpolation of grid coordinates is performed along grid lines normal to the cowl surface to provide mesh clustering about the cowl for viscous flow calculations. The clustering is based on a one-sided Roberts transformation (see e.g. [20]). The initial grid distribution is used as the basis for the interpolation performed during the mesh clustering process. All interpolations are based on arc length S along a given grid line emanating from the cowl surface. Given the distribution of coordinates (z, r) along a given grid line, and the corresponding arc length distribution S , the clustered distribution of coordinates is determined as:

$$S_j = S_{jmax} \frac{(\beta + 1) - (\beta - 1)[(\beta + 1)/(\beta - 1)]^{1-\bar{j}}}{[(\beta + 1)/(\beta - 1)]^{1-\bar{j}} + 1} \quad (3.26)$$

where β is a user-specified parameter which controls the amount of clustering ($\beta \geq 1$, more clustering as β approaches 1), $\bar{j} = j/j_{max}$ where j is the numerical index of a particular point, and j_{max} is the maximum numerical index of the grid normal to the cowl surface. A corresponding reinterpolation of points is also performed for grid block #4 to maintain the continuity of grid points across the block boundary separating blocks #3 and #4.

A sample multiple-block C-grid mesh network is shown in Fig. 3.5 for a ducted propfan geometry.

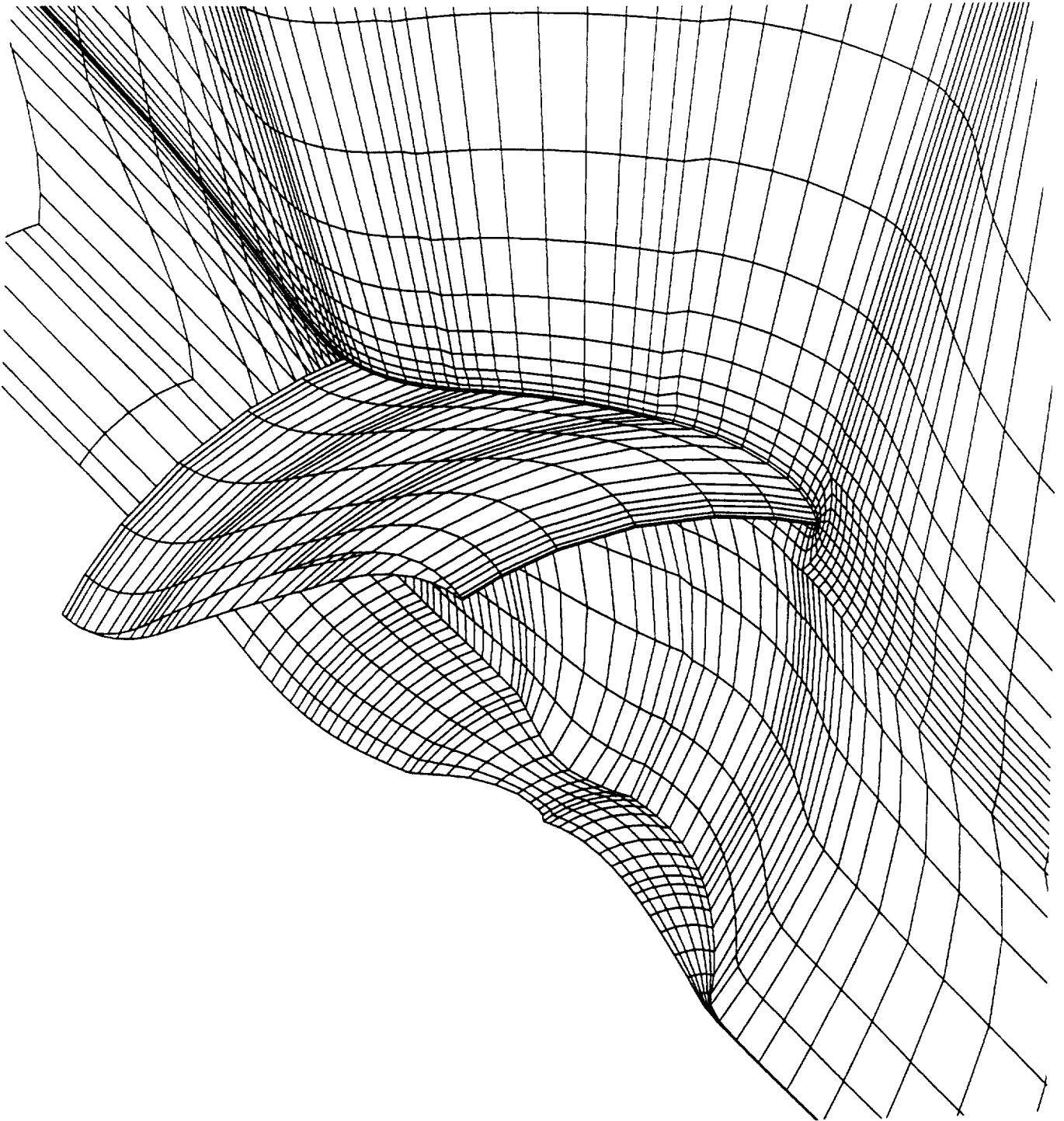


Figure 3.5: Sample multiple-block C-grid for a ducted propfan

4. 3D EULER/NAVIER-STOKES NUMERICAL ALGORITHM

This chapter contains a description of the time-dependent multiple-grid block Euler/Navier-Stokes ducted propfan aerodynamic analysis. The definitions of the pertinent variables used in this chapter may be found in the Nomenclature.

4.1 Nondimensionalization

To simplify the numerical treatment, all variables in the numerical solution are nondimensionalized by reference values as follows:

$$\begin{aligned}
 z &= \frac{\tilde{z}}{L_{ref}}, & r &= \frac{\tilde{r}}{L_{ref}}, & v_z &= \frac{\tilde{v}_z}{v_{ref}}, & v_r &= \frac{\tilde{v}_r}{v_{ref}}, & v_\theta &= \frac{\tilde{v}_\theta}{v_{ref}} \\
 p &= \frac{\tilde{p}}{p_{ref}}, & \mu &= \frac{\tilde{\mu}}{\mu_{ref}}, & c_p &= \frac{\tilde{c}_p}{R_{ref}}, & c_v &= \frac{\tilde{c}_v}{R_{ref}}, & k &= \frac{\tilde{k}}{k_{ref}} \\
 T &= \frac{\tilde{T}}{T_{ref}}, & \rho &= \frac{\tilde{\rho}}{\rho_{ref}}, & \omega &= \frac{\tilde{\omega} L_{ref}}{v_{ref}}
 \end{aligned} \tag{4.1}$$

The reference quantities are defined as follows:

L_{ref} is the maximum diameter of the propfan blade

p_{ref} is the freestream relative total pressure

ρ_{ref} is the freestream relative total density

a_{ref} is determined from the freestream relative total conditions

$$= \sqrt{\gamma p_{ref} / \rho_{ref}}$$

v_{ref} is determined from the freestream acoustic velocity as

$$v_{ref} = \frac{a_{ref}}{\sqrt{\gamma}}$$

μ_{ref} is the freestream viscosity

k_{ref} is the freestream thermal conductivity

R_{ref} is the freestream gas constant

T_{ref} is the freestream temperature

4.2 Governing Equations

The numerical solution procedure is based on the strong conservation law form of the Navier-Stokes equations expressed in a cylindrical coordinate system. The Euler equations may be derived as a subset of the Navier-Stokes equations by neglecting viscous dissipation and thermal conductivity terms (i.e. - μ and $k = 0$). By integrating the differential form of the Navier-Stokes equations over a rotating finite control volume, the following equations are obtained:

$$\int \frac{\partial}{\partial t}(Q)dV + L_{inv}(Q) = \int KdV + L_{vis}(Q) \quad (4.2)$$

where:

$$L_{inv}(Q) = \int_{dA} [\bar{F}_{inv}dA_z + \bar{G}_{inv}dA_r + (\bar{H}_{inv} - r\omega\bar{Q})dA_\theta] \quad (4.3)$$

and:

$$L_{vis}(Q) = \int_{dA} [\bar{F}_{vis}dA_z + \bar{G}_{vis}dA_r + \bar{H}_{vis}dA_\theta] \quad (4.4)$$

The terms L_{inv} and L_{vis} represent the cell face mass, momentum, and energy flux evaluations for the inviscid, and viscous components, respectively.

The vector of dependent variables Q is defined as:

$$Q = \begin{bmatrix} \rho \\ \rho v_z \\ \rho v_r \\ \rho v_\theta \\ \rho e_t \end{bmatrix} \quad (4.5)$$

where the velocity components v_z, v_r , and v_θ are the absolute velocity components in the axial, radial, and circumferential directions relative to the propfan coordinate system, respectively (see e.g. - Fig. 3.1). The total energy function, e_t , is defined as:

$$e_t = \frac{p}{(\gamma - 1)\rho} + \frac{1}{2}(v_z^2 + v_r^2 + v_\theta^2) \quad (4.6)$$

The individual flux functions are defined as:

$$F_{inv} = \begin{bmatrix} \rho v_z \\ \rho v_z^2 + p \\ \rho v_z v_r \\ r \rho v_z v_\theta \\ \rho v_z H \end{bmatrix}, \quad G_{inv} = \begin{bmatrix} \rho v_r \\ \rho v_z v_r \\ \rho v_r^2 + p \\ r \rho v_r v_\theta \\ \rho v_r H \end{bmatrix}, \quad H_{inv} = \begin{bmatrix} \rho v_\theta \\ \rho v_z v_\theta \\ \rho v_r v_\theta \\ r(\rho v_\theta^2 + p) \\ \rho v_\theta H \end{bmatrix} \quad (4.7)$$

$$F_{vis} = \begin{bmatrix} 0 \\ \tau_{zz} \\ \tau_{zr} \\ \tau_{z\theta} \\ q_z \end{bmatrix}, \quad G_{vis} = \begin{bmatrix} 0 \\ \tau_{rz} \\ \tau_{rr} \\ \tau_{r\theta} \\ q_r \end{bmatrix}, \quad H_{vis} = \begin{bmatrix} 0 \\ \tau_{\theta z} \\ \tau_{\theta r} \\ \tau_{\theta\theta} \\ q_\theta \end{bmatrix}, \quad (4.8)$$

$$\bar{F} = F(\bar{Q}), \quad \bar{G} = G(\bar{Q}), \quad \bar{H} = H(\bar{Q})$$

$$\bar{F}_v = F_v(\bar{Q}), \quad \bar{G}_v = G_v(\bar{Q}), \quad \bar{H}_v = H_v(\bar{Q}) \quad (4.9)$$

The flux variables \bar{F} , \bar{G} , and \bar{H} are determined at each grid cell interface by determining the average (\bar{Q}) of the cell-centered dependent variables from the individual finite volumes adjoining the interface.

Finally, the cylindrical coordinate system source term is:

$$K = \begin{bmatrix} 0 \\ 0 \\ \frac{\rho v_\theta^2 + p}{r} - \tau_{\theta\theta} \\ 0 \\ 0 \end{bmatrix} \quad (4.10)$$

It should be noted that in the numerical algorithm, the radius used in the cylindrical source term K is carefully formulated to guarantee numerical conservation for the radial momentum equation. That is, for a uniform stagnant flow, the radius in the radial momentum equation is chosen such that both sides of the radial momentum equation are equal. This ensures that small geometric errors do not corrupt the conservative nature of the numerical scheme. The total enthalpy, H , is related to the total energy by:

$$H = e_t + \frac{p}{\rho} \quad (4.11)$$

The viscous stress terms may be expressed as:

$$\tau_{zz} = 2\mu \left(\frac{\partial v_z}{\partial z} \right) + \lambda_v \nabla \cdot \vec{V}, \quad (4.12)$$

$$\tau_{zr} = \mu \left[\left(\frac{\partial v_r}{\partial z} \right) + \left(\frac{\partial v_z}{\partial r} \right) \right], \quad (4.13)$$

$$\tau_{z\theta} = 2\mu \left[\left(\frac{1}{r} \frac{\partial v_r}{\partial \theta} \right) + \left(\frac{\partial v_\theta}{\partial z} \right) \right], \quad (4.14)$$

$$\tau_{rr} = 2\mu \left(\frac{\partial v_r}{\partial r} \right) + \lambda_v \nabla \cdot \vec{V}, \quad (4.15)$$

$$\tau_{r\theta} = 2\mu \left[\left(\frac{1}{r} \frac{\partial v_r}{\partial z} \right) + \left(\frac{\partial v_\theta}{\partial r} \right) - \left(\frac{v_\theta}{r} \right) \right], \quad (4.16)$$

$$\tau_{\theta\theta} = 2\mu \left(\frac{1}{r} \frac{\partial v_\theta}{\partial \theta} + \frac{\partial v_r}{r} \right) + \lambda_v \nabla \cdot \vec{V}, \quad (4.17)$$

$$q_z = v_z \tau_{zz} + v_r \tau_{zr} + v_\theta \tau_{z\theta} + k \frac{\partial T}{\partial z}, \quad (4.18)$$

$$q_r = v_z \tau_{rz} + v_r \tau_{rr} + v_\theta \tau_{r\theta} + k \frac{\partial T}{\partial r}, \quad (4.19)$$

$$q_\theta = v_z \tau_{\theta z} + v_r \tau_{\theta r} + v_\theta \tau_{\theta\theta} + k \frac{\partial T}{\partial \theta}, \quad (4.20)$$

where μ is the first coefficient of viscosity, λ_v is the second coefficient of viscosity, and:

$$\nabla \cdot \vec{V} = \frac{\partial u_z}{\partial z} + \frac{\partial u_r}{\partial r} + \frac{1}{r} \frac{\partial u_\theta}{\partial \theta} + \frac{u_r}{r} \quad (4.21)$$

The remaining viscous stress terms are defined through the identities:

$$\tau_{rz} = \tau_{zr}, \quad (4.22)$$

$$\tau_{\theta r} = \tau_{r\theta}, \quad (4.23)$$

$$\tau_{\theta z} = \tau_{z\theta}, \quad (4.24)$$

This integral form of the governing equations is applied to a generalized finite volume in physical space as shown in Fig. 4.1. The cell surface areas dA_z , dA_r , and dA_θ are calculated using the cross product of the diagonals of a cell face, and the cell volume is determined by a procedure outlined by Hung and Kordulla [21] for generalized nonorthogonal cells.

In order to conveniently determine the viscous stress terms and thermal conduction terms across an arbitrary cell interface, a generalized coordinate transformation is applied to the viscous stress terms as follows:

$$\xi = \xi(z, r, \theta), \quad \eta = \eta(z, r, \theta), \quad \zeta = \zeta(z, r, \theta) \quad (4.25)$$

The chain rule may then be used to expand the various derivatives in the viscous stresses as:

$$\frac{\partial}{\partial x} = \frac{\partial \xi}{\partial x} \frac{\partial}{\partial \xi} + \frac{\partial \eta}{\partial x} \frac{\partial}{\partial \eta} + \frac{\partial \zeta}{\partial x} \frac{\partial}{\partial \zeta}, \quad (4.26)$$

$$\frac{\partial}{\partial r} = \frac{\partial \xi}{\partial r} \frac{\partial}{\partial \xi} + \frac{\partial \eta}{\partial r} \frac{\partial}{\partial \eta} + \frac{\partial \zeta}{\partial r} \frac{\partial}{\partial \zeta}, \quad (4.27)$$

$$\frac{\partial}{\partial \theta} = \frac{\partial \xi}{\partial \theta} \frac{\partial}{\partial \xi} + \frac{\partial \eta}{\partial \theta} \frac{\partial}{\partial \eta} + \frac{\partial \zeta}{\partial \theta} \frac{\partial}{\partial \zeta}, \quad (4.28)$$

The transformed derivatives may now be easily calculated by differencing the variables in computational space, and utilizing the appropriate identities for the metric differences (see e.g. [20]).

4.3 Runge-Kutta Time Integration

The time-stepping scheme used to advance the discretized equations is a four-stage Runge-Kutta integration. The solution proceeds as:

$$Q_1 = Q^n - \alpha_1 \Delta t [L(Q^n) + D(Q^n)],$$

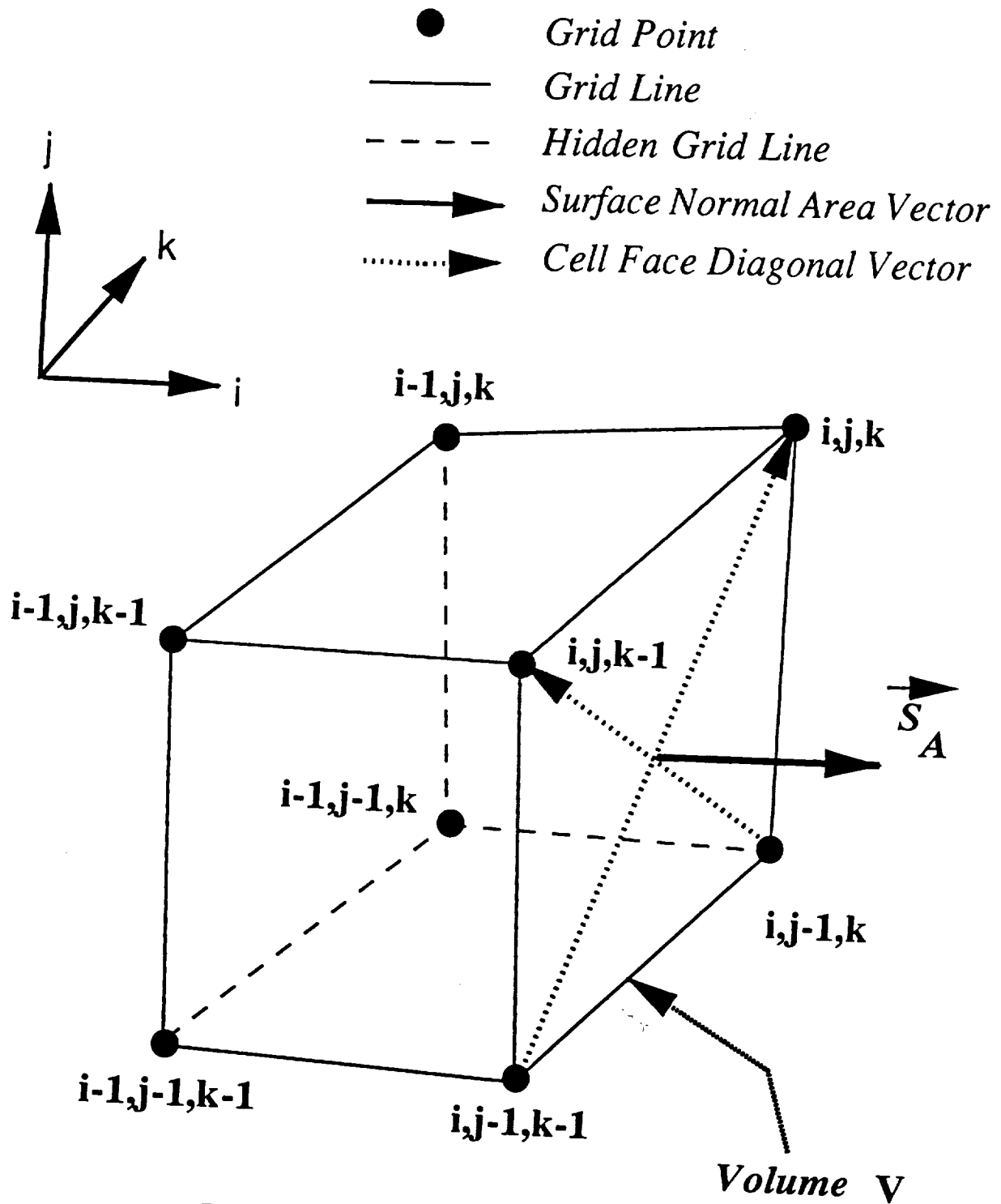


Figure 4.1: Three-dimensional finite volume cell

$$\begin{aligned}
Q_2 &= Q^n - \alpha_2 \Delta t [L(Q_1) + D(Q^n)], \\
Q_3 &= Q^n - \alpha_3 \Delta t [L(Q_2) + D(Q^n)], \\
Q_4 &= Q^n - \alpha_4 \Delta t [L(Q_3) + D(Q^n)], \\
Q^{n+1} &= Q_4
\end{aligned} \tag{4.29}$$

where:

$$\alpha_1 = \frac{1}{8}, \quad \alpha_2 = \frac{1}{4}, \quad \alpha_3 = \frac{1}{2}, \quad \alpha_4 = 1 \tag{4.30}$$

and:

$$L(Q) = L_{inv}(Q) - L_{vis}(Q) \tag{4.31}$$

Linear stability analysis indicates that this scheme is stable for all time increments δt which satisfy the stability criteria $CFL \leq 2\sqrt{2}$. The CFL number may be defined in a one-dimensional manner as:

$$CFL = \frac{\Delta t}{\frac{|u|+a}{\Delta z}} \tag{4.32}$$

This factor is calculated for each coordinate direction, and then geometrically averaged to obtain the maximum allowable time increment for a given computational cell.

For steady flows, an acceleration technique known as local time stepping is used to enhance convergence to the steady-state solution. Local time stepping utilizes the maximum allowable time increment at each point during the course of the solution. While this destroys the physical nature of the transient solution, the steady-state solution is unaffected and can be obtained more efficiently. For unsteady flow calculations, of course, a uniform value of the time step Δt must be used at every grid point to maintain the time-accuracy of the solution.

4.4 Fluid Properties

The working fluid is assumed to be air acting as a perfect gas, thus the ideal gas equation of state has been used. Fluid properties such as specific heats, specific heat ratio, and Prandtl number are assumed to be constant. The fluid viscosity is either specified as a constant, or derived from the Sutherland (see e.g. [20]) formula:

$$\mu = C_1 \frac{(T)^{\frac{3}{2}}}{T + C_2} \quad (4.33)$$

The so-called second coefficient of viscosity λ_v is fixed according to:

$$\lambda_v = -\frac{2}{3}\mu \quad (4.34)$$

The thermal conductivity is determined from the viscosity and the definition of the Prandtl number as:

$$k = \frac{cp\mu}{Pr} \quad (4.35)$$

4.5 Turbulence Model

As a result of computer limitations regarding storage and execution speed, the effects of turbulence are introduced through an appropriate turbulence model and solutions are performed on a numerical grid designed to capture the macroscopic (rather than the microscopic) behavior of the flow. A relatively standard version of the Baldwin-Lomax [22] turbulence model was adopted for this analysis. This model is computationally efficient, and has been successfully applied to a wide range of geometries and flow conditions.

The effects of turbulence are introduced into the numerical scheme by utilizing the Boussinesq approximation (see e.g. [20]), resulting in an effective calculation viscosity defined as:

$$\mu_{effective} = \mu_{laminar} + \mu_{turbulent} \quad (4.36)$$

The simulation is therefore performed using an effective viscosity which combines the effects of the physical (laminar) viscosity and the effects of turbulence through the turbulence model and the turbulent viscosity $\mu_{turbulent}$.

The Baldwin-Lomax model specifies that the turbulent viscosity be based on an inner and outer layer of the boundary layer flow region as:

$$\mu_{turbulent} = \begin{cases} (\mu_{turbulent})_{inner}, & y \leq y_{crossover} \\ (\mu_{turbulent})_{outer}, & y > y_{crossover} \end{cases} \quad (4.37)$$

where y is the normal distance to the nearest wall, and $y_{crossover}$ is the smallest value of y at which values from the inner and outer models are equal. The inner and outer model turbulent viscosities are defined as:

$$(\mu_{turb})_{inner} = \rho l^2 |\omega| \quad (4.38)$$

$$(\mu_{turb})_{outer} = KC_{cp} \rho F_{wake} F_{kleb} y \quad (4.39)$$

Here, the term l is the Van Driest damping factor

$$l = ky(1 - e^{(-y^+/A^+)}) \quad (4.40)$$

ω is the vorticity magnitude, F_{wake} is defined as:

$$F_{wake} = y_{max} F_{max} \quad (4.41)$$

where the quantities y_{max} , F_{max} are determined from the function

$$F(y) = y|\omega|[1 - e^{(-y^+/A^+)}] \quad (4.42)$$

The term y^+ is defined as

$$y \sqrt{\frac{\rho|\omega|}{\mu_{laminar}}} \quad (4.43)$$

The quantity F_{MAX} is the maximum value of $F(y)$ that occurs in a profile, and y_{MAX} is the value of y at which it occurs. The determination of F_{MAX} and y_{MAX} is perhaps the most difficult aspect of this model for three-dimensional flows. The profile of $F(y)$ versus y can have several local maximums, and it is often difficult to establish which values should be used. In this case, F_{MAX} is taken as the maximum value of $F(y)$ between a y^+ value of 350.0 and 1000.0. The function F_{kleb} is the Klebanoff intermittency factor given by

$$F_{kleb}(y) = [1 + 5.5(\frac{C_{kleb}y}{y_{max}})^6]^{-1} \quad (4.44)$$

and the remainder of the terms are constants defined as:

$$A^+ = 26,$$

$$C_{cp} = 1.6,$$

$$C_{kleb} = 0.3,$$

$$k = 0.4,$$

$$K = 0.0168 \quad (4.45)$$

In practice, the turbulent viscosity is limited such that it never exceeds 1000.0 times the laminar viscosity.

The turbulent flow thermal conductivity term is also treated as the combination of a laminar and turbulent quantity as:

$$k_{effective} = k_{laminar} + k_{turbulent} \quad (4.46)$$

For turbulent flows, the turbulent thermal conductivity $k_{turbulent}$ is determined from a turbulent Prandtl number $Pr_{turbulent}$ such that

$$Pr_{turbulent} = \frac{c_p \mu_{turbulent}}{k_{turbulent}} \quad (4.47)$$

The turbulent Prandtl number is normally chosen to have a value of 0.9.

In order to properly utilize this turbulence model, a fairly large number of grid cells must be present in the boundary layer flow region, and, perhaps of greater importance, the spacing of the first grid cell off of a wall should be small enough to accurately account for the inner "law of the wall" turbulent boundary layer profile region. Unfortunately, this constraint is typically not satisfied due to grid-induced problems or excessive computational costs, especially for time-dependent flow calculations. A convenient technique to suppress this problem is the use of wall functions to replace the inner turbulent model function, and solve for the flow on a somewhat coarser grid. This technique has not been tested for the current application, but would appear to be a reasonable area for future research. Practical applications of the Baldwin-Lomax model for three-dimensional viscous flow must be made with the limitations of the model in mind. The Baldwin-Lomax model was designed for the prediction of wall bounded turbulent shear layers, and is not likely to be well suited for flows with massive separations or large vortical structures. There are, unfortunately, a number of applications for ducted and unducted propfans where this model

is likely to be invalid. This is also likely to be an area requiring improvement in the future.

4.6 Artificial Dissipation

An artificial dissipation operator (D) is added to the numerical scheme to control oscillations in the solution which result from the centered-difference approach in the flux derivative formulation. This problem is especially prevalent near shock waves, and it has been observed that the formulation of the dissipative term can have a significant influence on the final numerical solution. Jameson [23] demonstrated that a dissipative system combining second- and fourth-difference smoothing terms can effectively eliminate undesirable numerical oscillations without destroying the accuracy of the solution. The scheme presented below is stable for all time steps satisfying the *CFL*-related time step limitation

$$CFL \leq 2\sqrt{2} \quad (4.48)$$

The dissipation operator is constructed in the following manner:

$$D_z(Q) = d_{i+\frac{1}{2},j,k} - d_{i-\frac{1}{2},j,k} \quad (4.49)$$

$$d_{i+\frac{1}{2},j,k} = \frac{V_{i+\frac{1}{2},j,k}}{(\Delta t_i)_{i+\frac{1}{2},j,k}} \left[(\epsilon_2)_{i+\frac{1}{2},j,k} \Delta_z Q_{i+\frac{1}{2},j,k} - (\epsilon_4)_{i+\frac{1}{2},j,k} \Delta_z^3 Q_{i+\frac{1}{2},j,k} \right] \quad (4.50)$$

where:

$$(\epsilon_2)_{i+\frac{1}{2},j,k} = \kappa^2 \max(\nu_{i+1,j,k}, \nu_{i,j,k}) \quad (4.51)$$

$$(\epsilon_4)_{i+\frac{1}{2},j,k} = \max(0, \kappa^4 - \epsilon_{i+\frac{1}{2},j,k}^2) \quad (4.52)$$

$$\nu_{i,j,k} = \frac{|p_{i+1,j,k} - 2p_{i,j,k} + p_{i-1,j,k}|}{|p_{i+1,j,k} + 2p_{i,j,k} + p_{i-1,j,k}|} \quad (4.53)$$

Typical values for the second and fourth difference damping constants are:

$$\kappa^2 = \frac{1}{4} \quad \kappa^4 = \frac{1}{64} \quad (4.54)$$

The term Δt_i represents a one-dimensional equivalent of the maximum allowable time step in the given coordinate direction. The use of this factor introduces an eigenvalue scaling into the dissipation operator which minimizes the added dissipation in coordinate directions which do not limit the stability of the algorithm.

The damping scheme described above may be applied directly for inviscid flow calculations, but must be modified slightly for viscous flow calculations. As the magnitude of the physical viscous dissipation grows, the artificial dissipation is no longer required, and, in fact, can prevent convergence to the desired solution due to the complicated interaction between the physical and numerical dissipation structures. In order to deal with this problem, a controlling term is added to the artificial dissipation operator to smoothly eliminate the damping term near solid walls. This scheme does not reduce the artificial damping in the freestream, and could interfere with larger freestream vortical structures which may not require added dissipation. This implementation of the damping scheme is another area requiring future study. The dissipation in viscous regions is controlled by a simple one-dimensional function:

$$(\epsilon_2)_{i+\frac{1}{2},j,k} = \Upsilon \kappa^2 \max(\nu_{i+1,j,k}, \nu_{i,j,k}) \quad (4.55)$$

$$(\epsilon_4)_{i+\frac{1}{2},j,k} = \Upsilon \max(0, (\kappa_4) - (\epsilon_2)_{i+\frac{1}{2},j,k}) \quad (4.56)$$

where:

$$\Upsilon = \sin\left(\frac{\pi}{2} \frac{m}{m_{limit}}\right) \quad (4.57)$$

Here m is the index of the coordinate direction along which the nearest wall is found, and m_{limit} is an approximate grid reference location for the boundary layer edge. This simple model was found to be satisfactory for most calculations, and avoids the necessity for finding the true boundary layer edge (if one can actually be defined for complicated three-dimensional flows).

The complete dissipation operator $D_{i,j,k}$ is constructed as the sum of the dissipation operators in each of the respective coordinate directions as:

$$D_{i,j,k} = (D_z)_{i,j,k} + (D_r)_{i,j,k} + (D_\theta)_{i,j,k} \quad (4.58)$$

4.7 Implicit Residual Smoothing

Implicit residual smoothing is a technique commonly used for accelerating the convergence of explicit time-marching schemes applied to steady flow calculations. Since an unsteady flow calculation for a given geometry and grid is likely to be computationally more expensive than a similar steady flow calculation, it would be advantageous to utilize this acceleration technique for time-dependent flow calculations as well. In recent calculations for two dimensional unsteady flows, Jorgensen and Chima [24] demonstrated that a variant of the implicit residual smoothing technique could be incorporated into a time-accurate explicit method to permit the use of larger calculation time increments without adversely affecting the results of the unsteady calculation. The implementation of this residual smoothing scheme reduced the CPU

time for their calculation by a factor of five. This so-called time-accurate implicit residual smoothing operator was then also demonstrated by Rao and Delaney [25] for a similar two-dimensional unsteady calculation. Although this “time-accurate” implicit residual smoothing scheme is not developed theoretically to accurately provide the unsteady solution, it can be demonstrated that errors introduced through this residual smoothing process are very local in nature, and are generally not greater than the discretization error.

In this study, a variant of the time-accurate implicit residual smoothing operator described by Jorgensen and Chima [24] was extended to three spatial dimensions and implemented in the unsteady solution procedure. The standard implicit residual smoothing operator can be written as:

$$(1 - \epsilon_z \delta_{zz})(1 - \epsilon_r \delta_{rr})(1 - i\epsilon_\theta \delta_{\theta\theta})\bar{R}_{i,j,k} = R_{i,j,k} \quad (4.59)$$

where $R_{i,j,k}$ (the residual) is expressed as:

$$R_{i,j,k} = \Delta t [L(Q_{i,j,k})_{inv} + L(Q_{i,j,k})_{vis} + D(Q_{i,j,k})] \quad (4.60)$$

Here the differencing operator δ is discretized as:

$$\delta_{zz}Q_{i,j,k} = Q_{i+1,j,k} - 2Q_{i,j,k} + Q_{i-1,j,k}$$

$$\delta_{rr}Q_{i,j,k} = Q_{i,j+1,k} - 2Q_{i,j,k} + Q_{i,j-1,k}$$

$$\delta_{\theta\theta}Q_{i,j,k} = Q_{i,j,k+1} - 2Q_{i,j,k} + Q_{i,j,k-1}$$

The reduction is applied sequentially in each coordinate direction as:

$$R_{i,j,k}^* = (1 - \epsilon_z \delta_{zz})_{-1} R_{i,j,k}$$

$$\begin{aligned}
R_{i,j,k}^{**} &= (1 - \epsilon_z \delta_{rr})_{-1} R_{i,j,k}^* \\
R_{i,j,k}^{***} &= (1 - \epsilon_z \delta_{\theta\theta})_{-1} R_{i,j,k}^{**} \\
\bar{R}_{i,j,k} &= R_{i,j,k}^{***}
\end{aligned} \tag{4.61}$$

where each of the first three steps above require the inversion of a scalar tridiagonal matrix. The residual smoothing operator is applied at the first and third stage during the four-stage Runge-Kutta algorithm. The time-marching scheme then becomes:

$$\begin{aligned}
Q_1 &= Q^n - \alpha_1 \bar{R}(Q^n) \\
Q_2 &= Q^n - \alpha_2 R(Q_1) \\
Q_3 &= Q^n - \alpha_3 \bar{R}(Q_2) \\
Q_4 &= Q^n - \alpha_4 R(Q_3) \\
Q^{n+1} &= Q_4
\end{aligned} \tag{4.62}$$

For steady flow calculations, a constant value of $\epsilon_z = \epsilon_r = \epsilon_\theta = 2$ is typically used to provide accelerated convergence. It can be shown that the Runge-Kutta time stepping scheme described in this report becomes unconditionally stable for any time step Δt when ϵ satisfies:

$$\epsilon_{i,j,k} \leq \frac{1}{4} \left[\left(\frac{CFL_{i,j,k}}{CFL_{i,j,k}^*} \right)^2 - 1 \right] \tag{4.63}$$

where $\epsilon_{i,j,k}$ now varies throughout the grid, and $CFL_{i,j,k}$ represents the local value of the CFL number based on the calculation time increment $\Delta t_{i,j,k}$, and $CFL_{i,j,k}^*$ represents the maximum stable value of the CFL number permitted by the unmodified scheme. It is obvious then that the residual smoothing operator need only be

applied in those regions where the local CFL number exceeds the stability-limited value, and therefore the local variation of $\epsilon_{i,j,k}$ is determined as:

$$\epsilon_{i,j,k} = \max \left(0, \frac{1}{4} \left[\left(\frac{CFL_{i,j,k}}{CFL_{i,j,k}^*} \right)^2 - 1 \right] \right) \quad (4.64)$$

In this approach, the residual operator coefficient becomes zero at points where the local CFL number is less than that required by stability, and the influence of the smoothing is only locally applied to those regions exceeding the stability limit. Practical experience involving unsteady flow calculations suggests that for a constant time increment, the majority of the flowfield utilizes CFL numbers less than the stability-limited value to maintain a reasonable level of accuracy. Local smoothing is therefore typically required only in regions of small grid spacing, where the stability-limited time step is very small. Numerical tests both with and without the time-accurate implicit residual smoothing operator for the flows of interest in this study were found to produce essentially identical results, while the time-accurate residual smoothing resulted in a decrease in CPU time by a factor of 2-3.

4.8 Boundary Conditions

Inflow and exit boundary conditions are applied numerically using characteristic theory. A one-dimensional isentropic system of equations is utilized to derive the following characteristic equations at an axial inflow/outflow boundary:

$$\frac{\partial C^-}{\partial t} - (v_z - a) \frac{\partial C^-}{\partial z} = 0, \quad (4.65)$$

$$\frac{\partial C^+}{\partial t} + (v_z + a) \frac{\partial C^+}{\partial z} = 0 \quad (4.66)$$

where:

$$C^- = v_z - \frac{2a}{\gamma - 1}, \quad C^+ = v_z + \frac{2a}{\gamma - 1} \quad (4.67)$$

In order to efficiently process boundary information in the numerical solution, phantom cells are located just outside the computational domain to permit the unmodified application of the interior point scheme at near boundary cells. Boundary condition information is effectively introduced into the solution by properly controlling the dependent variables in the phantom cells while permitting the application of the standard interior point scheme at near boundary cells.

For subsonic normal inflow, the upstream running invariant C^- is extrapolated to the inlet, and along with the equation of state, specified total pressure, total temperature, and flow angle (used to specify the angle of attack), the flow variables at the boundary may be determined. It should be mentioned that the effective inflow angle may vary for a given block as it rotates about the axis, and therefore the inflow angle is actually a function of circumferential position, θ . At the exit, a static pressure is specified at the hub for internal flows, and at the outer boundary for external flows. The remaining pressures along the outflow boundary are calculated by integrating the radial momentum equation:

$$\frac{\partial p}{\partial r} = \frac{\rho v_\theta^2}{r} \quad (4.68)$$

In this case, the downstream running invariant C^+ is used to update the phantom cells at the exit boundary. Far-field boundaries also use this characteristic technique based on whether the local flow normal to the boundary passes into or out of the domain. The solid surfaces (hub, cowl, airfoils) must satisfy flow tangency for inviscid flow:

$$\vec{V} \cdot \vec{n} = 0 \quad (4.69)$$

or no slip for viscous flows:

$$v_z = 0, \quad v_r = 0, \quad v_\theta = r\omega \quad (4.70)$$

In both cases, we specify no convective flux through the boundary (an impermeable surface), and hence, only pressure is needed at the phantom cell. The pressure may be extrapolated, or updated using a variant of the normal momentum equation. In this case, extrapolation was found to be the most effective technique based on rapid convergence and adequate results. In addition, solid surfaces are also assumed to be adiabatic, which implies that the normal temperature gradient is also zero.

4.9 Multiple-Block Coupling

For the multiple-block C-grid scheme, the solution is performed on a single grid block at a time. Special boundary conditions along block boundaries are therefore required to provide some transport of information between blocks. This transport is provided through a simple procedure which relies on the fact that the grid block boundaries have coincident grid points. Since the standard interior point scheme is performed at the first grid cell off the block boundary, all that is required is to determine the fluxes along the block boundaries themselves. Phantom points are provided along each side of a block boundary to accommodate the flux calculation at the block boundary cell face. The flow variables in the phantom cells are provided by interrogating the corresponding cell in the adjacent block when a particular value is required. After each stage of the Runge-Kutta integration for each block, the block boundary phantom cells are updated by utilizing the new dependent variable

values from the adjacent blocks. This direct specification technique was compared to a characteristic-based method similar to the inlet and exit boundary condition routines, and was found to provide enhanced convergence behavior.

For ducted configurations, the grid blocks used to discretize the blades are rotating, while the grid blocks discretizing the cowl and outer flow regions are stationary. Under these circumstances, flow variables for the phantom points are found through a circumferential interpolation of the neighboring computational blocks based on the known angular position of the blades. This technique presumes that the meridional coordinates of the grid points along the block boundaries are coincident. It should be mentioned that the interpolation technique does not strictly enforce a global conservation across the block boundary, although this has not posed a problem in the calculations performed to date.

Artificial damping is applied at the block boundaries by neglecting the fourth order derivative term due to the lack of a four point differencing stencil at the boundaries. Implicit residual smoothing is applied at the block boundary by imposing a zero residual gradient (i.e. $(dR/dz) = 0.0$) condition at the boundary.

4.10 Solution Procedure

The numerical solution is performed in an identical manner for both unducted and ducted propfan geometries. Assuming that the numerical grid and flow parameters are known, the time-marching procedure may begin from some set of initial data. This initial data is specified as a uniform flow, or may be introduced from a previous solution. The time-marching procedure is applied iteratively to update the flow vari-

ables as the solution proceeds. Steady state solutions are deemed converged when the average residual R has been reduced by a factor of 10^{-3} , or when the residual has stopped converging.

For unsteady flows, it is usually best to first obtain a steady state solution for a single blade passage, and then duplicate this flowfield for the remaining blade passages to construct the initial data for the full rotor for an unsteady solution. The unsteady solution may then be advanced in time with a uniformly specified time step, until a time-periodic solution is achieved. This normally requires two complete revolutions of the rotor.

5. RESULTS

Several numerical results from the multiple-block 3D Euler/Navier-Stokes analysis code *AOA* described in Chapter 4 are presented in the sections which follow. In most cases, steady flow results are given to verify the accuracy of the formulation before presenting the unsteady computations. Viscous and inviscid flow calculations are presented initially for a 2-bladed SR7 propfan for which both steady state and time-dependent experimental airfoil surface static pressure distribution data were available. Next, the Euler algorithm is utilized to predict the flow about the complete 8-bladed SR7 propfan geometry, illustrating the time-dependent formation and dissipation of a blade passage shock system. A demonstration of unsteady inviscid flow about a generic ducted propfan geometry at angle of attack is presented in the following section. Finally, results from viscous flow calculations are compared extensively with high speed experimental data for a 1.15 pressure ratio ducted fan configuration. Each case is discussed separately in the sections which follow. A summary of the computational statistics (CPU time, grid size, etc.) associated with each of the calculations presented in this report is given in Table 5.1.

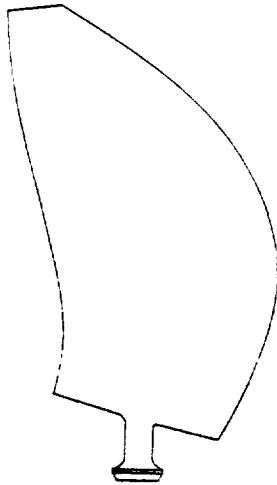
Table 5.1: Summary of computational characteristics for *ADPAC* test cases

Test Case	Steady/ Unsteady	Viscous/ Inviscid	# Blocks	Grid Size	Mach #	Cray-II CPU (minutes)
Modane	Steady	Inviscid	1	135,000	0.2	48
Modane	Steady	Viscous	1	135,501	0.2	153
Modane (Coarse)	Unsteady	Inviscid	2	15,180	0.5	54
Modane (Fine)	Unsteady	Inviscid	2	195,734	0.5	2322
Modane	Unsteady	Viscous	2	131,936	0.5	2546
SR7	Unsteady	Inviscid	8	237,160	0.8	2136
Ducted SR7	Unsteady	Inviscid	40	450,000	0.8	2640
NASA Fan	Steady	Viscous	5	183,414	0.75-0.85	210
NASA Fan	Unsteady	Viscous	60	488,320	0.20	3361

5.1 SR7 2-Bladed Propfan Modane Tests

In order to verify the numerics of the aerodynamic solver, several initial calculations were performed for steady and unsteady flows about unducted propfans. A number of experimental studies have been performed for the unducted SR7 propfan geometry ranging from scaled wind tunnel tests to in-flight measurements. The SR7 propfan design utilizes 8 blades with 41 degrees of sweep at the tip. A special hub contour is employed to eliminate flow choking at the hub. A description of the SR7 design parameters is given in Fig. 5.1.

The first extensive comparison of predicted results for steady and unsteady unducted propfan flows was performed based on the test of the SR7 airfoil at the Modane wind tunnel test facility reported by Bushnell et al. [26]-[27]. In the Modane tests, the propfan driver did not have enough power to drive the full 8-bladed configuration, so a 2-bladed version was tested instead. The airfoil surfaces were instrumented to



Characteristic	SR-7A
Number of blades	8
Tip sweep angle, ^a deg	41
Model diameter, cm (in.)	62.23 (24.5)
Tip speed, m/sec (ft/sec)	243.8 (800)
Power loading, kW/m ² (shp/ft ²)	256.85 (32)
Activity factor, AF	227
Integrated design lift coefficient, c_{L1}	0.202
Airfoils	NASA 16 and 65/CA
Ratio of nacelle maximum diameter to propeller diameter	0.35
Cruise design Mach number	0.80
Cruise design advance ratio	3.06
Cruise design power coefficient	1.45

^aGeometric measurement from planform.

Figure 5.1: SR7 propfan design characteristics

permit the measurement of steady and unsteady airfoil surface static pressures.

Both steady and unsteady, viscous and inviscid flow calculations were performed for this geometry to facilitate a comparison with the experimental data. An illustration of the numerical grid used for the steady state inviscid and viscous flow calculations are presented in Figs. 5.2 and 5.3, respectively. The inviscid grid contained $120 \times 45 \times 25$ points in the axial, radial and circumferential directions, respectively, while the viscous grid numbered $93 \times 47 \times 31$. The viscous grid was slightly smaller in the axial direction to reduce overall CPU time. The clustering of grid lines near solid surfaces, necessary to resolve the blade surface boundary layer flow, is clearly evident in the viscous grid.

Steady flow predictions were compared with experimental data for a nominal power coefficient of 0.250. The freestream Mach number was 0.2, with an advance ratio of 0.881. This particular flow condition gives rise to a strong leading edge vortex which dominates the flow characteristics of the suction surface of the airfoil, and was therefore considered a challenging test case for numerical simulation.

Predicted steady flow (zero angle of attack) airfoil surface static pressure coefficient distributions for both inviscid and viscous flow are compared with experimental data at spanwise locations of 28.4% and 93.1% (r/R) in Figs. 5.4-5.5, respectively. Both Euler and Navier-Stokes solutions produced a leading edge vortex, evidenced by the large pressure drop near the leading edge of the suction surface in Figure 5.4. The viscous flow calculation more accurately reproduces the experimental findings in this region, presumably due to a more accurate representation of the leading edge vortex, and in part due to the blockage imparted by the airfoil surface boundary layer.

Further comparisons with experimental data indicate that the exact location of the origin of the leading edge vortex is not adequately resolved in either calculation, and indicates that spanwise grid refinement can play a larger role in the accuracy of the results than either circumferential or axial grid refinement. The predicted trajectory of the leading edge vortex was also somewhat different than the trajectory indicated by the experimental data. This feature is best illustrated in the comparison of predicted airfoil suction surface static to total pressure ratio contours given in Fig. 5.6. The predicted contours display a remarkable similarity to the experimental distribution. The leading edge vortex path is indicated by the region of low pressure bending across the suction surface from approximately 30% span towards the airfoil tip. The experimental contours suggest that the leading edge vortex remains attached to the leading edge, while both viscous and inviscid contours suggest that the vortex drifts further aft axially on the blade. This slight discrepancy may be due to several factors. The exact deflected airfoil shape and blade setting angle are unknown (experimental uncertainty is on the order of 1 degree), which introduces a significant source of error in the calculation. In addition, to truly capture the detailed physics of this complicated vortical flow would require grid densities in excess of the present grid system, and therefore grid resolution must be considered a potential source of error.

The viscous flow predictions for this case show some striking aerodynamic features resulting from the complicated flow over this highly three-dimensional airfoil. The leading edge vortex is clearly depicted in the particle flow trajectories illustrated in Fig. 5.7. The influence of the leading edge vortex is depicted by the color static pressure contours used to define the blade in this figure. During the development of

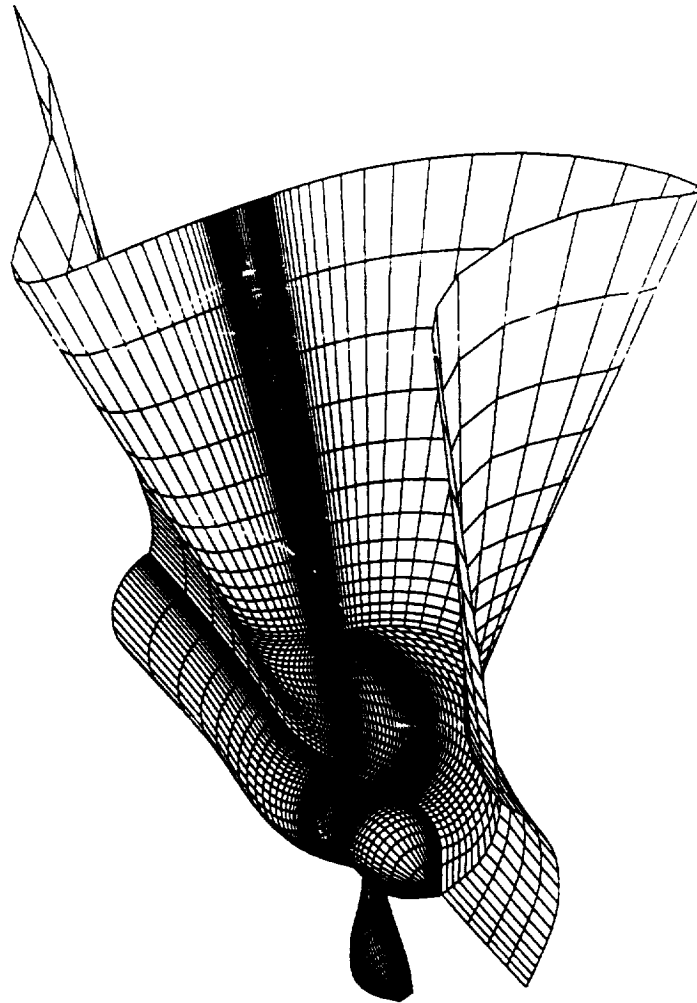


Figure 5.2: 2-bladed SR7 propfan geometry and steady state inviscid calculation grid for Modane test comparison

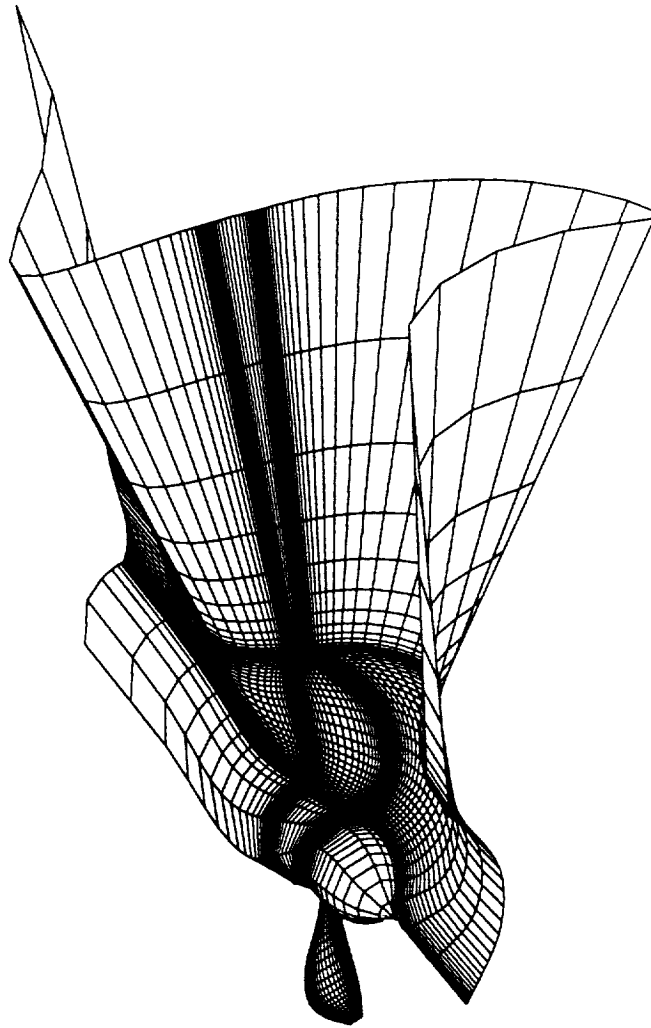


Figure 5.3: 2-bladed SR7 propfan geometry and steady state viscous calculation grid for Modane test comparison

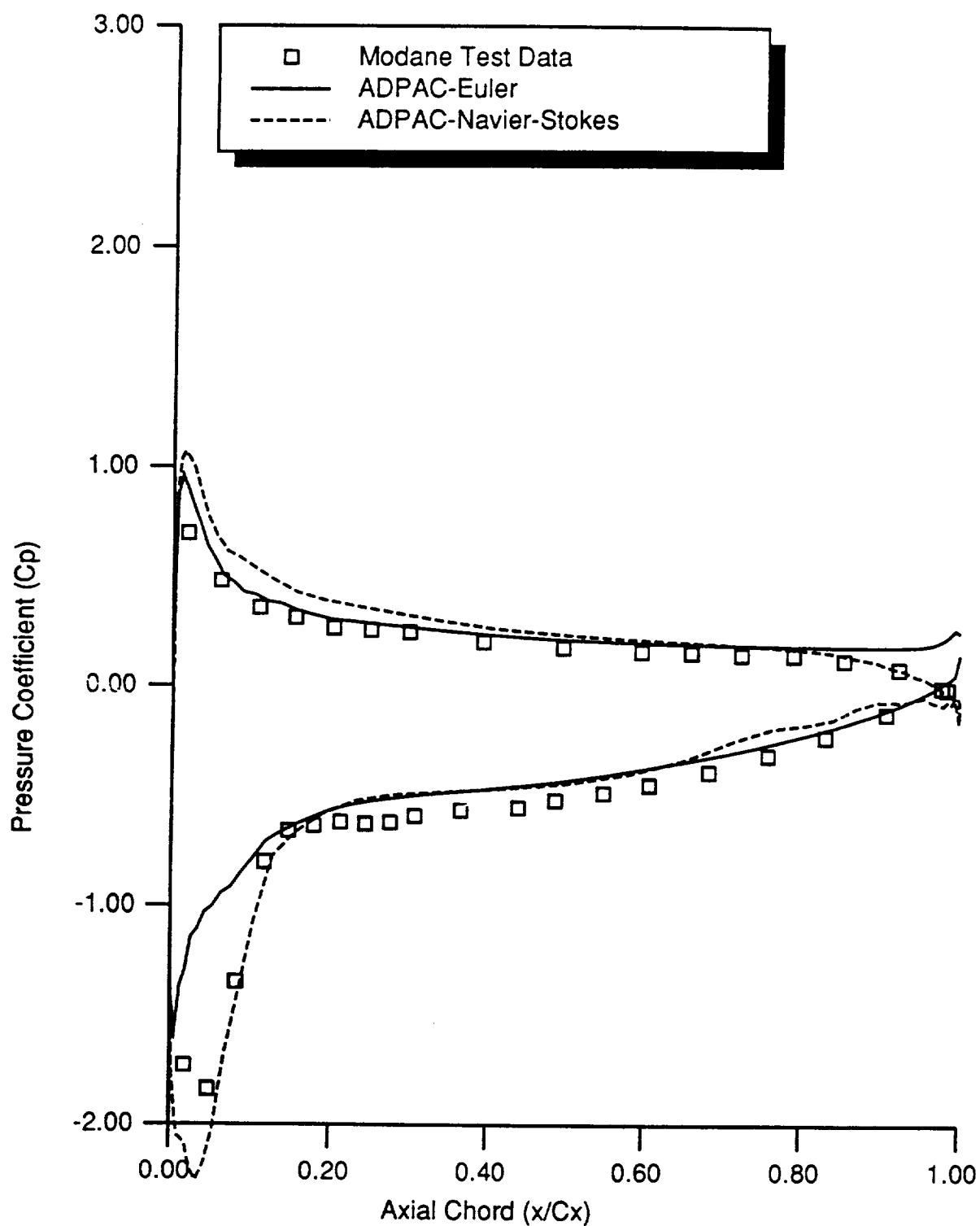


Figure 5.4: Comparison of predicted and experimental airfoil surface static pressure coefficient distributions for 2-bladed SR7 propfan Modane test (28.4% span)

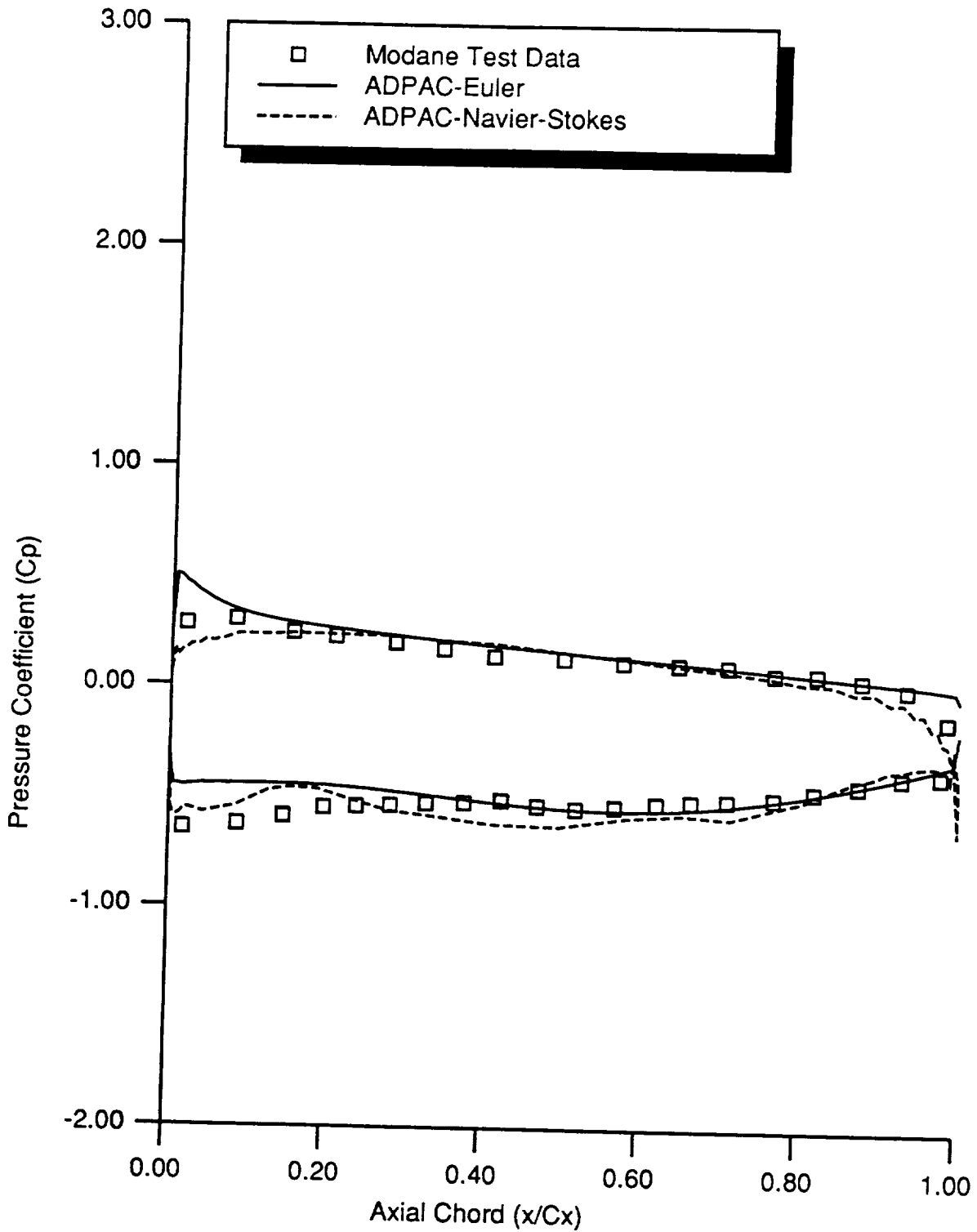


Figure 5.5: Comparison of predicted and experimental airfoil surface static pressure coefficient distributions for 2-bladed SR7 propfan Modane test (93.1% span)

*ADPAC-Navier-Stokes**ADPAC-Euler**Experiment*

Figure 5.6: Comparison of predicted and experimental airfoil suction surface static/total pressure ratio contours for 2-bladed SR7 propfan



Figure 5.7: Illustration of predicted turbulent flow leading edge vortex particle trajectory traces for for 2-bladed SR7 propfan

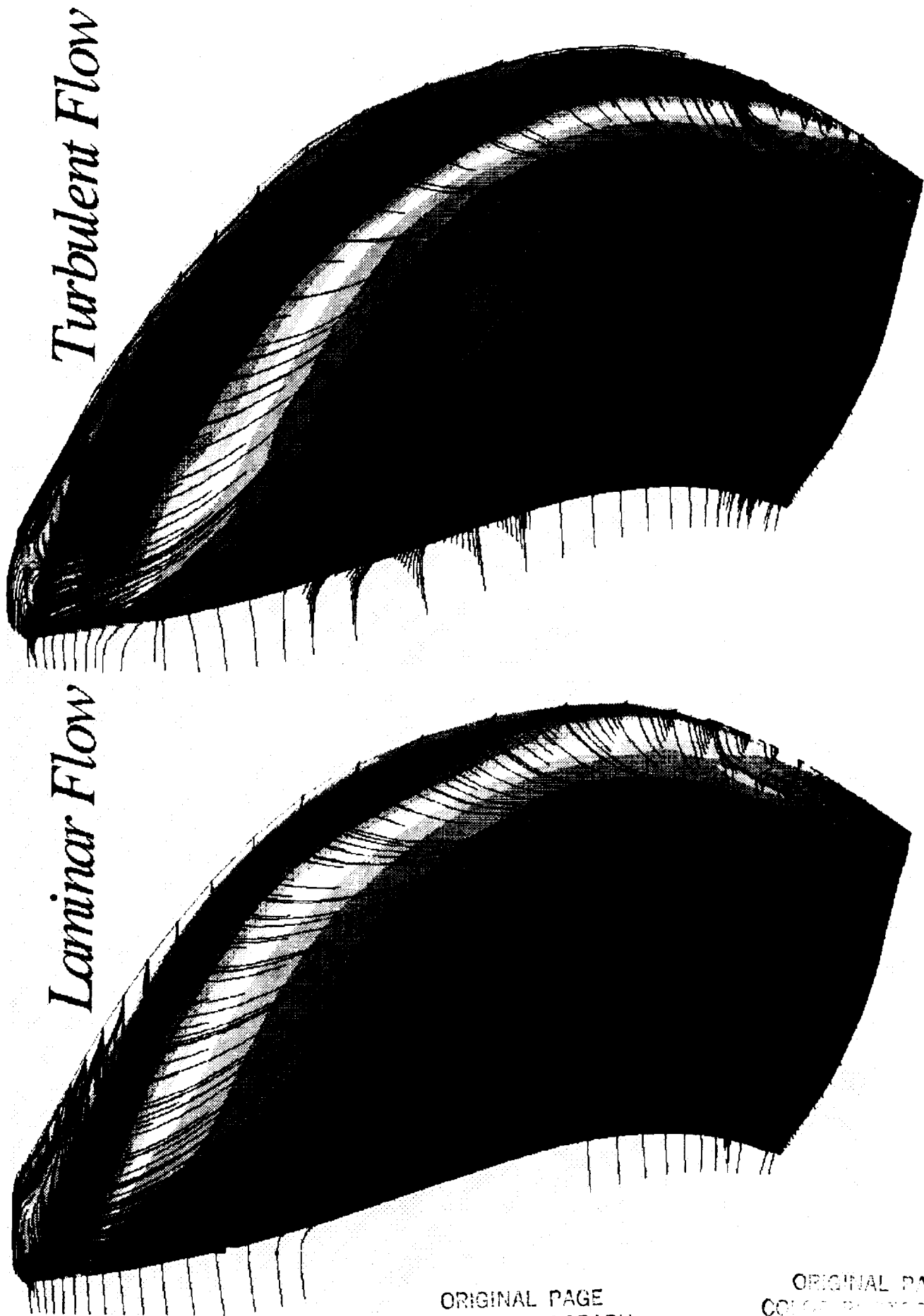


Figure 5.8: Comparison of laminar and turbulent predicted suction surface shear flow patterns and static/total pressure ratio contours for 2-bladed SR7

ORIGINAL PAGE
COLOR PHOTOGRAPH

ORIGINAL PAGE
COLOR PHOTOGRAPH

the viscous flow solution scheme, both laminar and turbulent viscous flow predictions were performed for this case, thus allowing some insight into the effects of turbulence for highly loaded propfan airfoils. An interesting depiction of the results of this study is found in the suction surface shear flow patterns for both laminar and turbulent flow predictions given in Fig. 5.8. The shear flow patterns were generated by releasing particles at the first grid point off the surface and tracing the near surface flow pattern by restricting the particle paths to the first grid plane off the suction surface. This technique is roughly equivalent to a surface oil flow visualization technique. The suction surface flow patterns for both predictions clearly reveal the radial secondary flows generated by the leading edge and tip vortices. In addition, the laminar calculation reveals a small leading edge separation region near the propfan root leading edge. The turbulent flow results shows no such phenomena. As expected, the laminar result also reveals a large region of separated flow near the trailing edge of the blade. The low momentum fluid in the separation zone migrates radially outward, causing a complicated interaction of leading edge vortex, tip vortex, and radial migration flows near the tip. By comparison, the turbulent flow prediction shows a much smaller region of separation at the trailing edge, and less radial migration, although the interacting flows near the tip are no less complicated. These results demonstrate the detailed flow patterns which may be captured with advanced, three-dimensional viscous flow calculations.

All of the results for the SR7 presented thus far have been based on a single blade passage grid solution. Unsteady flow predictions for the SR7 2-bladed propfan were initiated from steady flow results similar to those already presented, although

slightly fewer grid points were utilized to minimize the computational cost. For the unsteady predictions, each single passage grid system was rotated and duplicated to discretize the adjacent blade passage, and the full features of the multiple-grid block *AOA* solver were utilized to track the solution for the complete rotor system. For the time-dependent calculations, the flow Mach number was 0.5, and the angle of attack was 3.0 degrees. Time-dependent inviscid flow predictions were generated for both a coarse and a fine grid to illustrate the effects of grid density on the unsteady flow predictions. The coarse grid utilized 46x15x11 grid points per blade passage, while the fine grid utilized 77x41x31 points per blade passage. Viscous flow predictions were performed for a single grid utilizing 56x38x31 points per blade passage.

A steady state solution was used to initialize the time-dependent calculation. For reference, comparisons of predicted and experimental steady flow (zero angle of attack) airfoil surface static/inlet total pressure ratio distributions for this case are given at 28.4% and 94.4% span in Figs. 5.9-5.10, respectively. As in the previous steady flow comparisons, the agreement between predictions and experiment is good.

Both viscous and inviscid solutions were then initiated from the corresponding steady state (zero angle of attack) solutions. Roughly two complete revolutions of the rotor were required to reach a time-periodic solution. The results presented here correspond to the third revolution.

Several cycles of both the coarse and fine grid inviscid as well as the fine grid viscous predicted phase-resolved time-dependent pressure histories are compared with experimental data at 64% radial span and 4.9% and 36.7% chord on the airfoil suction

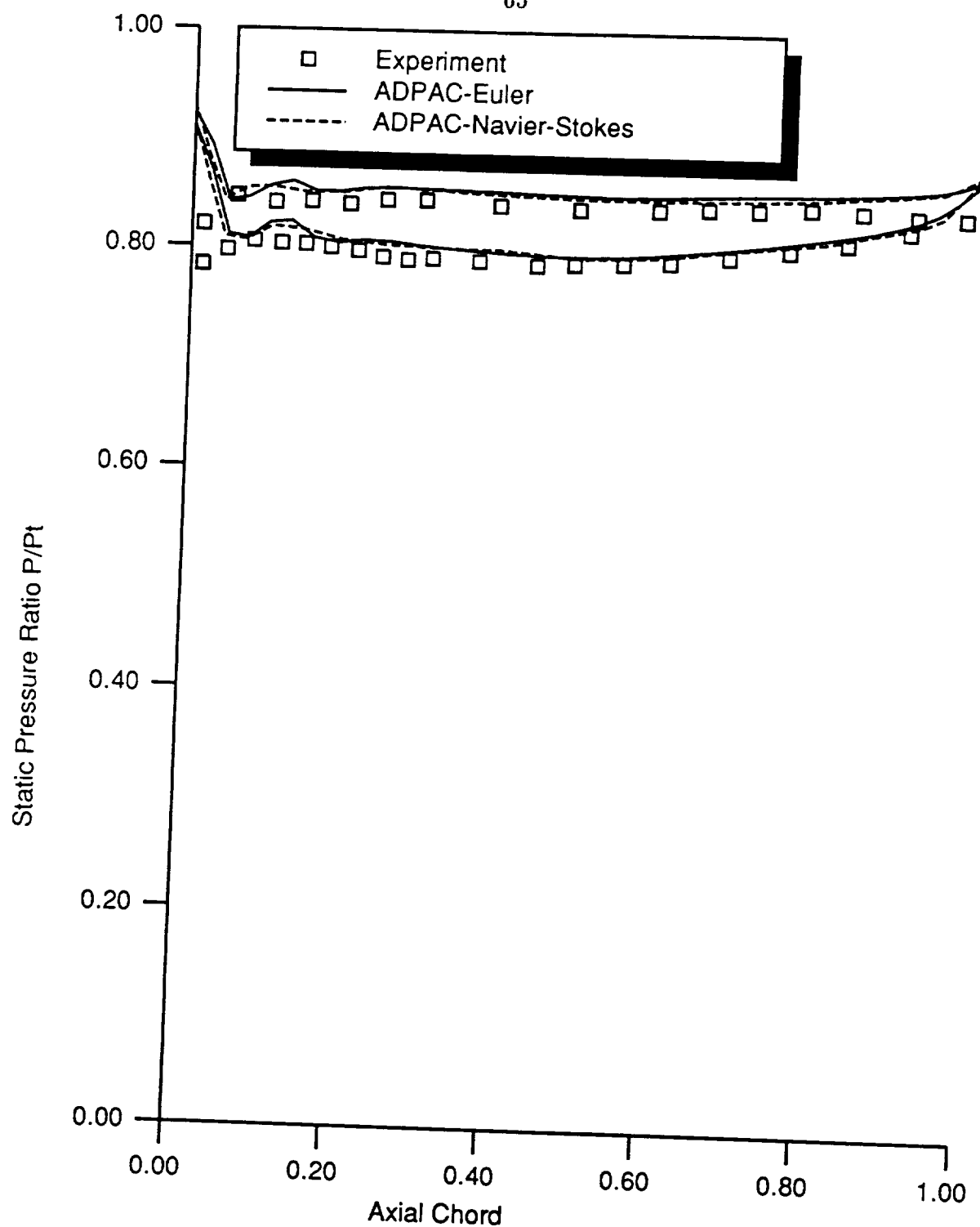


Figure 5.9: Comparison of predicted and experimental airfoil surface static/total pressure ratio distributions for 2-bladed SR7 propfan (28.4% span, $M=0.5$, $J=3.06$).

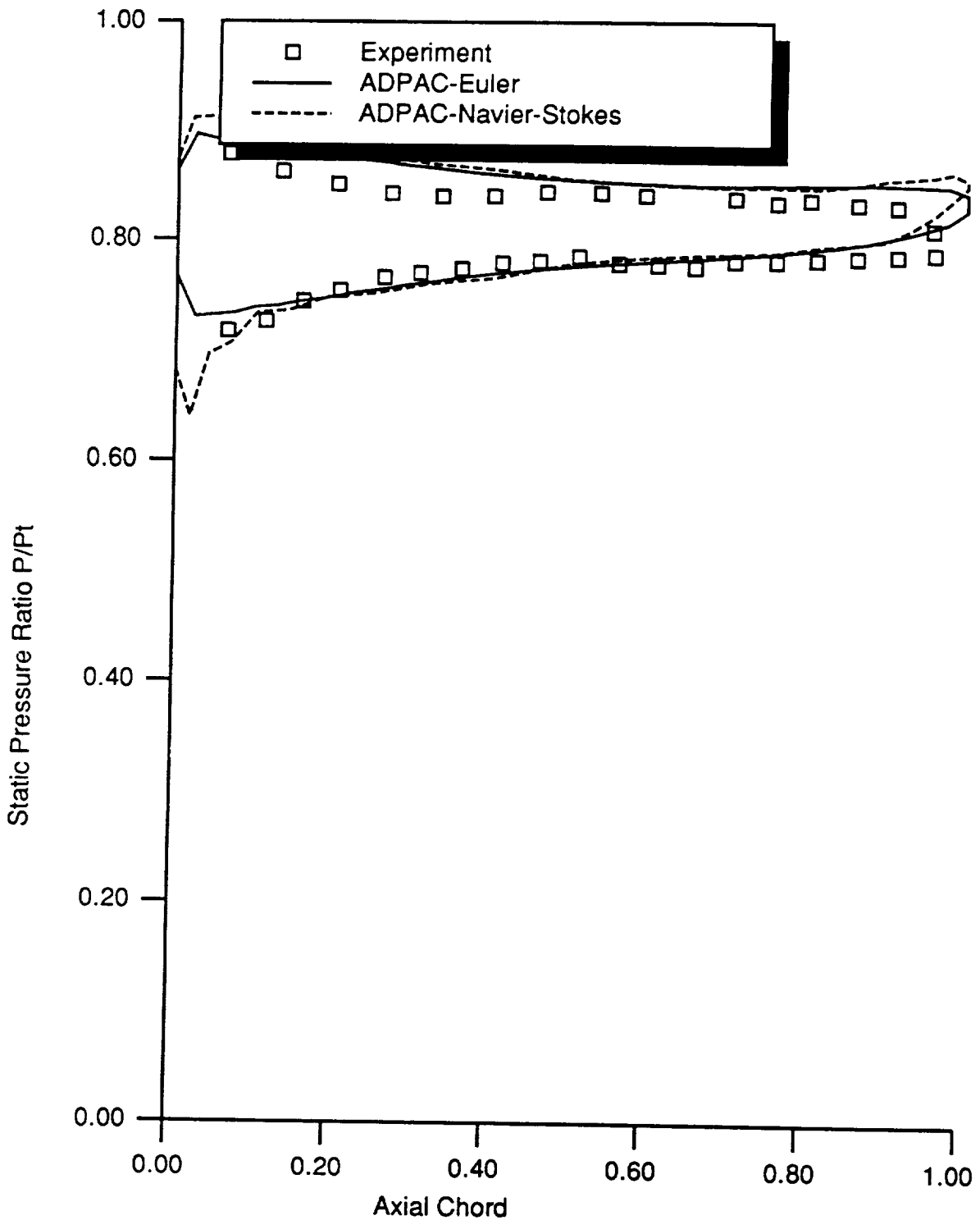


Figure 5.10: Comparison of predicted and experimental airfoil surface static/total pressure ratio distributions for 2-bladed SR7 propfan (94.4% span, $M=0.5$, $J=3.06$).

(camber) surface in Figs. 5.11-5.12, respectively. The inviscid coarse grid prediction is observed to be reasonably accurate in the region downstream of the blade leading edge, but fails to correctly predict the amplitude of the unsteady pressure fluctuations in the vicinity of the leading edge. This is clearly attributable to insufficient grid resolution, as both the viscous and inviscid fine grid results more closely match the experimental data. This trend is evident in nearly every data comparison for this case. A similar set of plots is given at 64% span and 4.9%, 10.0%, and 63.3% chord for the airfoil pressure (face) surface in Figs. 5.13-5.15, respectively. The comparison of time-dependent pressure histories at 4.9% span in Fig. 5.13 is disturbing, since the fine grid solutions show a larger deviation from the experimental measurements than the coarse grid results. This deviation becomes even more perplexing due to the excellent agreement with experimental data at 10.0% chord given in Fig. 5.14. Based on these observations, it was concluded that the deviation in Fig. 5.13 was due either to experimental error, or is a result of some flow phenomena which is not adequately simulated (such as a flow separation or time-dependent vortex development) in the present solution strategy. Further comparisons of predicted and experimental data for the two-blade SR7 propfan suction surface at 91% span and 27.9% and 69.8% chord are given in Figs. 5.16-5.17, respectively. Again, the fine grid results show very good agreement with the experimental data, especially near the leading edge, where pressure fluctuations are at a maximum. Finally, a similar comparison is given for the pressure surface at 91% span at 27.9% and 89.8% chord in Figs. 5.18-5.19, respectively. It was observed that the predicted results demonstrate a slight phase shift compared to the experimental data which is accentuated in the comparisons at the

outer (91%) spanwise locations. It appears that the use of the fine grid in the numerical calculation reduces this phase shift in most cases. The difference between the experimental and calculation blade shapes under aerodynamic and rotational loading could also be a factor in this discrepancy. An illustration of the three-dimensional viscous flow resulting for this case is given in Fig. 5.20. This figure illustrates the 2-bladed propfan shaded by instantaneous static pressure color contours and particle trajectories emanating from the blade tips. The asymmetric aerodynamic loading induced on the propfan spinner and hub by the angle of attack is clearly evident, as is the upsweep of the instantaneous particle trajectories from the blade tips. The viscous flow results for this case did not differ significantly from the fine grid inviscid flow results, presumably because no significant viscous flow phenomena (massive flow separation, vortical development, etc.) are present during the unsteady cycle at this operating condition. A more interesting comparison would likely result for larger angles of attack or increased blade loading levels, both of which will be areas for future investigation.

5.2 SR7 8-Bladed Propfan

A second unsteady calculation for the SR7 propfan blade geometry was performed for the full 8-bladed propfan configuration. Steady state inviscid calculations based on this geometry were performed over a wide range of advance ratios and blade setting angles for flight Mach numbers of 0.7 and 0.8 under Task I of this contract [10].

This test, based on the SR7 8-bladed propfan geometry, corresponds to the numerical test results presented by Nallasamy and Groeneweg [12]. Nallasamy and

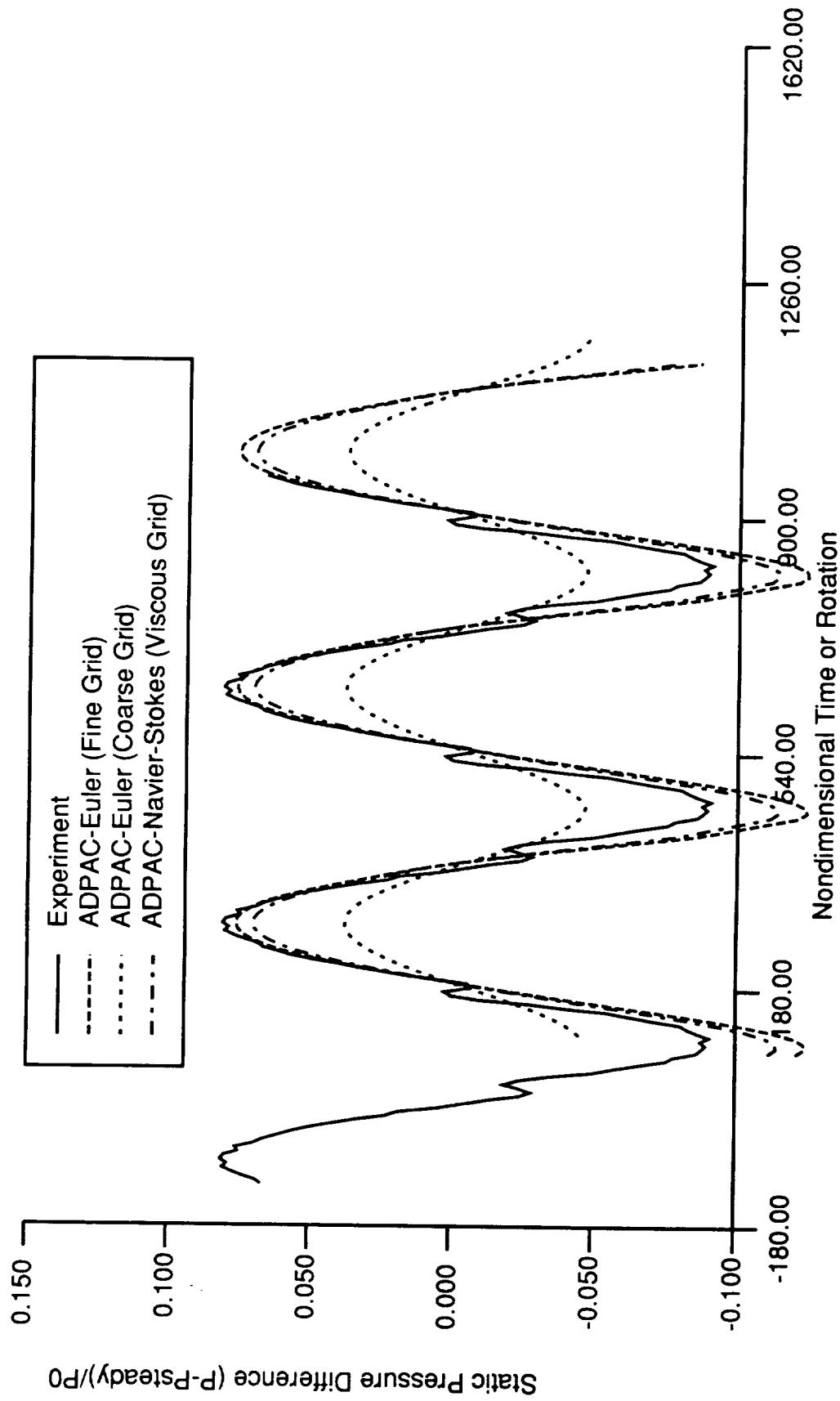


Figure 5.11: Comparison of predicted and experimental airfoil surface time-dependent static/total pressure ratio history for 2-bladed SR7 propfan (suction side, 4.9% chord, 64.0% span, 3 degrees angle of attack)

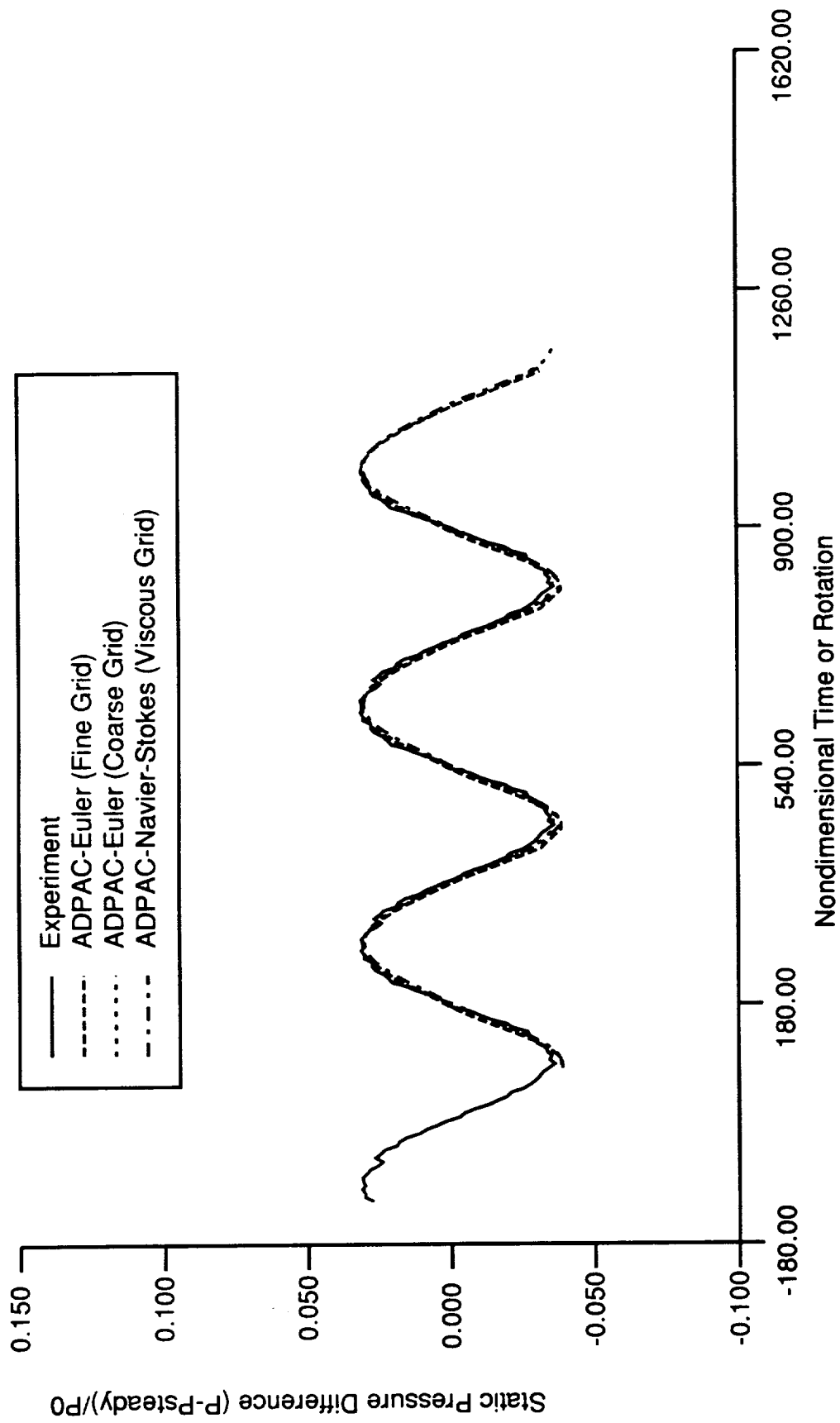


Figure 5.12: Comparison of predicted and experimental airfoil surface time-dependent static/total pressure ratio history for 2-bladed SR7 propfan (suction side, 36.7% chord, 64.0% span, 3 degrees angle of attack)

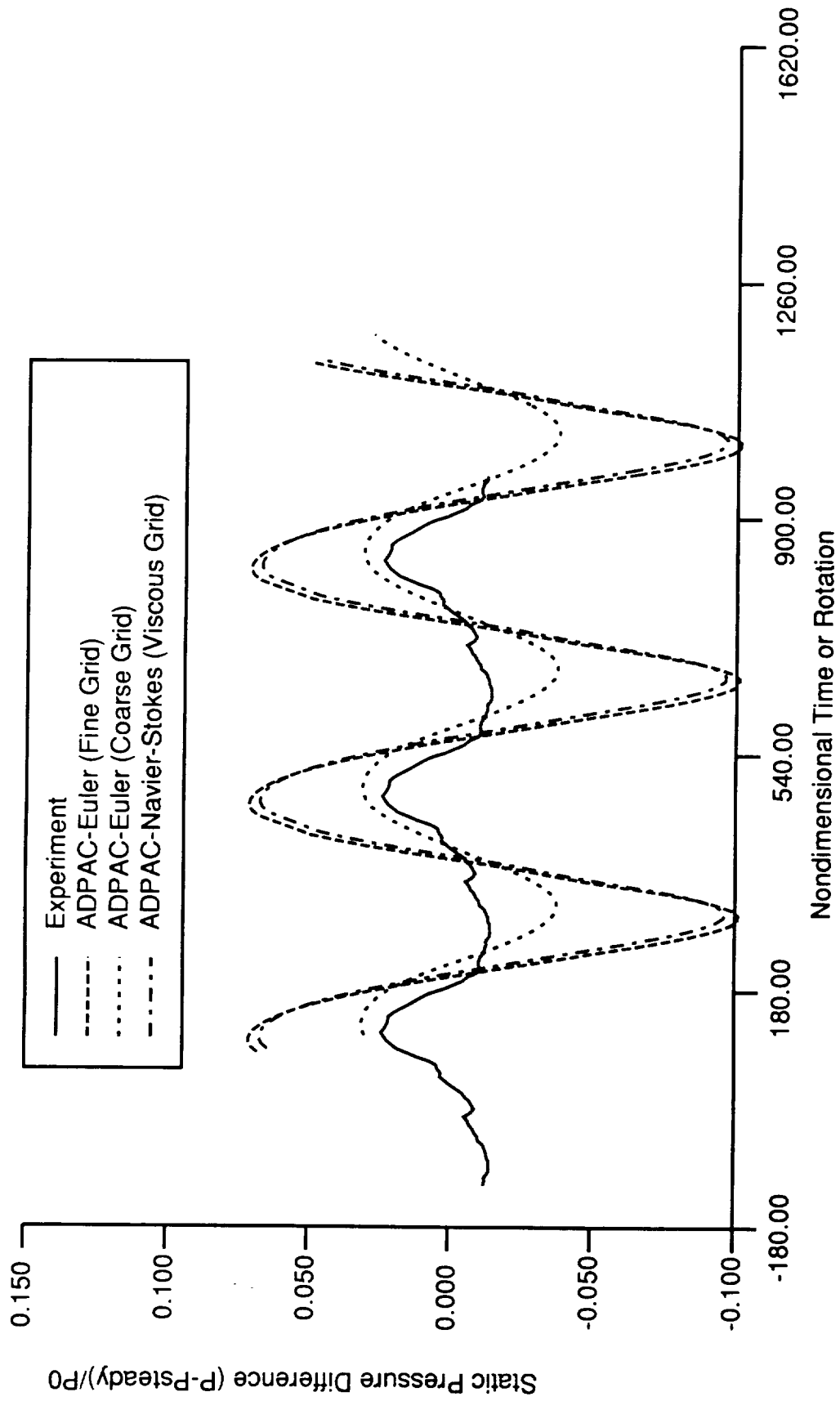


Figure 5.13: Comparison of predicted and experimental airfoil surface time-dependent static/total pressure ratio history for 2-bladed SR7 propfan (pressure side, 4.9% chord, 64.0% span, 3 degrees angle of attack)

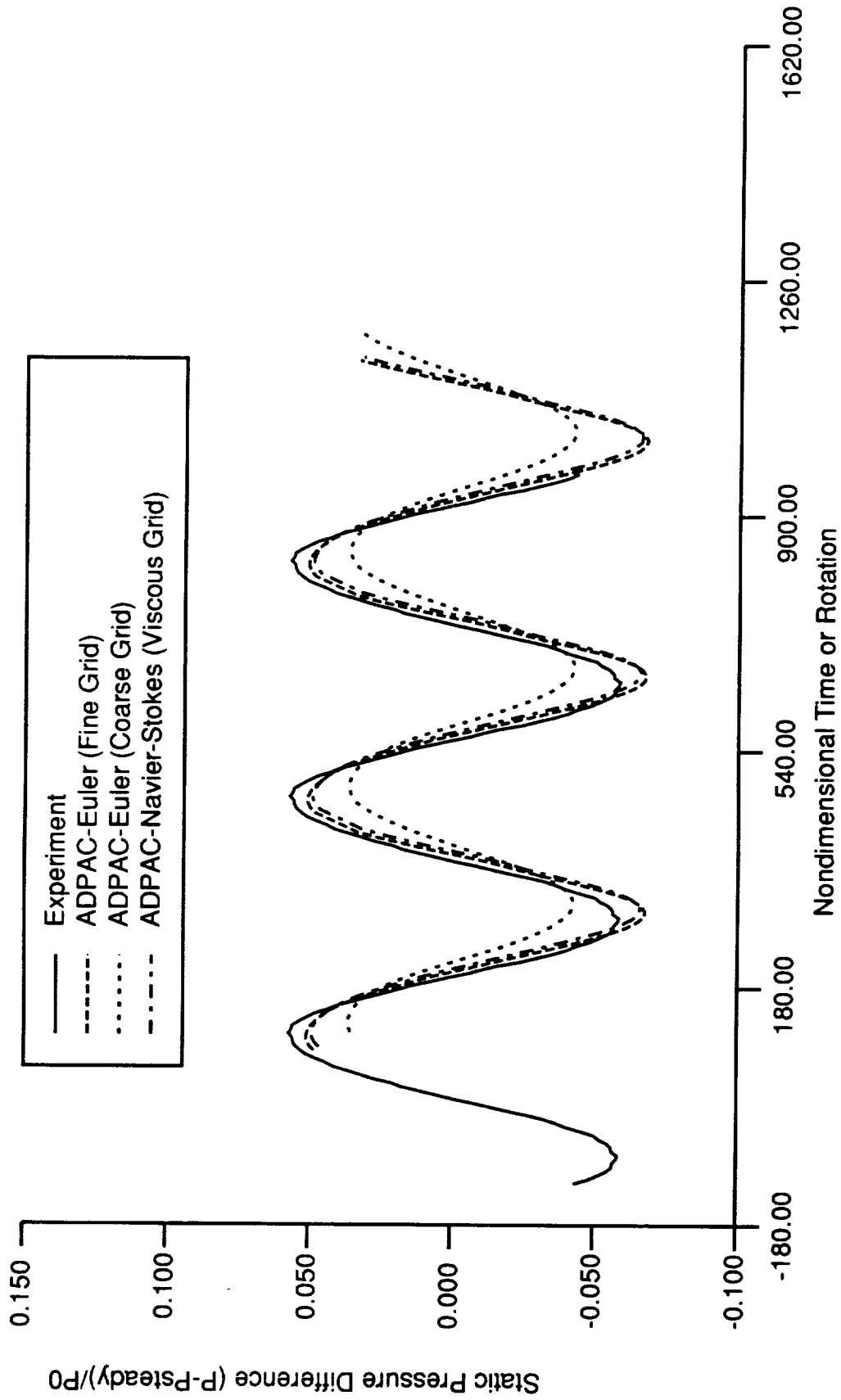


Figure 5.14: Comparison of predicted and experimental airfoil surface time-dependent static/total pressure ratio history for 2-bladed SR7 propfan (pressure side, 10.0% chord, 64.0% span, 3 degrees angle of attack)

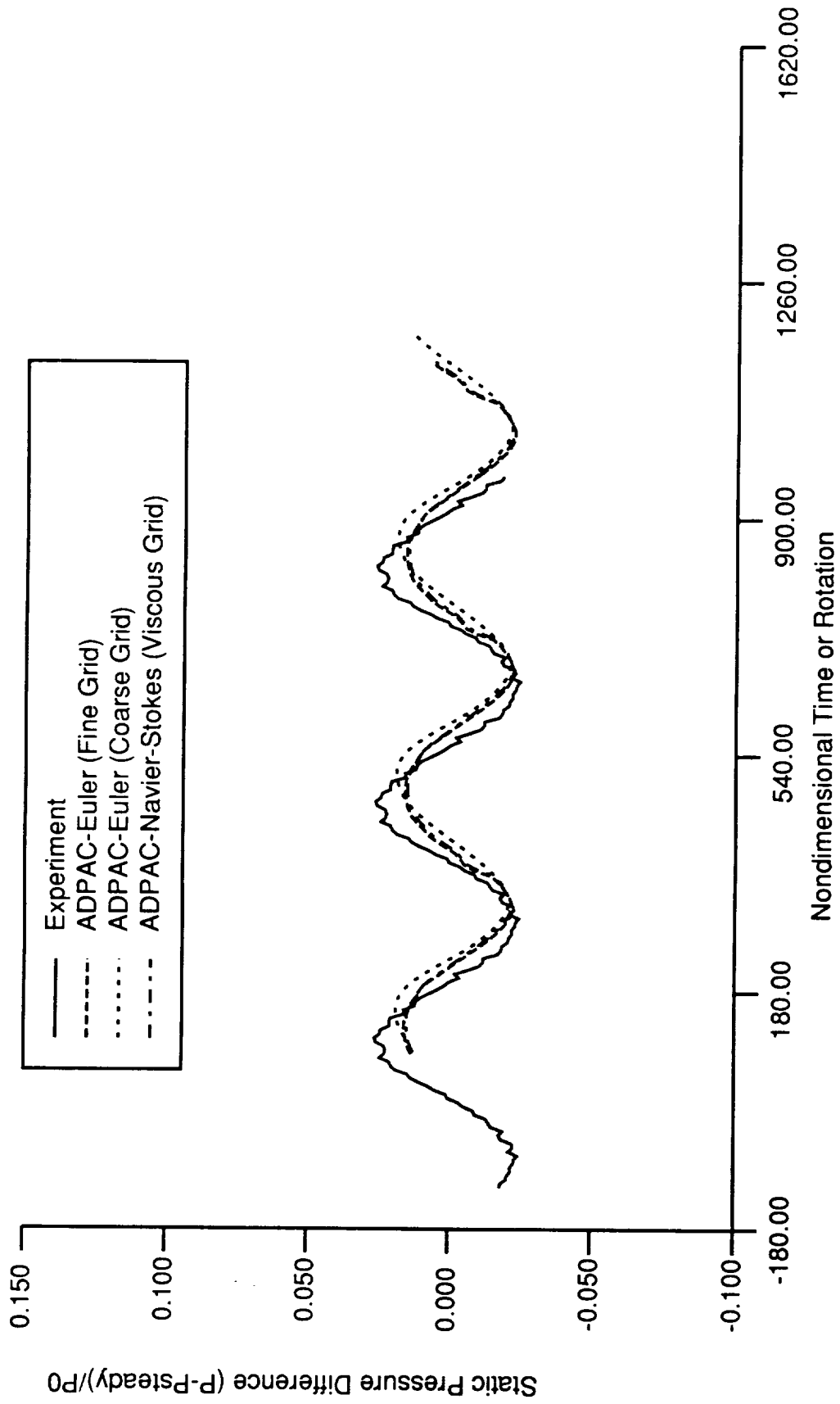


Figure 5.15: Comparison of predicted and experimental airfoil surface time-dependent static/total pressure ratio history for 2-bladed SR7 propfan (pressure side, 63.3% chord, 64.0% span, 3 degrees angle of attack)

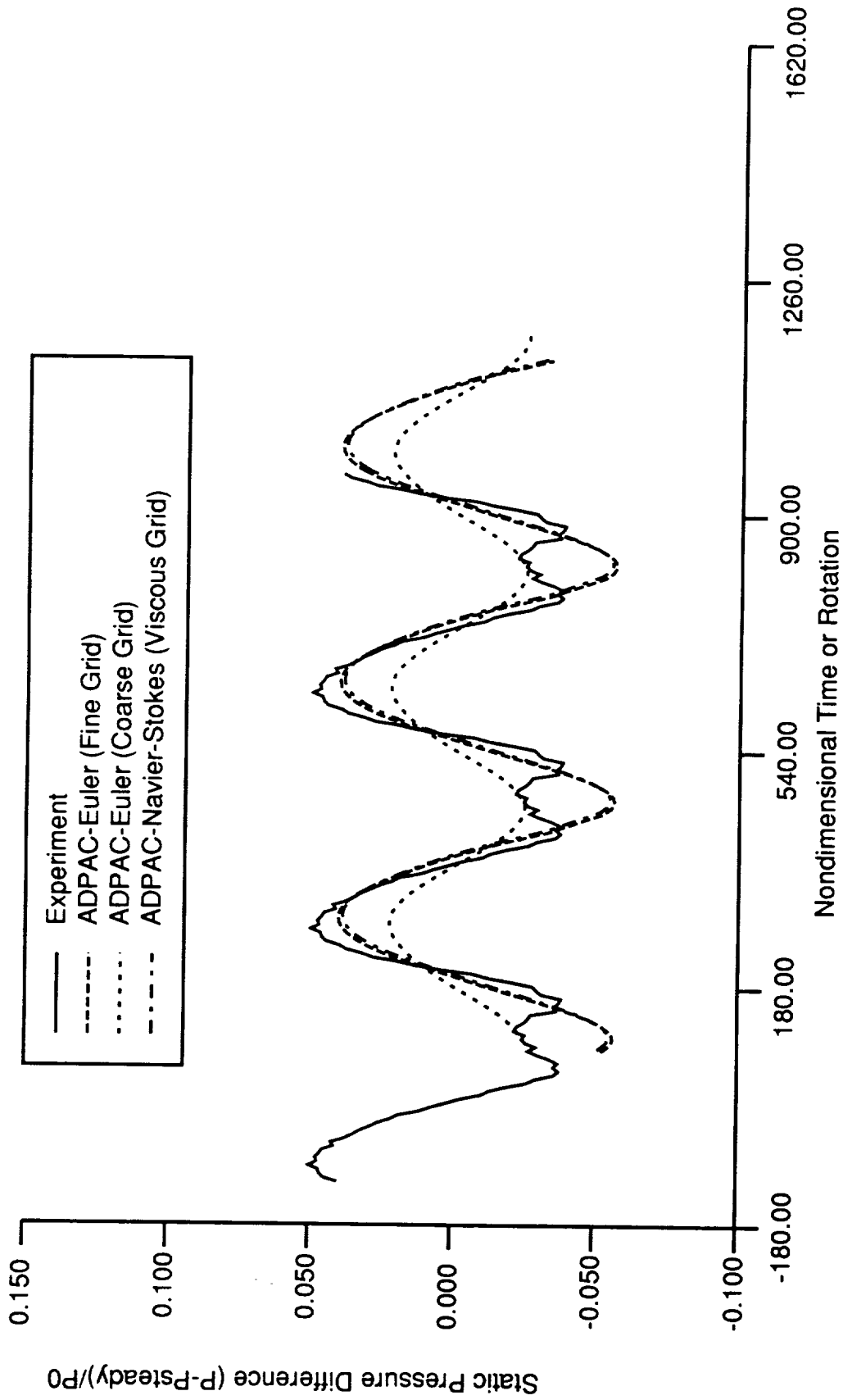


Figure 5.16: Comparison of predicted and experimental airfoil surface time-dependent static/total pressure ratio history for 2-bladed SR7 propfan (suction side, 27.9% chord, 91.0% span, 3 degrees angle of attack)

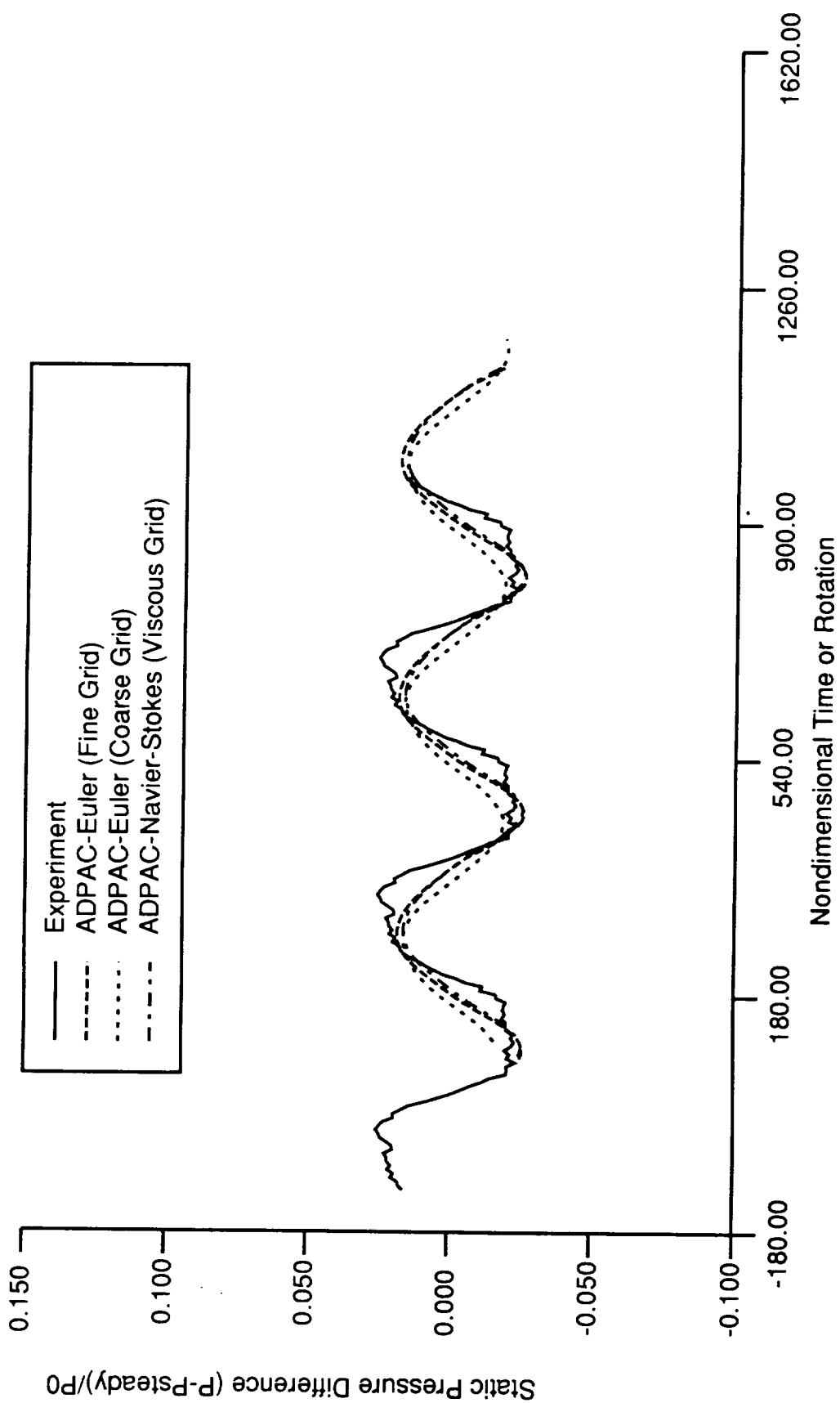


Figure 5.17: Comparison of predicted and experimental airfoil surface time-dependent static/total pressure ratio history for 2-bladed SR7 propfan (suction side, 69.8% chord, 91.0% span, 3 degrees angle of attack)

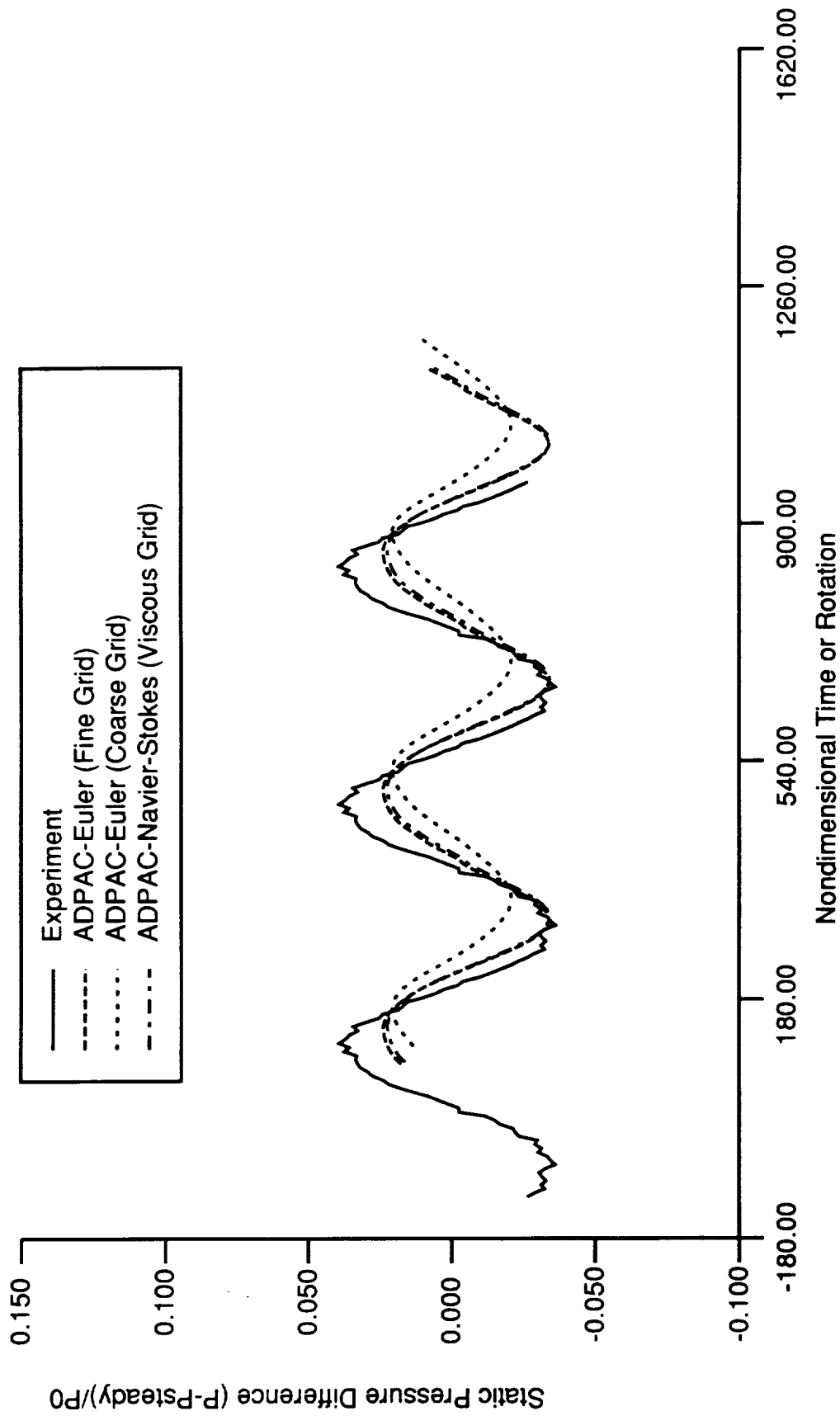


Figure 5.18: Comparison of predicted and experimental airfoil surface time-dependent static/total pressure ratio history for 2-bladed SR7 propfan (pressure side, 27.9% chord, 91.0% span, 3 degrees angle of attack)

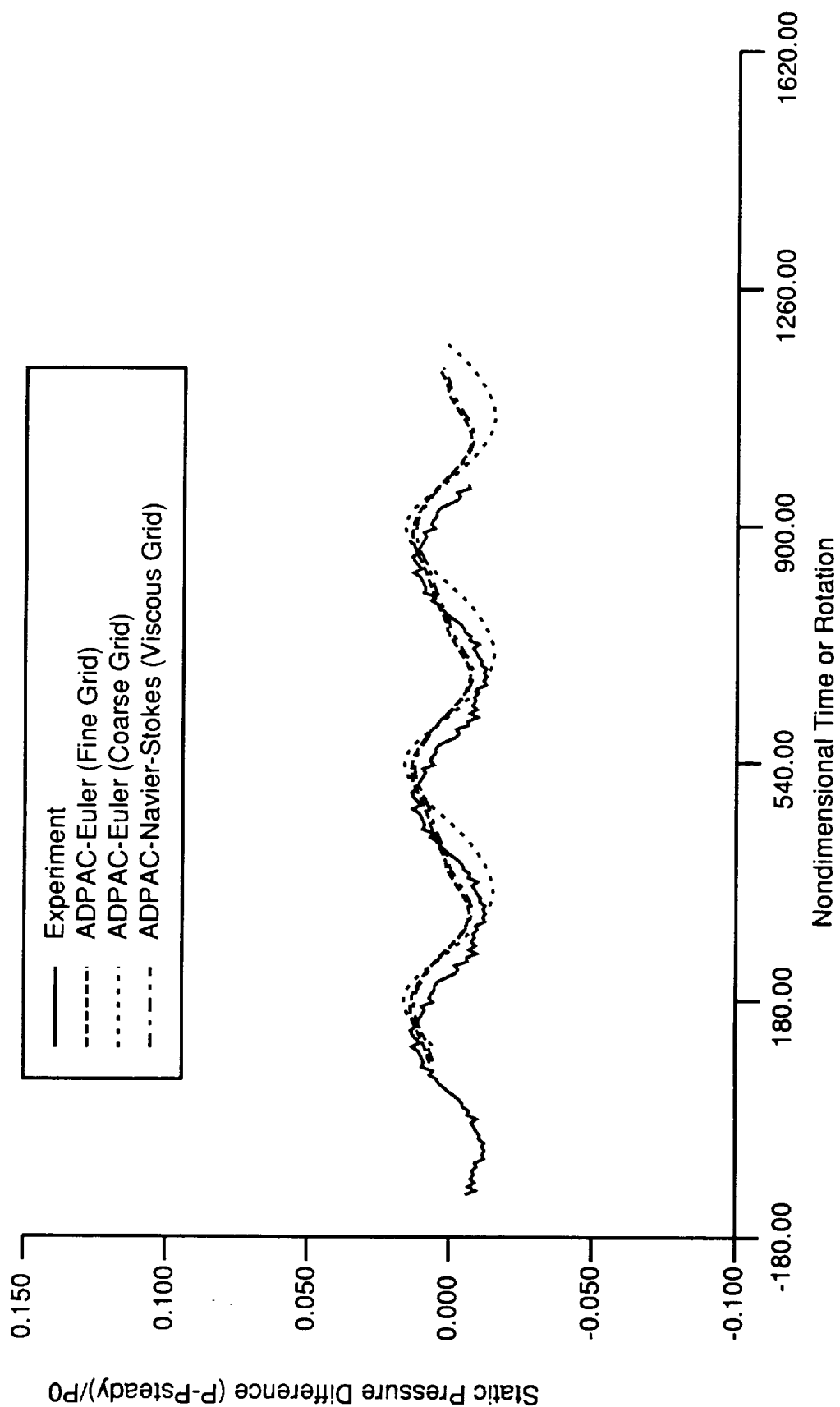


Figure 5.19: Comparison of predicted and experimental airfoil surface time-dependent static/total pressure ratio history for 2-bladed SR7 propfan (pressure side, 89.8% chord, 91.0% span, 3 degrees angle of attack)

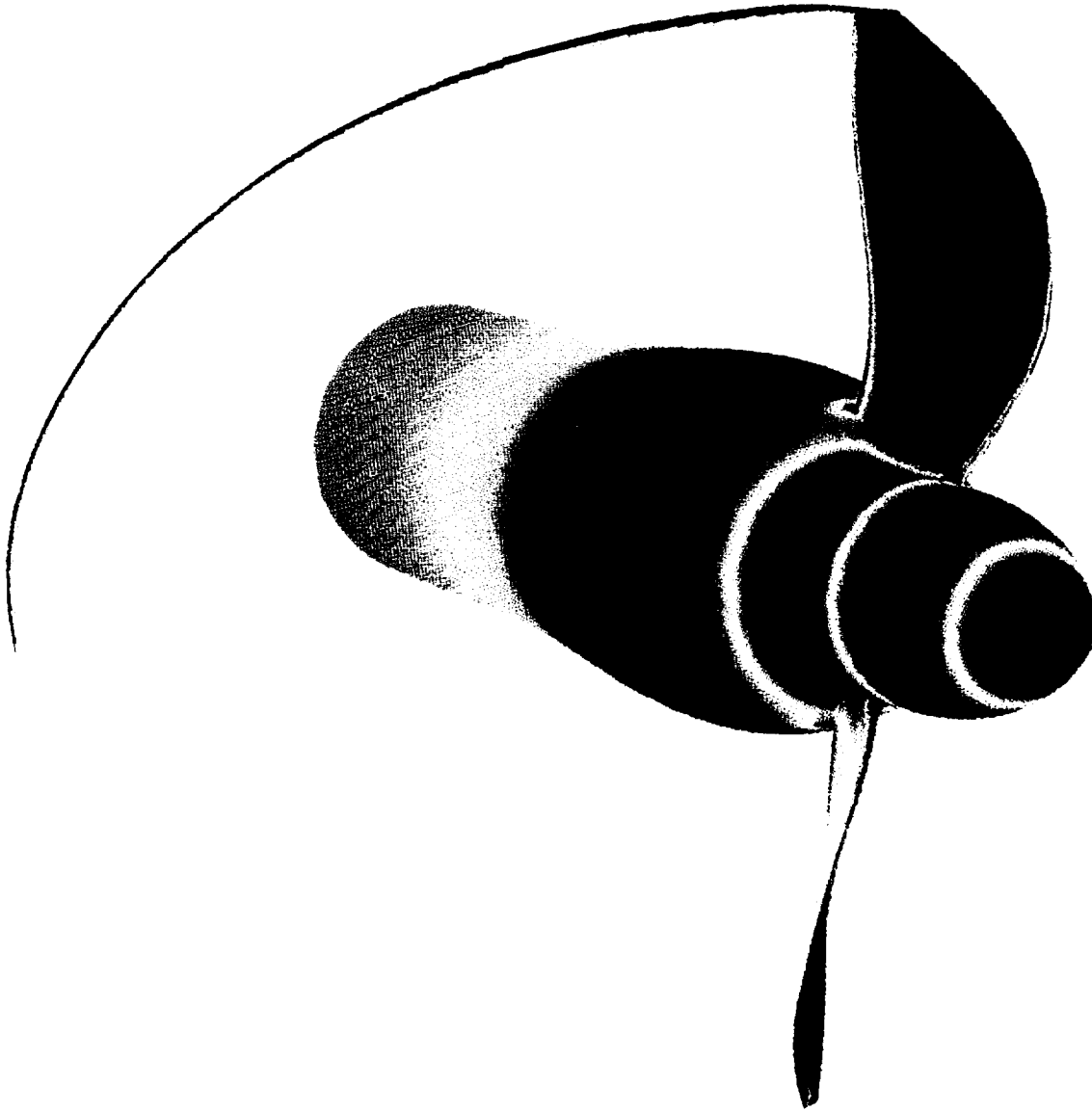


Figure 5.20: Instantaneous propfan surface static/total pressure ratio contours and blade tip particle trajectories for 2-bladed SR7 propfan at angle of attack ($M=0.5$, $J=3.06$, angle of attack = 3 degrees).

Groeneweg predicted the unsteady inviscid flow about an 8-bladed SR7 propfan at a Mach number of 0.8, advance ratio of 3.12, and 4.6 degrees angle of attack. The 3/4 radius blade setting angle was 60.2 degrees. Their predictions for this case indicated the time-dependent formation of a passage shock which develops during the downward (into the angled freestream) motion of the propeller. The shock wave ultimately moves forward through the blade passage, and then dissipates as the propeller begins to swing upward (away from the angled freestream). Although no experimental data were available for comparison, the unsteady shock motion and previous predictions make this an interesting case to study.

An unsteady inviscid calculation was performed for this unducted propfan on a system of numerical grids containing 8 blocks (one for each blade passage). The grid system utilized a total of 237,160 points as shown in Fig. 5.21. Instantaneous static pressure contour plots of a blade-to-blade grid surface corresponding to roughly 50% span are given for each of the eight blade passages consecutively in the direction of rotation in Figs. 5.22(a)- 5.22(h), respectively for the inviscid flow prediction. These plots serve to illustrate the differences in blade passage pressure during each blade pitch rotation of the propfan. The passages begin about one blade pitch before top dead center and continue in the direction of rotation into the downward sweep. The convergence of the contours in Figs. 5.22(a)- 5.22(c) clearly illustrates the formation of the passage shock. Figs. 5.22(d)- 5.22(f) portray the motion and simultaneous dissipation of the shock as it moves forward through the passage, until it ultimately disappears and renews the time-dependent cycle (Fig. 5.22(h)). This sequence is qualitatively identical to the observations reported by Nallasamy and Groeneweg [12]

in their calculations. An instantaneous depiction of the predicted propfan surface static/total pressure ratio contours is given in Fig 5.23. The asymmetric hub loading and blade passage shock movement are all easily identifiable in the color contours. Of particular interest is the noticable change in blade leading edge stagnation point at the airfoil root due to the angled freestream. It would appear that the root airfoil section should be particularly insensitive to incidence angle for good off-design performance.

A rotational history of the predicted single blade power coefficient history is given in Fig. 5.24(a). A reproduction of a similar plot from Ref. [12] is also illustrated in Fig. 5.24(b) for comparison. The present prediction is in good qualitative agreement with Nallasamy and Groeneweg's results. Quantitatively, the *ADPAC* results indicate a slightly larger peak to peak variation in the single blade power coefficient history. This discrepancy is more than likely due to a combination of effects resulting from differences in grid resolution, numerical damping, and/or time step size between the two calculations.

5.3 Ducted Propfan Test Case

Since the ducted propfan is a relatively new area of investigation, there are few available experimental or numerical data upon which the present algorithm may be compared. Calculations based on existing fan geometries do little to illustrate the aerodynamics of advanced ducted propfan geometries, and therefore an unsteady calculation based on a fictitious geometry is initially examined here. The test geometry was developed based on the SR7 blade geometry. Since propfan design philosophy utilizes cascade flow concepts for the root airfoil sections, it is unlikely that the ad-

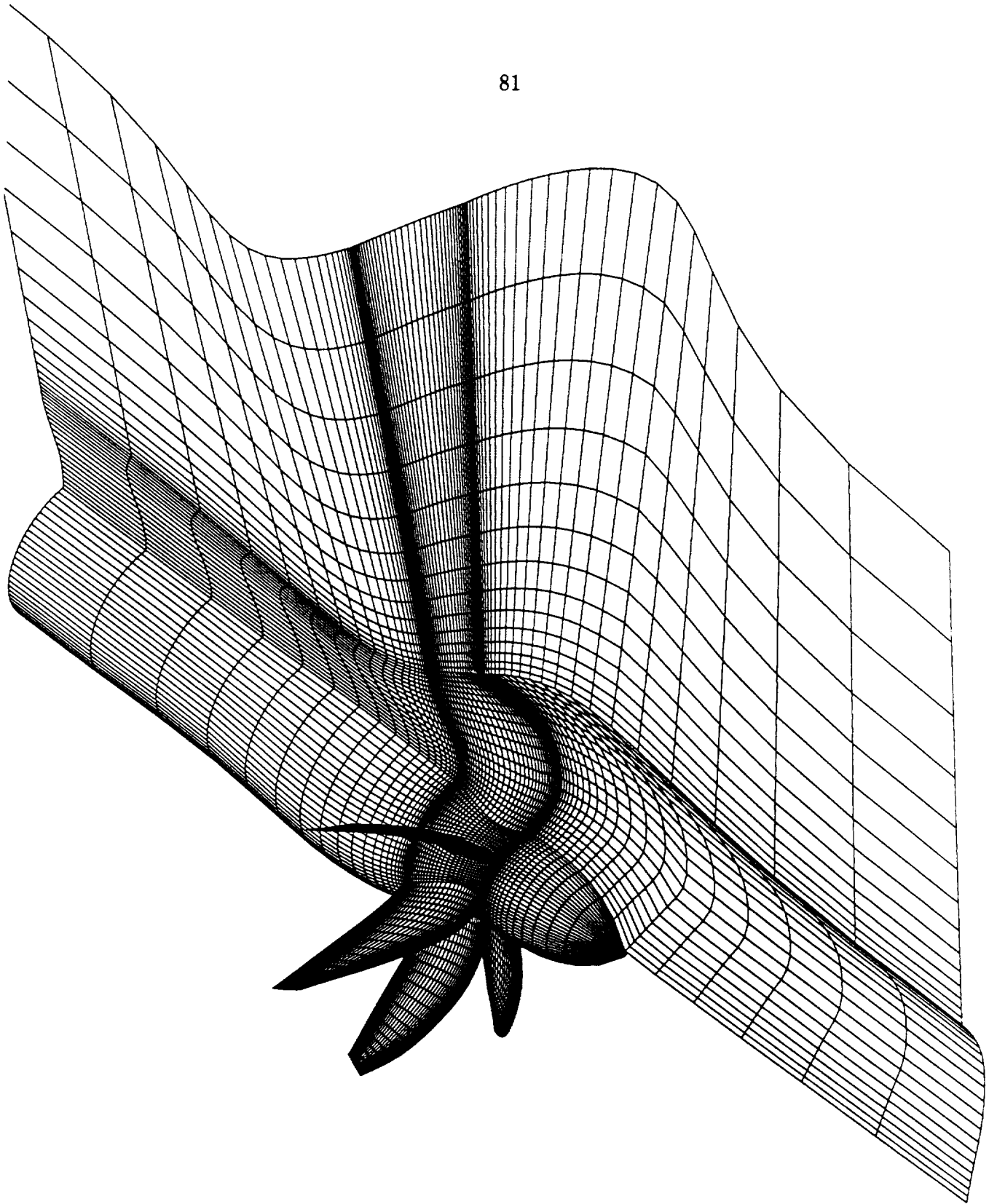


Figure 5.21: Full rotor grid for SR7 time-dependent inviscid calculations

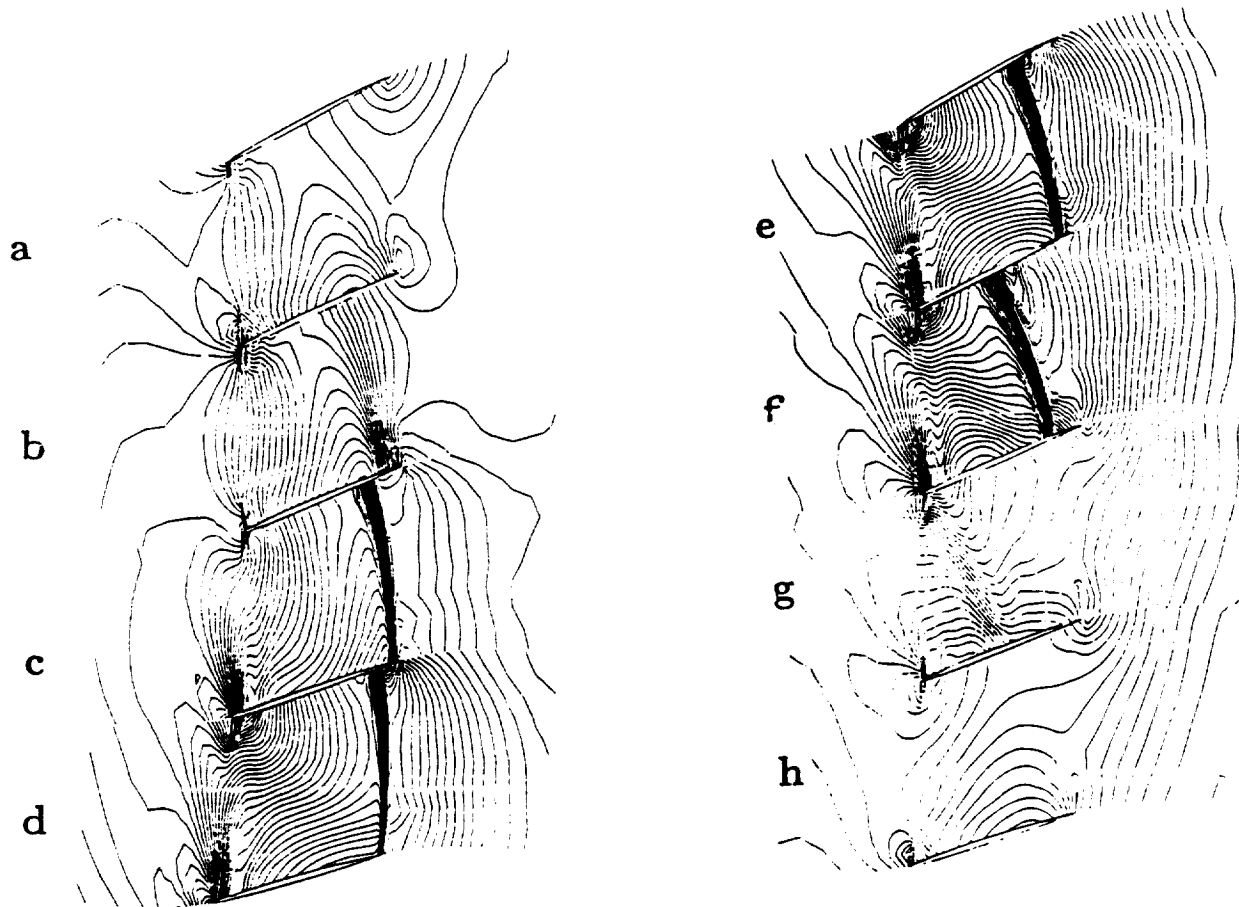


Figure 5.22: Predicted instantaneous propfan inviscid blade passage static pressure contours for 8-bladed SR7 propfan at angle of attack ($M=0.8$)

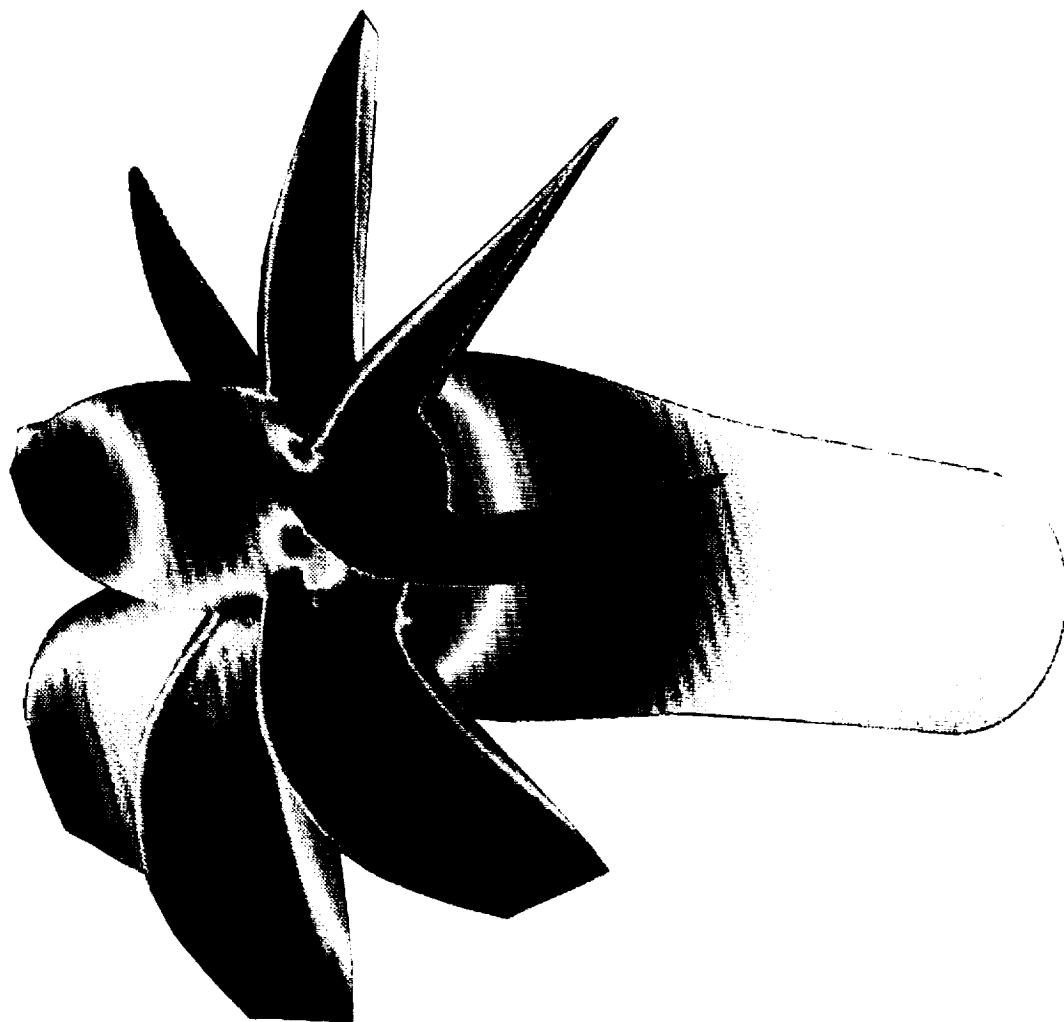


Figure 5.23: Predicted instantaneous propfan surface static/total pressure ratio contours for 8-bladed SR7 propfan at angle of attack ($M=0.8$, angle of attack = 4.6 degrees)

ORIGINAL PAGE
COLOR PHOTOGRAPH

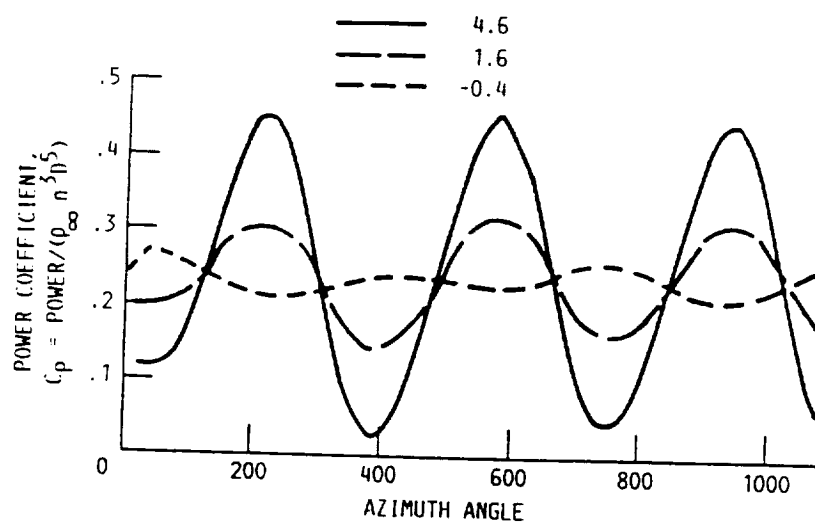
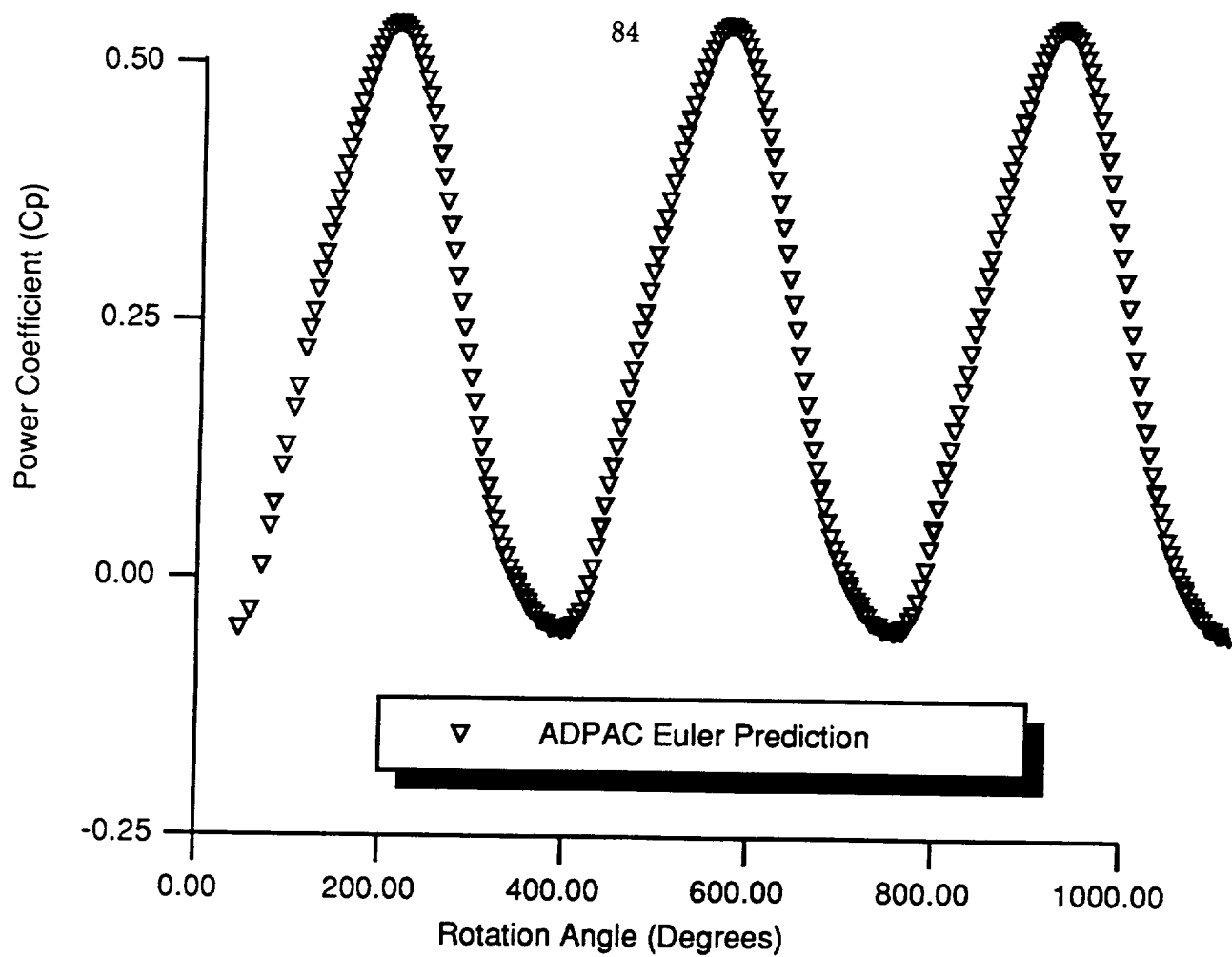


Figure 5.24: Predicted rotational single blade power coefficient histories for 8-bladed SR7 propfan at angle of attack ($M=0.8$, angle of attack = 4.6 degrees)

dition of an outer duct would significantly effect the aerodynamics in this region, so this geometry was unaltered. However, the near tip region of the blade is not likely to be adequately suited for ducting, and, therefore, the blade geometry was created by discarding the outer 20% of the SR7 airfoil, and enclosing this clipped eight-bladed propfan in a low profile duct. The length of the duct was chosen to be representative of a high bypass ratio unmixed exhaust flow ducted propfan configuration. This geometry is conceptually equivalent to the types of designs expected for the ducted propfan concept.

Inviscid aerodynamic calculations were again performed for both a coarse grid and a fine grid solution for the ducted SR7 geometry at a Mach number of 0.8, advance ratio of 3.06, and 5 degrees angle of attack. Again, the $3/4$ radius blade setting angle was 60.2 degrees. Only the results from the fine grid solution are presented here.

The fine grid solution employed 450,000 grid points and is illustrated in Fig. 5.25. For this configuration, the mesh was comprised of 40 separate grid blocks (5 per blade passage). A series of instantaneous blade passage static pressure contour plots at roughly 50% span are given in Figs. 5.26(a)- 5.26(h) for the fine grid calculation. It is immediately obvious that a rather strong passage shock has formed as a result of these flow conditions. It is apparent that the blade setting angle is not optimally adjusted for this case. The shock oscillates slightly during the course of the revolution, but ultimately shows little change as a result of the rotation, and the flow remains choked in each passage throughout the cycle. This is a result, in part, of the flow straightening effect induced by the duct, which aids to minimize the angle of attack flow nonuniformity. Blade surface fluctuations are seen to be significantly reduced

by this streamlining effect. An examination of the overall unsteadiness induced on the propfan blades is illustrated by the surface static pressure unsteady envelope plot given in Fig. 5.27 corresponding to 90% span. The low level of unsteadiness is evident from the thin shaded regions defining the unsteady envelope. The influence of the passage shock clearly dominates this flow and is clearly displayed in the jump in static pressure on the pressure surface at roughly 50% chord. An instantaneous propfan surface static pressure contour plot is given for the fine grid calculation in Fig. 5.28. The asymmetric loading on the spinner and duct leading edges resulting from the angle of attack are clearly evident.

An interesting comparison of unsteady blade loading between an unducted propfan and a ducted propfan is illustrated in Fig. 5.29. Single blade power coefficient rotational history data from the unducted SR7 calculation described in the previous section is compared with predicted data from a second calculation for the ducted SR7 geometry to illustrate the influence of the duct on the time-dependent blade loading. In this second ducted propfan calculation, the blade setting angle was increased 3 degrees to unchoke the flow in the blade passage, and provide a more meaningful comparison of results. The overall power coefficient for each case was roughly equivalent. The solutions indicate that the peak time-dependent loading for the ducted propfan is roughly 30% of that predicted for an equivalently-powered unducted propfan. This observation suggests that the addition of the propfan duct could provide significant reductions in unsteady blade stress levels and propfan generated noise levels resulting from angle of attack over comparable unducted propulsion systems. Further investigation is required to verify this result over a wider range of geometries

and operating conditions.

5.4 NASA 1.15 Pressure Ratio Fan

The final calculations to be presented were performed for a 1.15 pressure ratio fan stage originally tested by NASA [28]-[31] and utilized extensively under this contract for analysis [10]. A description of the geometry and design parameters for the NASA 1.15 pressure ratio fan is given in Fig. 5.30. This fan is representative of a 25:1 bypass ratio turbofan engine fan stage, and therefore closely approximates the ducted propfan concept propulsion system. During the present study, only viscous flow calculations were performed for this geometry, as a detailed presentation of steady state inviscid flow calculations was given in a previous report [10]. For this series of calculations, it was not possible to exactly match the experimentally measured mass flow through the fan due to the expense of iterating on the three-dimensional solution; therefore, predictions are based on the flight Mach number and estimated fan rotational speed alone.

Preliminary steady flow calculations were performed to permit a comparison of predicted results with the high speed experimental data published in Ref. [28]. A meridional view of the geometry and steady flow viscous flow grid system are given in Fig. 5.31. Steady flow calculations were performed for flight Mach numbers of 0.75 and 0.85. The fan rotational speed was based on advance ratios of 2.86 and 3.22 for the 0.75 and 0.85 Mach number cases, respectively. A comparison of the viscous predicted and experimental cowl leading edge surface static pressure ratios is given in Fig. 5.33 for a Mach number of 0.75 and an advance ratio of 2.86. Inviscid

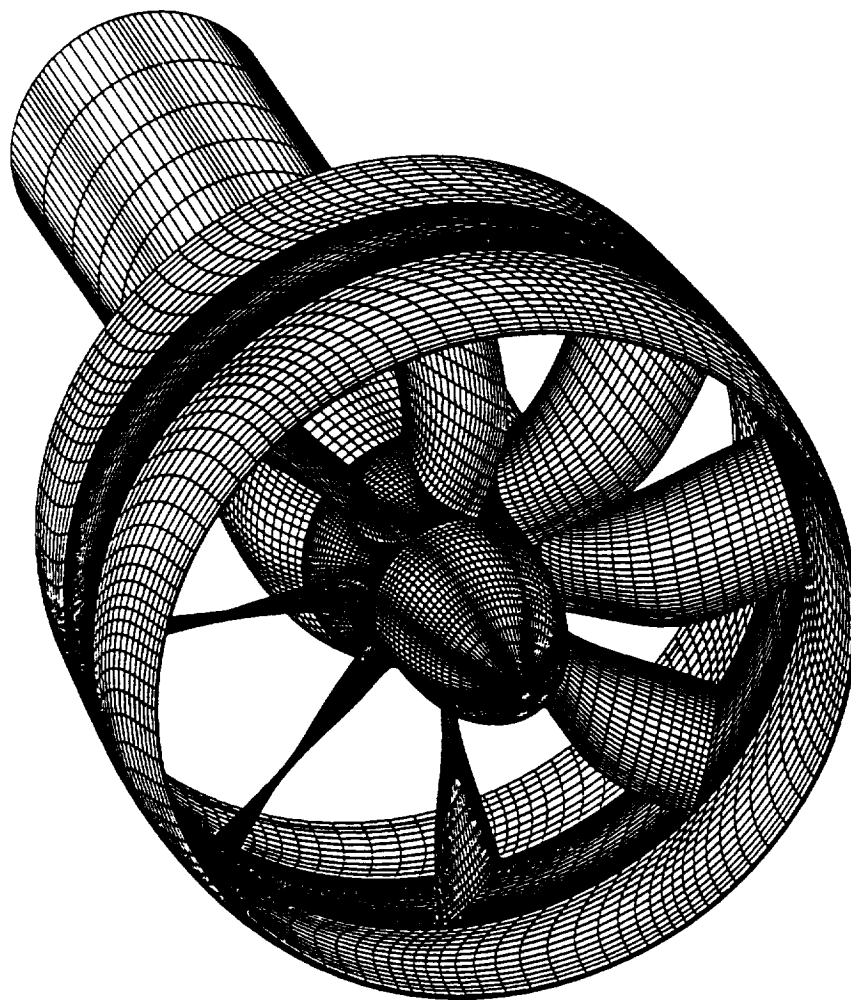


Figure 5.25: Full rotor grid system for ducted SR7 propfan geometry

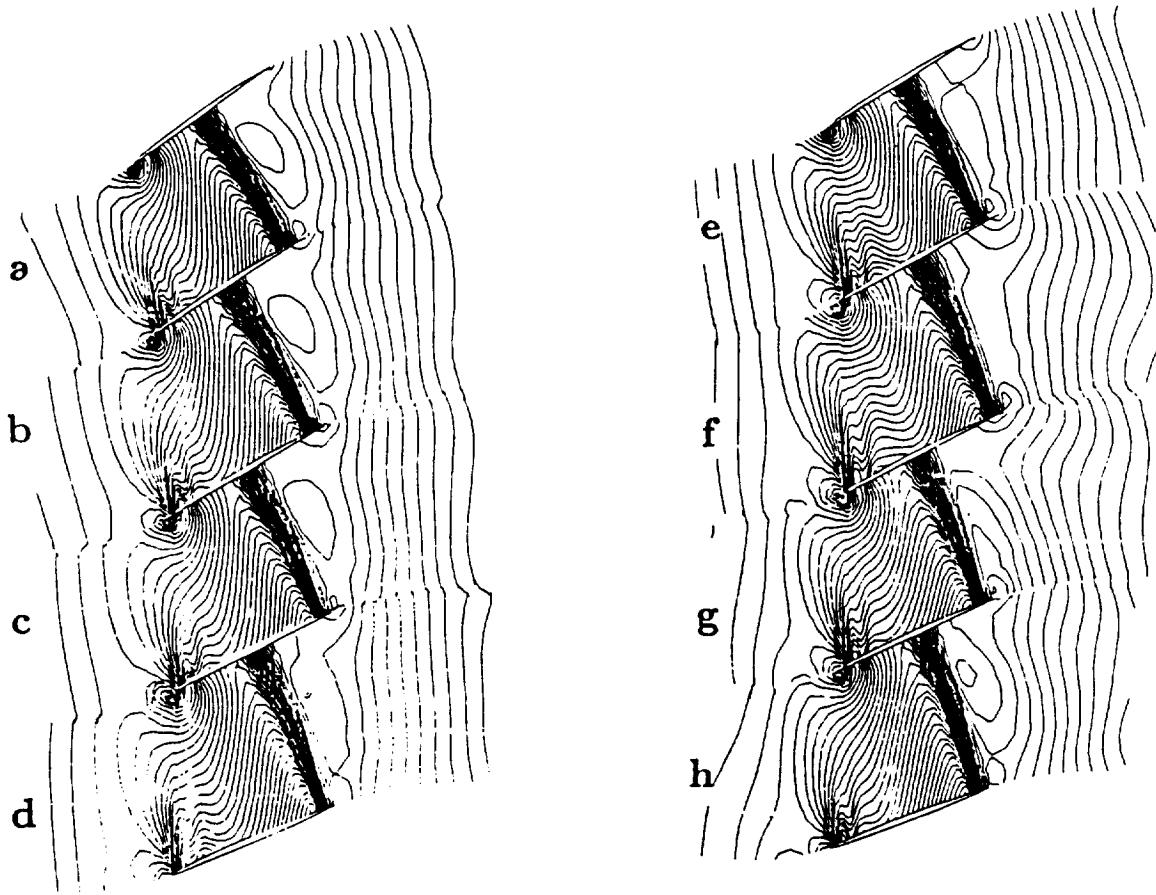


Figure 5.26: Instantaneous blade passage static pressure contours for ducted SR7 propfan geometry ($M=0.8$).

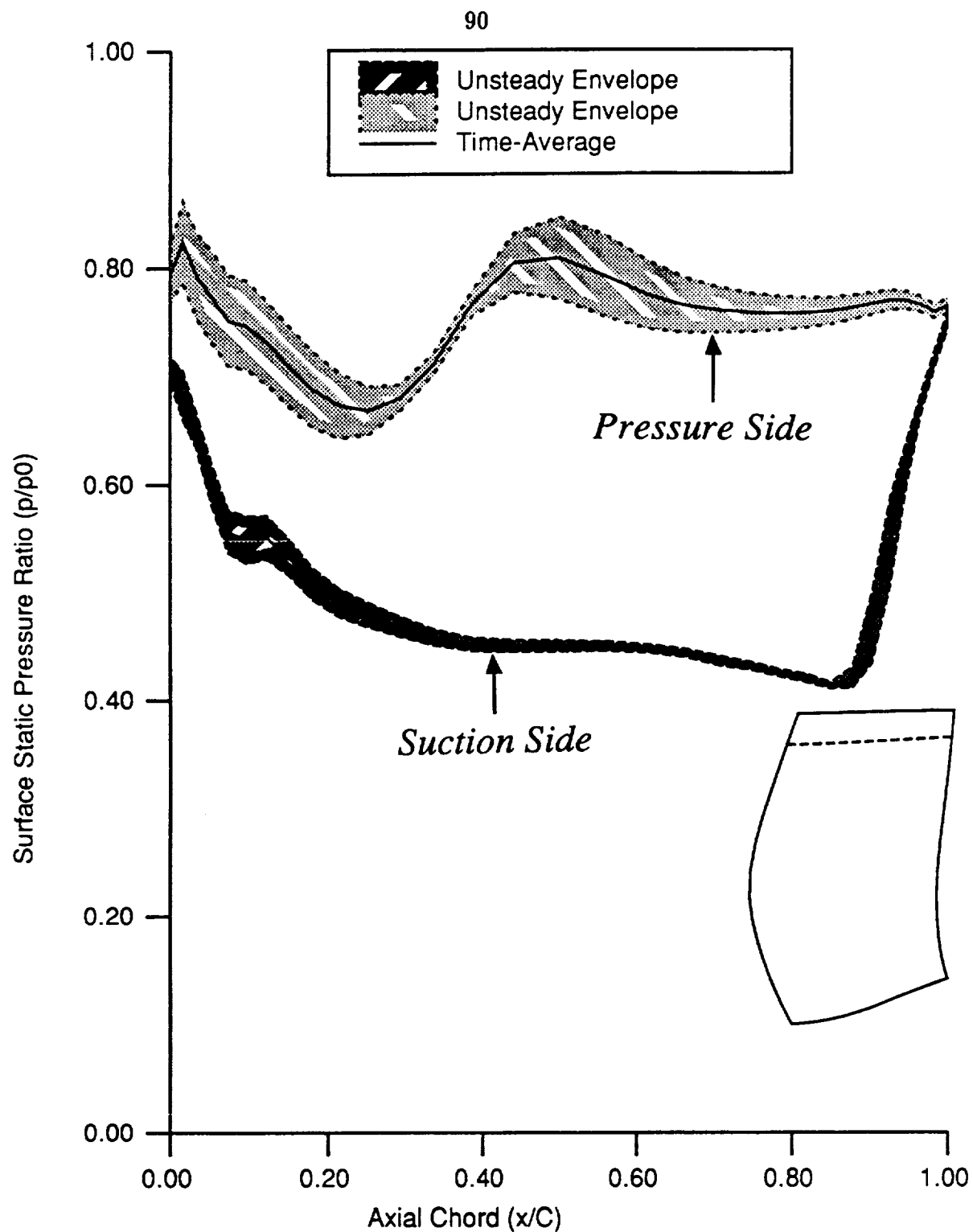


Figure 5.27: Comparison of time-average and unsteady blade section static pressure distributions for ducted SR7 propfan (90% span).

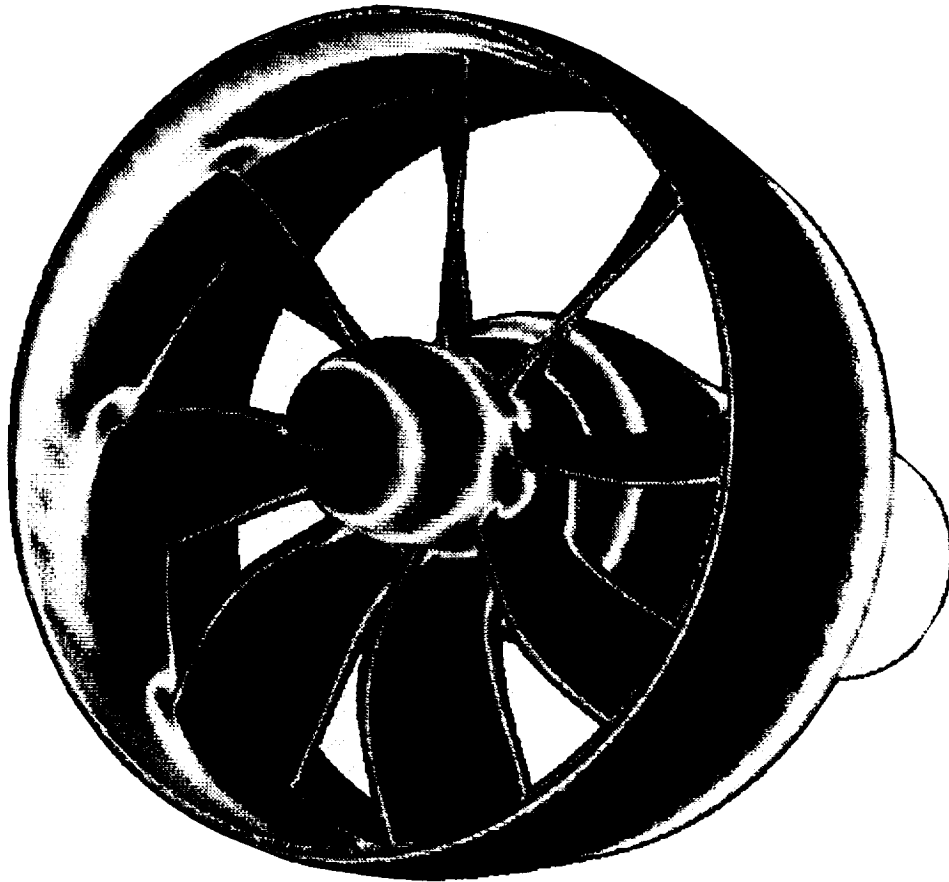


Figure 5.28: Predicted surface static pressure contours for ducted SR7 propfan geometry at angle of attack ($M=0.8$).

ORIGINAL PAGE
COLOR PHOTOGRAPH

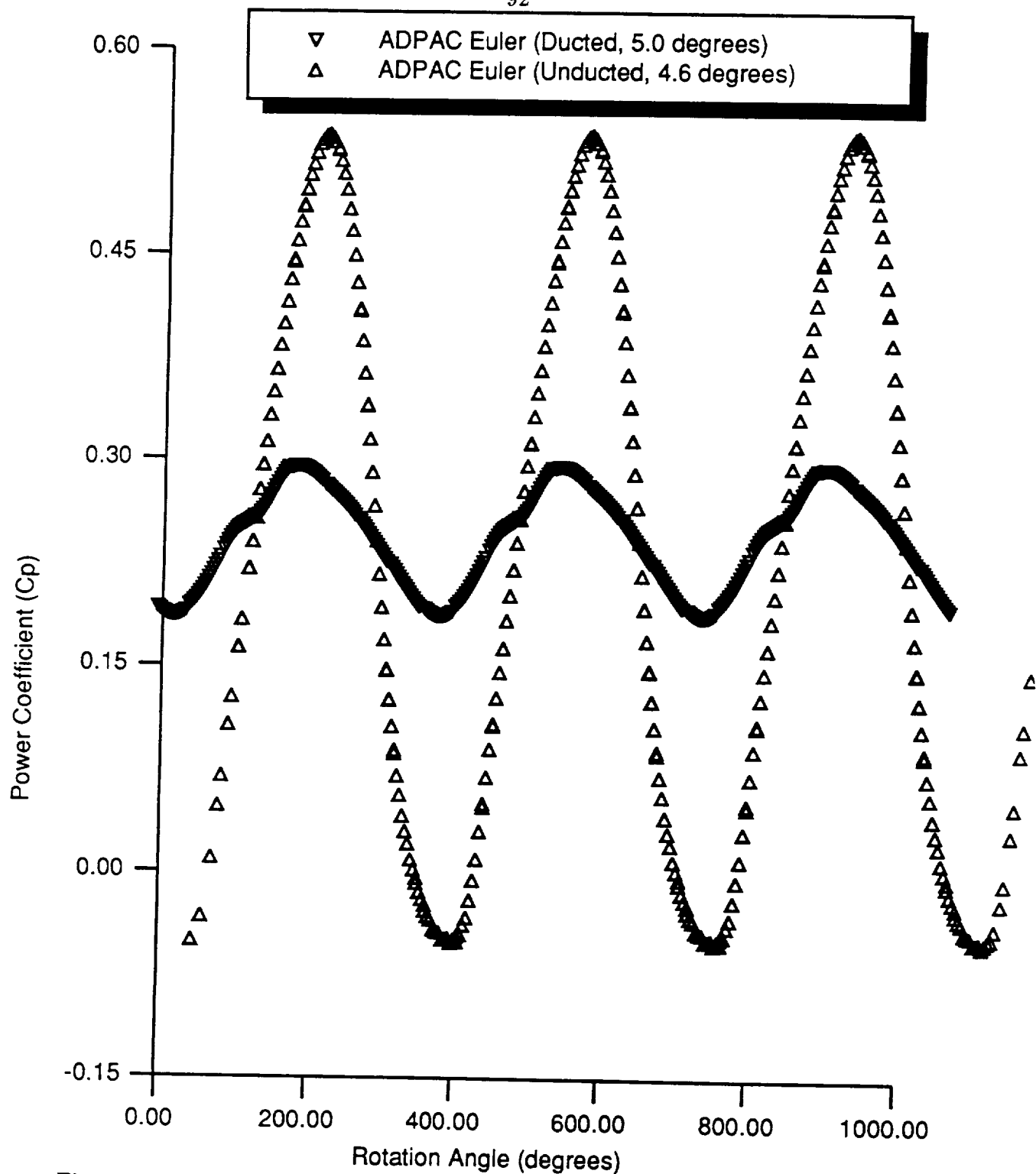


Figure 5.29: Predicted single blade power coefficient rotational histories for ducted and unducted 8-bladed SR7 propfans at angle of attack ($M=0.8$).

results from a previous task [10] of this contract are also presented on Fig. 5.33 for reference. The agreement between experiment and calculation appears to be very good for this case. A similar comparison of results is given for a Mach number of 0.85 and an advance ratio of 3.22 in Fig. 5.34. Again, the viscous results demonstrate good agreement with the experimental data in the high gradient leading edge region. The deviation observed between the inviscid results and the experimental data near the outer downstream edge of the cowl static pressure distribution was previously believed to be due either to a shock-induced flow separation or to a wind tunnel sidewall interference effect. An examination of the predicted viscous flow velocity vectors in this region given in Fig. 5.32 indicates that the flowfield is not separated downstream of the shock, and that the deviation between prediction and experiment is likely due to the wind tunnel sidewall aerodynamic interference.

The final results to be presented are based on a time-dependent viscous flow calculation for the NASA 1.15 pressure ratio fan. The flight Mach number was chosen to be 0.20, and the advance ratio was 1.12. The angle of attack was 40 degrees. These values were selected to permit a comparison with the low-speed experimental data for non-zero angles of attack presented in Ref. [29] for the NASA 1.15 pressure ratio fan. The actual wind tunnel velocity for this data was reported to be 144 ft/s, which corresponds to a Mach number of approximately 0.12. Unmodified compressible flow time-marching schemes typically do not perform well for Mach numbers under 0.2, and therefore the calculation freestream Mach number was rather arbitrarily increased to avoid low Mach number problems in the numerical solution. The results should therefore be interpreted with this discrepancy in mind.

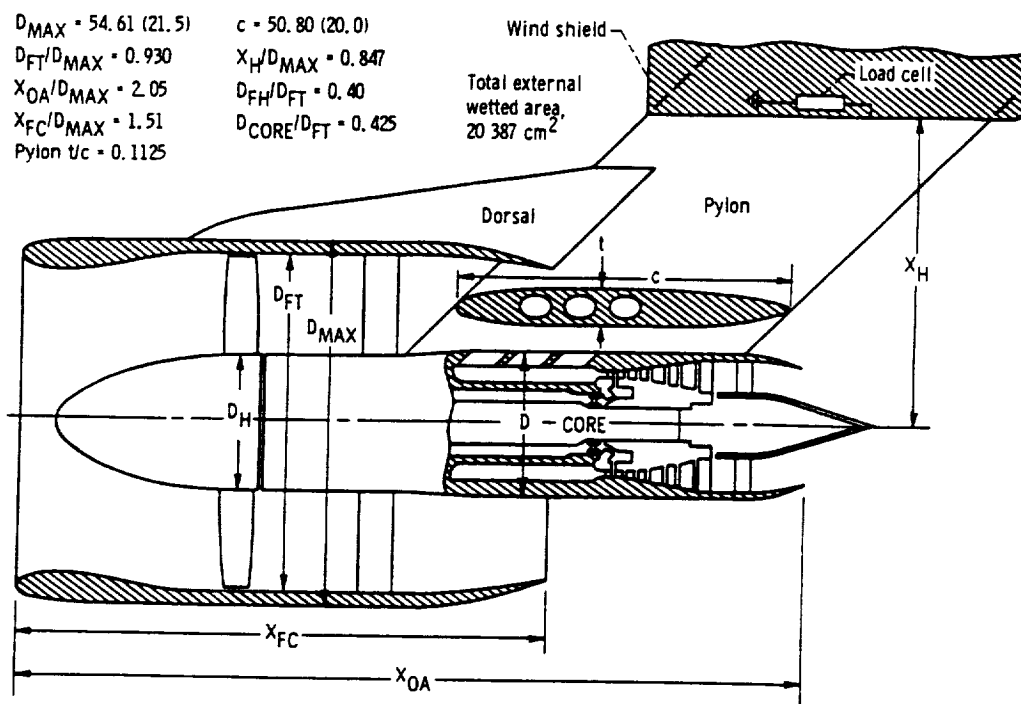


Figure 5.30: NASA 1.15 pressure ratio fan stage geometry (dimensions in cm)

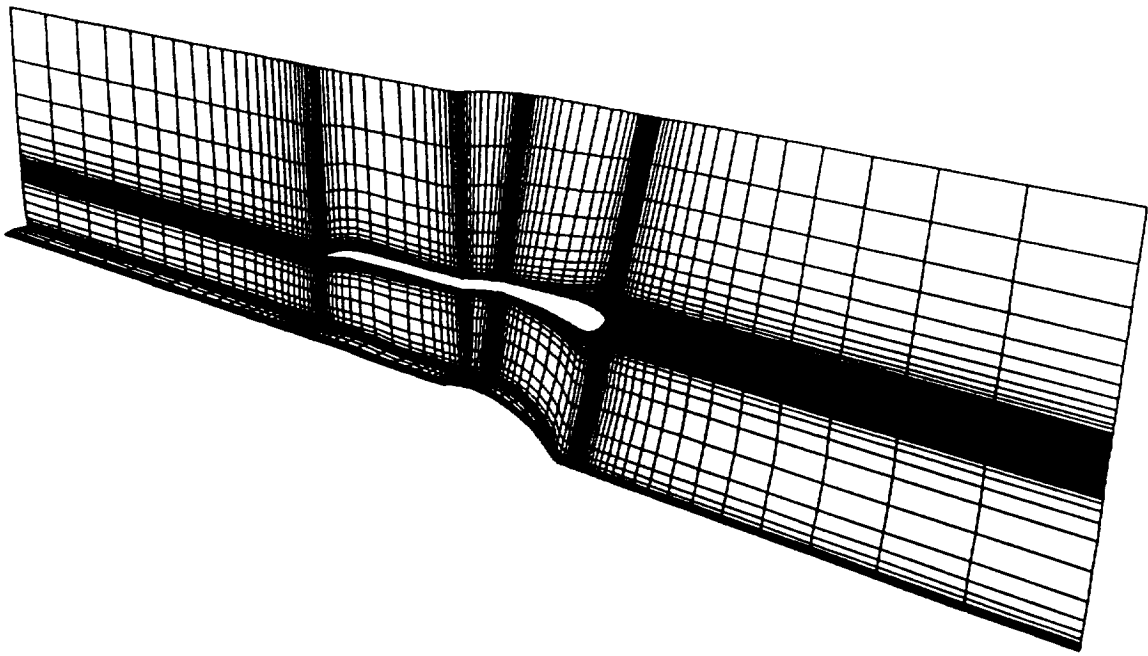


Figure 5.31: NASA 1.15 pressure ratio fan viscous flow grid system

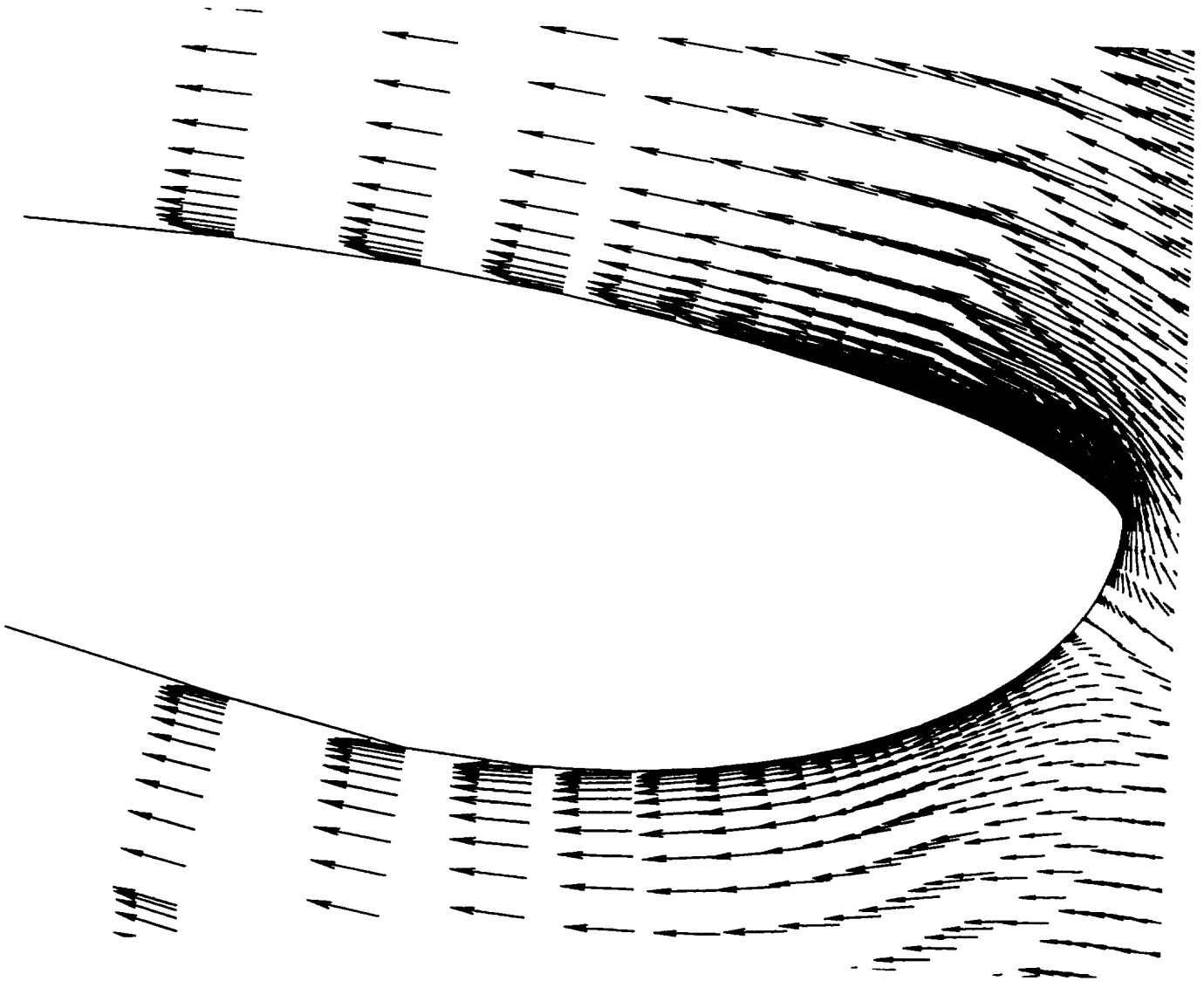


Figure 5.32: Predicted cowl surface velocity vectors in the vicinity of the outer surface shock for the NASA 1.15 pressure ratio fan stage geometry ($M=0.85$)

The full rotor numerical grid is illustrated in Fig. 5.35 and utilized 488,320 points. Relatively large grid spacings were utilized near solid surfaces to reduce the computational cost associated with the time-dependent calculation. The experimental case corresponding to this calculation was run at 120% design rotor speed, which equates to 10,992 rpm. The low flight velocity, high rotational speed, and large angle of attack all contribute to the complexity of this test case.

During the course of this test calculation, some indications of code instability due to small radius cells along the centerline upstream of the spinner leading edge were observed. These instabilities occasionally led to divergence of the solution, and should be considered an area requiring future study. Unfortunately, due to contract time and CPU time limitations, it was not possible to run this case to a time-periodic solution; however, the results are presented here for completeness.

An illustration of the instantaneous surface static pressure contours for the time-dependent solution is given in Fig. 5.36. The asymmetric loading on the spinner and cowl resulting from the highly angled freestream are clearly depicted in the color contours. A comparison of the time-averaged and unsteady blade surface static pressure ratio distribution envelopes are given in Figs. 5.37- 5.39 for 10%, 50% and 90% span, on the suction and pressure sides of the blade, respectively. The unsteady loading is seen to be largest at the hub and the tip of the blade, presumably due to the flow directing influences resulting from the proximity of the hub and cowl surfaces.

One important aspect of ducted propfan performance is the pressure recovery of the inlet duct at angle of attack. This aspect of the calculation is illustrated in the comparison of experimental and calculated fan face total pressure ratio contours

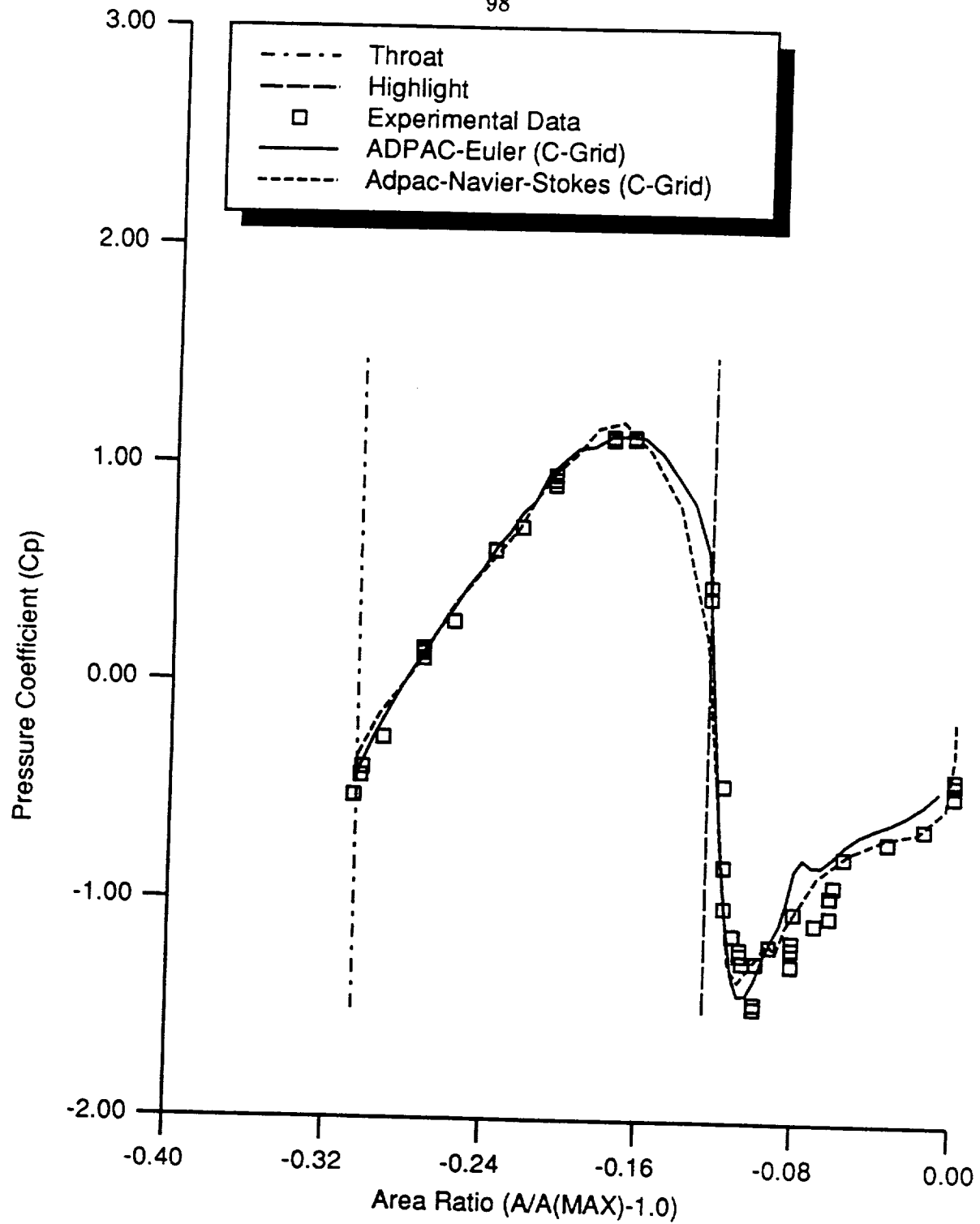


Figure 5.33: Comparison of viscous and inviscid predicted and experimental cowl surface leading edge static pressure ratio coefficient distributions for NASA 1.15 pressure ratio fan ($M=0.75$)

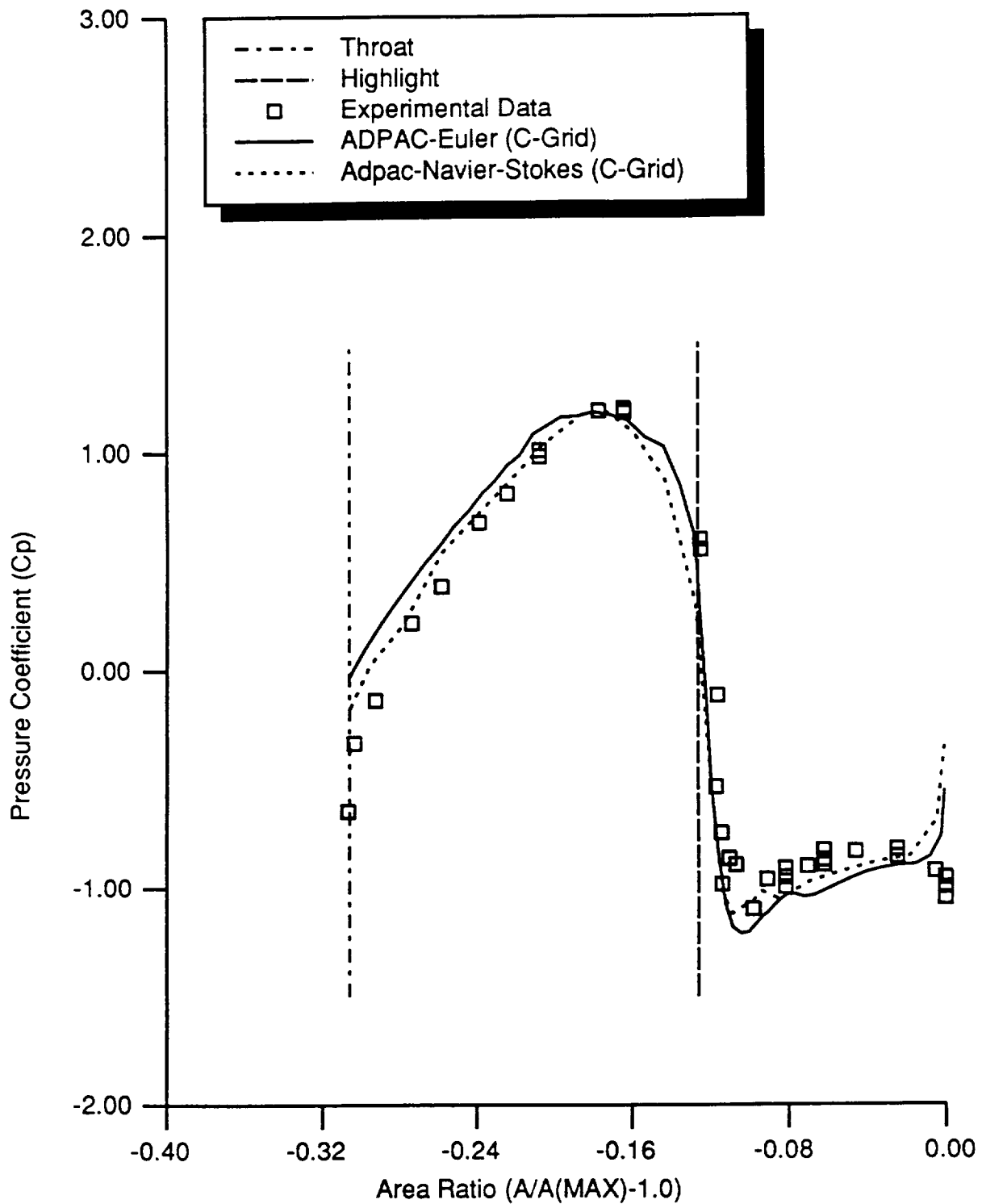


Figure 5.34: Comparison of viscous and inviscid predicted and experimental cowl surface leading edge static pressure ratio coefficient distributions for NASA 1.15 pressure ratio fan ($M=0.85$)

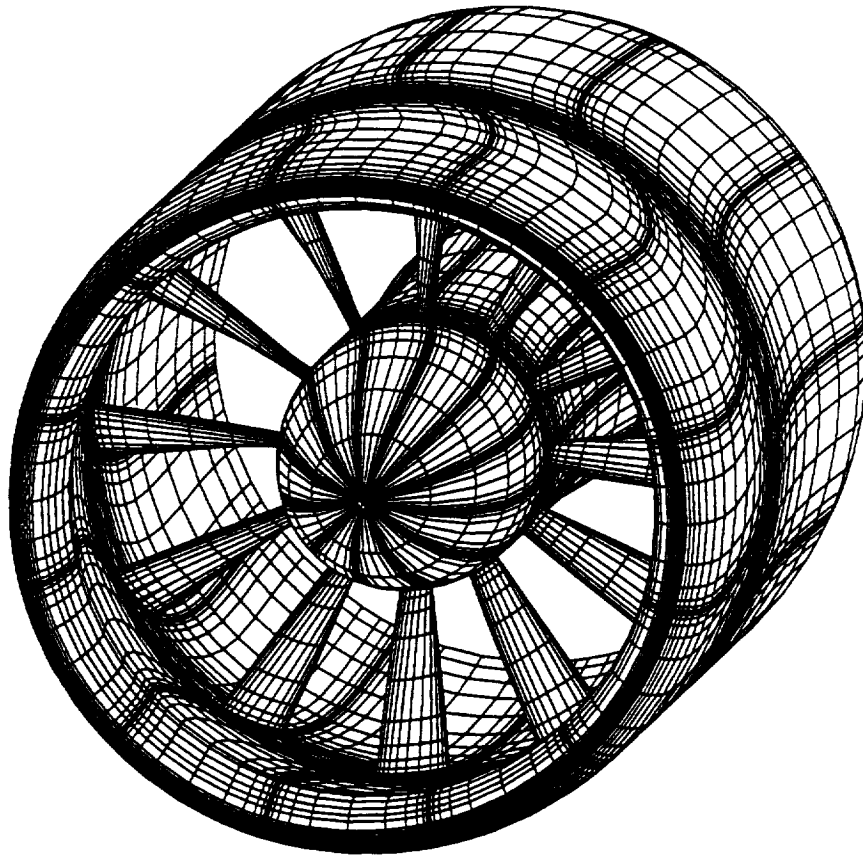


Figure 5.35: Full rotor grid system for NASA 1.15 pressure ratio fan

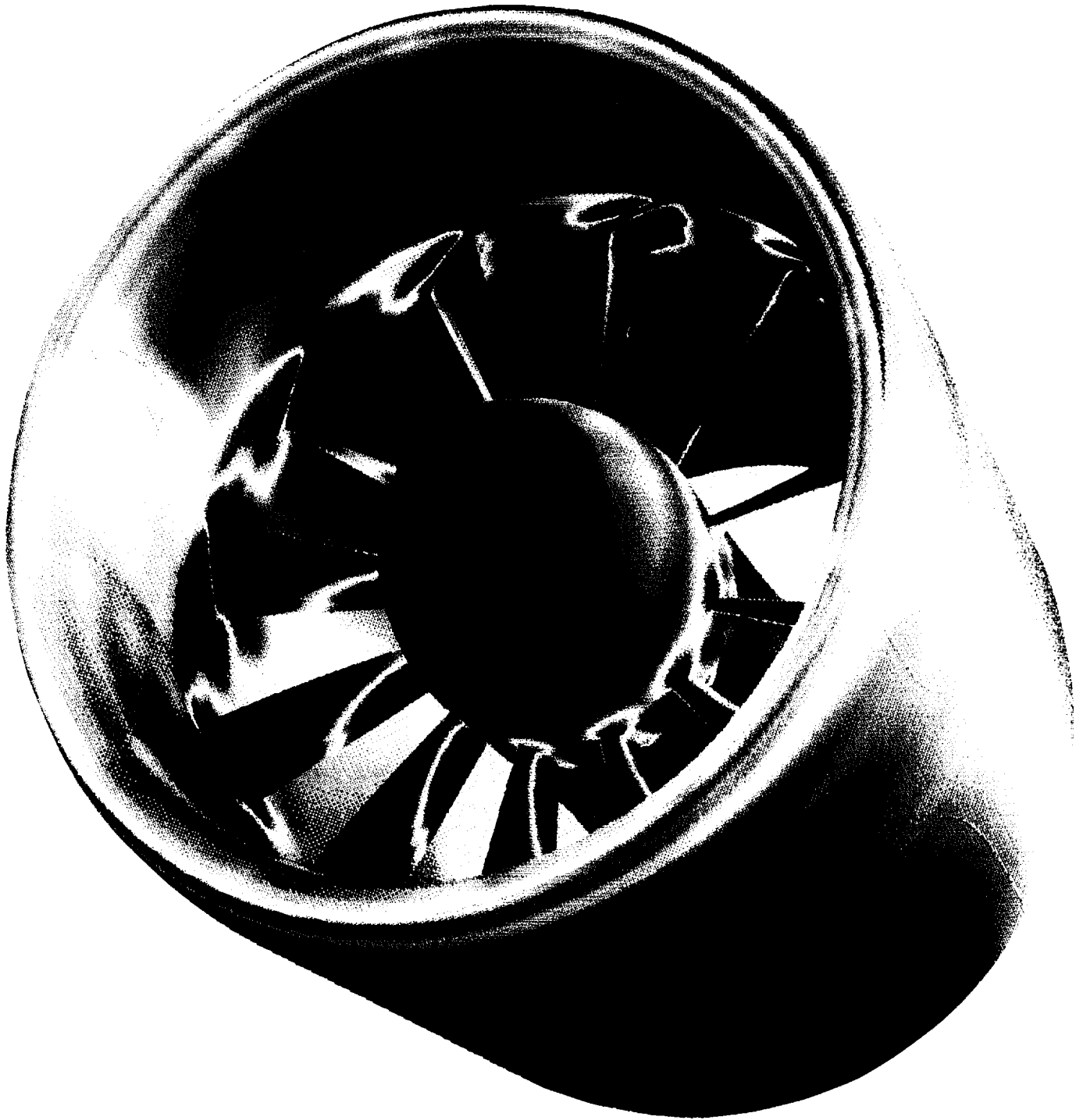


Figure 5.36: Predicted viscous instantaneous static pressure contours for NASA 1.15 pressure ratio fan at angle of attack. ($M=0.20$)

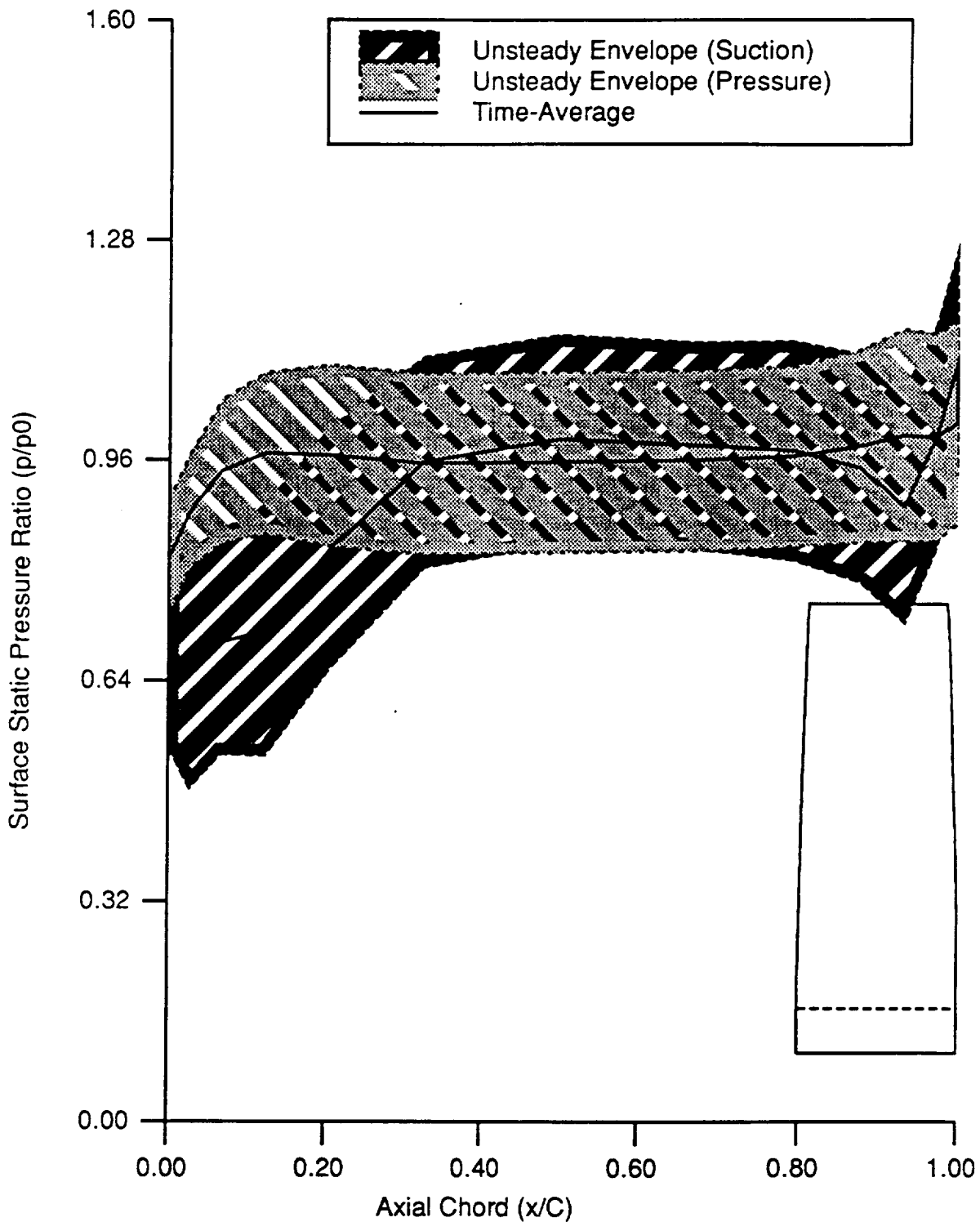


Figure 5.37: Comparison of viscous predicted time-averaged and unsteady envelope blade surface static pressure ratio distributions for NASA 1.15 pressure ratio fan at angle of attack (10% span, $M=0.20$)

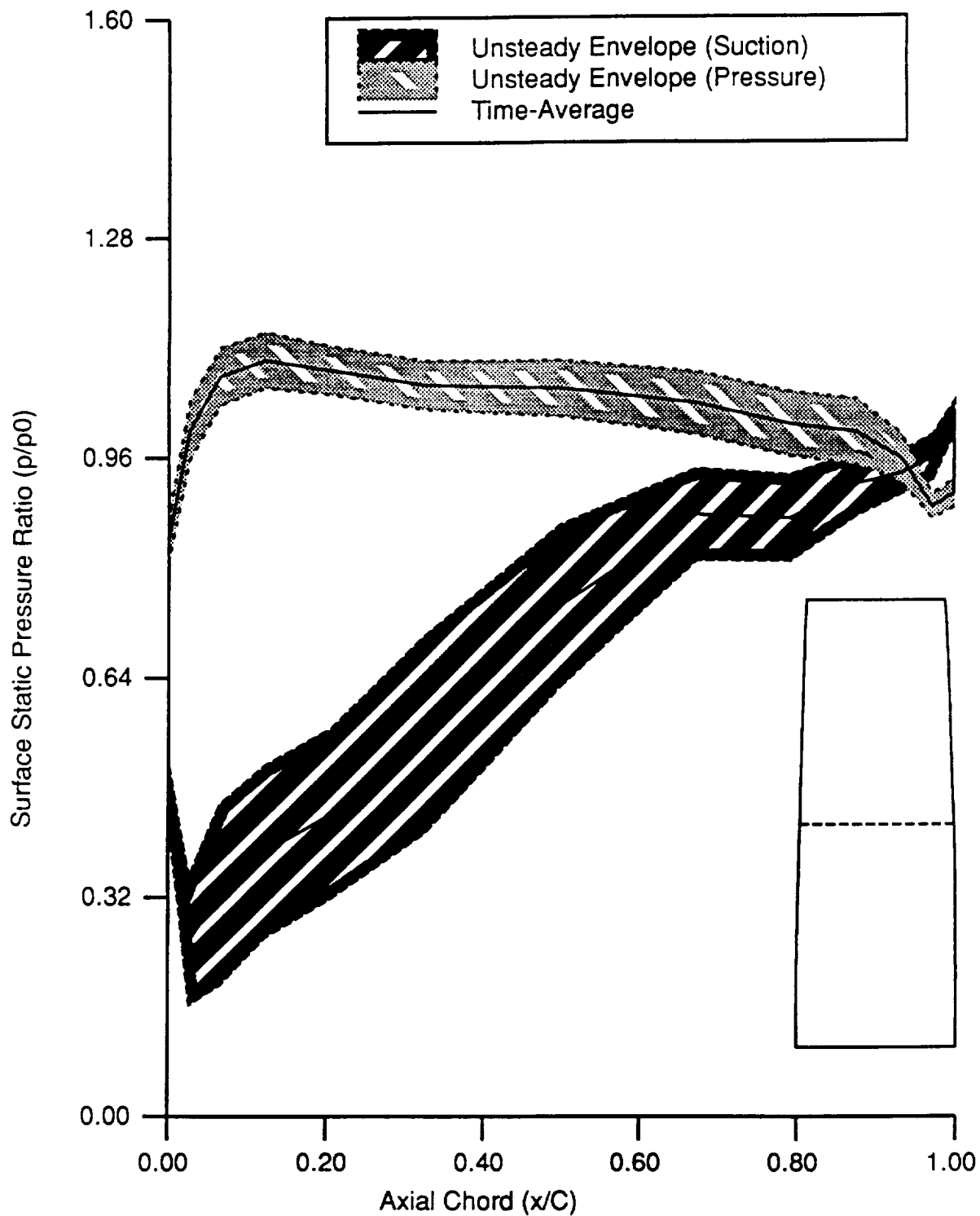


Figure 5.38: Comparison of viscous predicted time-averaged and unsteady envelope blade surface static pressure ratio distributions for NASA 1.15 pressure ratio fan at angle of attack (50% span, $M=0.20$)

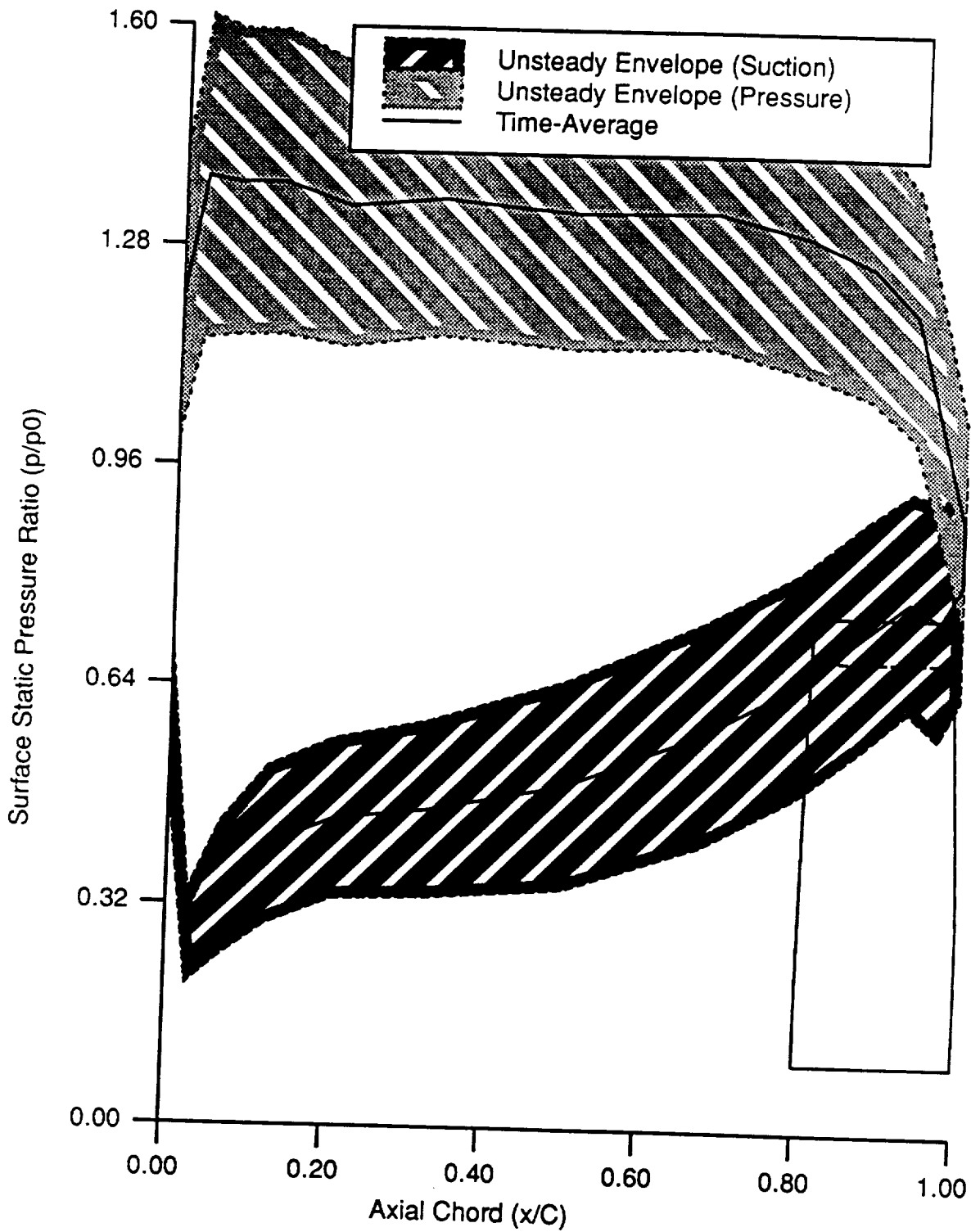


Figure 5.39: Comparison of viscous predicted time-averaged and unsteady envelope blade surface static pressure ratio distributions for NASA 1.15 pressure ratio fan at angle of attack (90% span, $M=0.20$)

given in Fig. 5.40. The experimental data for this case indicated a significant increase in inlet total pressure loss for incidence angles greater than 30 degrees. This deficiency was attributed to flow separation of the cowl internal flow, as indicated by the large decrease in total pressure on the windward side of the fan face total pressure contours in Fig. 5.40. A comparison of predicted and experimental cowl surface static/inlet total pressure distributions along the windward face of the cowl is given in Fig. 5.41. The flow separation previously discussed causes the pressure distribution to become relatively flat downstream of the highlight. This feature is evident in both experimental and predicted pressure distributions.

The results presented here illustrate the details available from predictions obtained with the *ADPAC* analysis code, and the usefulness in assessing off-design performance issues associated with ducted propfan propulsion systems operating at angle of attack.

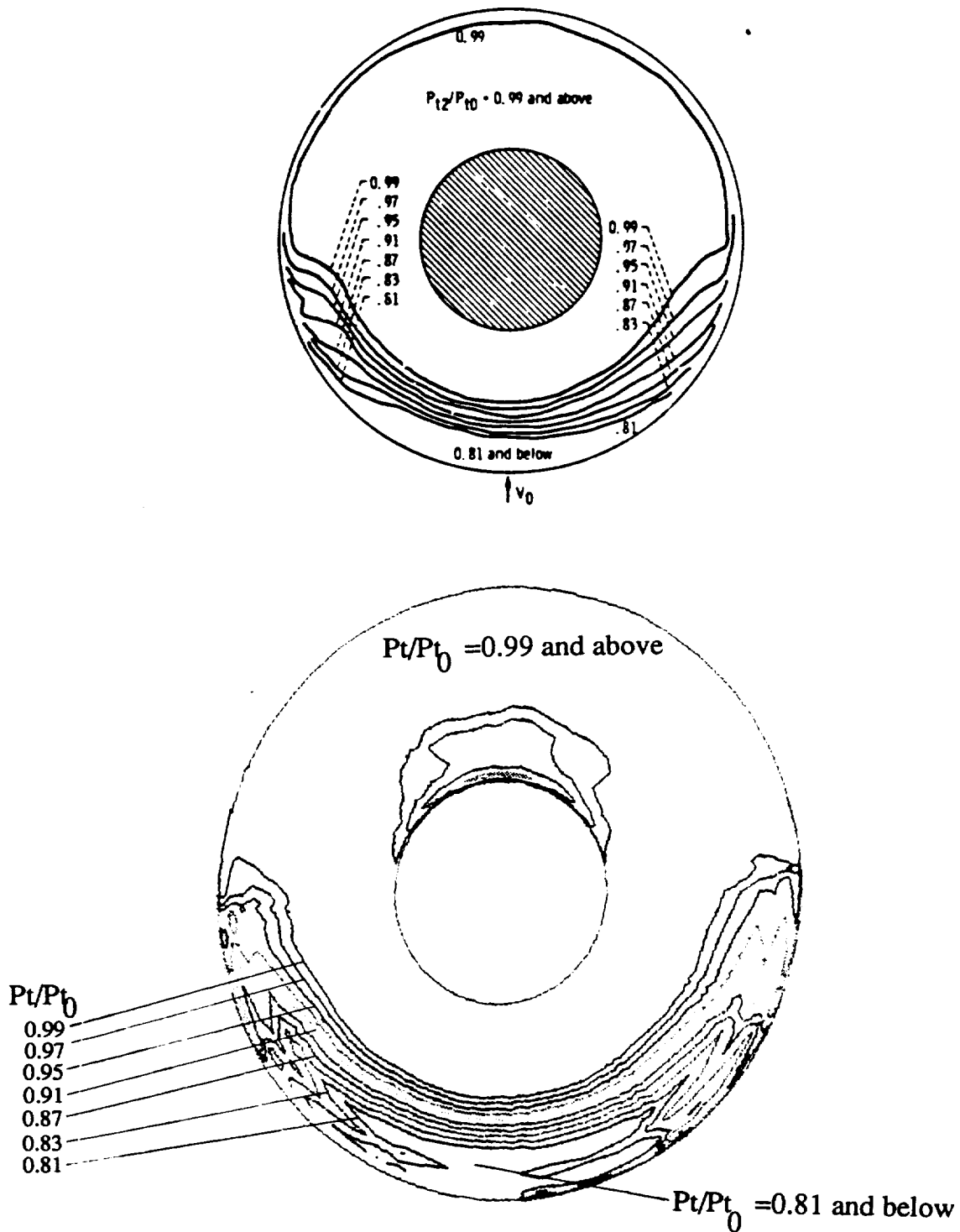


Figure 5.40: Comparison of experimental and viscous predicted instantaneous fan face total pressure ratio contours for NASA 1.15 pressure ratio fan ($M=0.2$, angle of attack = 40 degrees).

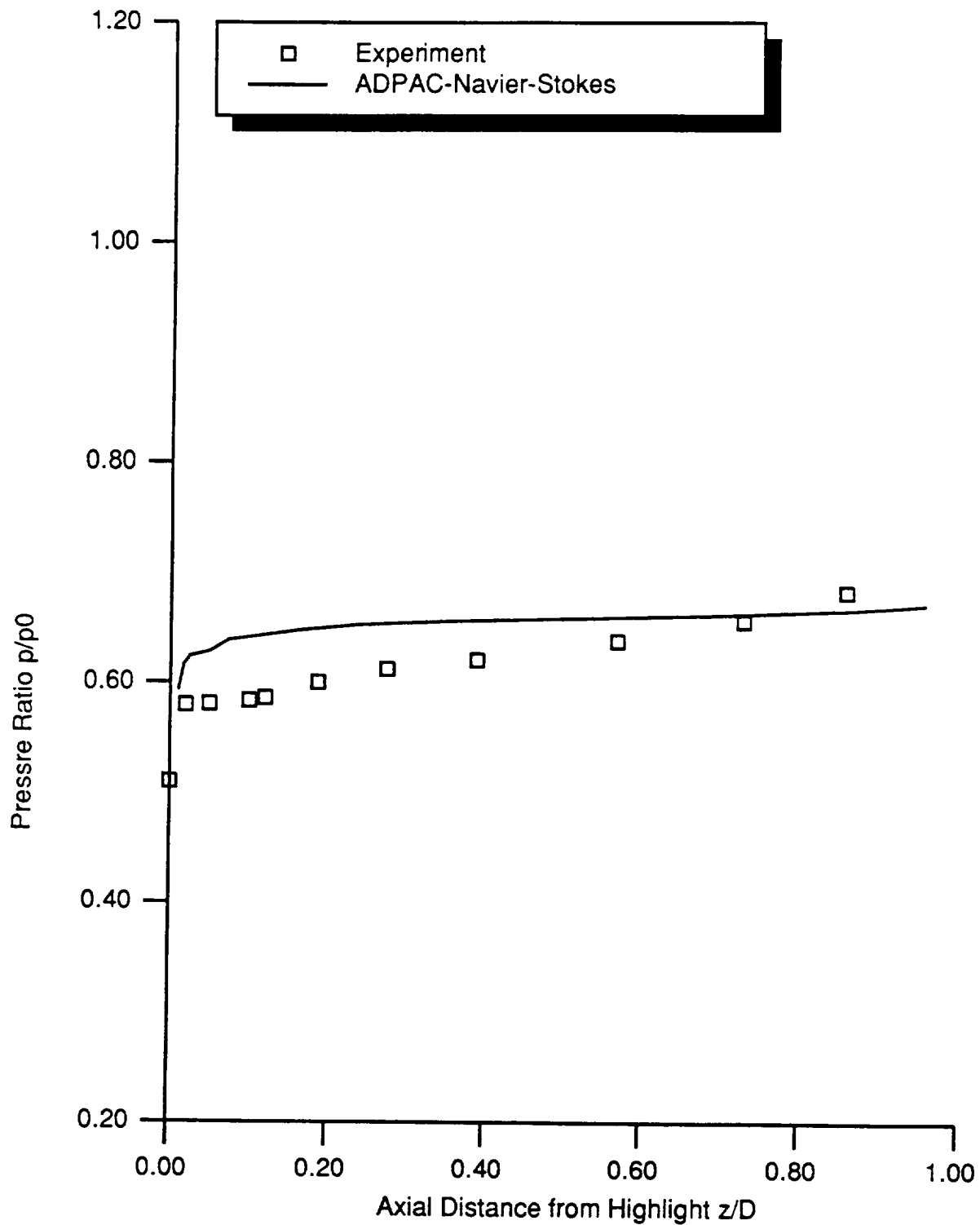


Figure 5.41: Comparison of experimental and instantaneous viscous predicted cowl windward side internal static/inlet total pressure ratio distribution for NASA 1.15 pressure ratio fan ($M=0.2$, angle of attack = 40 degrees)

6. CONCLUSIONS

A time-dependent, three-dimensional Euler/Navier-Stokes aerodynamic analysis and grid generation scheme has been developed for the numerical analysis of both ducted and unducted propfan flowfields at angle of attack. The underlying multi-block discretization scheme utilizes a single H-type grid per blade passage for unducted propfans, and a coupled system of five grid blocks utilizing an embedded C-grid about the cowl per blade passage for ducted propfans. Aerodynamic predictions were verified through comparisons with steady state and time-dependent experimental results for an advanced unducted propfan design, and a ducted 1.15 pressure ratio fan. Time-dependent calculations for single rotation propfans at angle of attack have demonstrated good agreement with experimental data and other predictions. The capability of accurately simulating the time-dependent aerodynamics about a complete ducted propfan at angle of attack has been demonstrated.

Several comments are in order concerning the various numerical techniques applied in this study. It is apparent that the simple boundary layer dissipation operator and algebraic turbulence model are not well suited for the complex vortical flows encountered in modern propfan blade designs. The time-accurate implicit residual smoothing algorithm can decidedly influence the nature of a solution when a large *CFL* number (and hence, excessive damping) is employed. The accuracy of the anal-

ysis can be swayed by additional factors, including the unknown deflected shape of the propfan blade, errors introduced through poor grid resolution, turbulence modeling, and artificial dissipation. In spite of the known algorithmic deficiencies, the analysis has successfully predicted the time-dependent flow about ducted and unducted propfans at angle of attack, and has demonstrated good agreement with available experimental data.

REFERENCES

- [1] Hager, R. D., and Vrabel, D., "Advanced Turboprop Project", NASA SP-495, 1988.
- [2] Barton, J. M., Yamamoto, O., and Bober, L. J., "Euler Analysis of Transonic Propeller Flows," *AIAA Journal*, Vol. 3, June 1987, pp. 277-282.
- [3] Usab, W. J., Lee, A. K., and Sullivan, J. P., "A Comparison of Numerical Simulation and Experimental Measurements of Flow through Propellers," AIAA Paper 88-0367, 1988.
- [4] Saito, S., Kobayashi, H., Nakamura, Y., and Matsuo, Y., "Predicted Flow Field Around the Advanced Propeller at Take-Off," AIAA Paper 88-3151, 1988.
- [5] Matsuo, Y., Arakawa, C., Saito, S., and Kobayashi, H., "Navier-Stokes Computations for Flowfield of an Advanced Turboprop," AIAA Paper 88-3094, 1988.
- [6] Kobayawa, M., and Hatano, I., "Flow Field around a Propeller by Navier-Stokes Equation Analysis," AIAA Paper 88-3150, 1988.
- [7] Celestina, M. L., Mulac, R. A., and Adamczyk, J. J., "A Numerical Simulation of the Inviscid Flow Through a Counterrotating Propeller," ASME Paper 86-GT-136, 1986.
- [8] Whitfield, D. L., Swafford, T. W., Janus, J. M., Mulac, R. A., and Belk, D. M., "Three-Dimensional Unsteady Euler Solutions for Propfans and Counter-Rotating Propfans in Transonic Flow," AIAA Paper 87-1197, 1987.
- [9] Hall, E. J., and Delaney, R. A., "3D Euler Analysis of Ducted Propfan Flowfields", AIAA Paper 90-3034-CP, 1990.

- [10] Hall, E. J., Delaney, R. A., and Bettner, J. L., "Investigation of Advanced Counterrotation Blade Configuration Concepts for High Speed Turboprop Systems: Task I - Ducted Propfan Analysis", NASA CR 185217, NASA COntact NAS3-25270, 1990.
- [11] Williams, M. H., Cho, J., and Dalton, W. N., "Unsteady Aerodynamic Analysis of Ducted Fans," (to appear in the *AIAA Journal of Propulsion and Power*).
- [12] Nallasamy, M., and Groeneweg, J. F., "Unsteady Euler Analysis of the Flow Field of a Propfan at an Angle of Attack", AIAA Paper 90-0339, 1990.
- [13] Whipple, D., "BDX-Binary Data Exchange Preliminary Information", NASA-Lewis Research Center, 1989.
- [14] Walatka, P. P., and Buning, P. G., "PLOT3D User's Manual," , rough draft for NASA TM, 1988.
- [15] Plessel, Todd, "SURF User's Guide," , NASA Ames Research Center, 1988.
- [16] Walatka, P. P., and Buning, P. G., "FAST", NASA Ames Research Center, 1990.
- [17] Mulac, R. A., "A Multistage Mesh Generator for Solving the Average-Passage Equation System," NASA CR 179539, 1988.
- [18] Brackbill, J. B., and Saltzman, J. S., "Adaptive Zoning for Singular Problems in Two Dimensions," *Journal of Computational Physics*, 46, 342-368, 1982.
- [19] Thompson, J. F., "Elliptic Grid Generation," *Numerical Grid Generation* (Edited by Joe Thompson), Elsevier Science Publishing Co., 1982.
- [20] Anderson, D. A., Tannehill, J. C., and Pletcher, R. H. , "Computational Fluid Mechanics and Heat Transfer", McGraw-Hill, New York, New York, 1984.
- [21] Hung, C. M., and Kordulla, W., "A Time-Split Finite Volume Algorithm for Three-Dimensional Flow-Field Simulation," AIAA Paper 83-1957, 1983.
- [22] Baldwin, B. S., and Lomax, H., "Thin-Layer Approximation and Algebraic Model for Separated Turbulent FLOws", AIAA Paper 78-257, 1978.

- [23] Jameson, A., Schmidt, W., and Turkel, E., "Numerical Solutions of the Euler Equations by Finite Volume Methods Using Runge-Kutta Time-Stepping Schemes," AIAA Paper 81-1259, 1981.
- [24] Jorgensen, P. C. E., and Chima, R. V., "An Unconditionally Stable Runge-Kutta Method for Unsteady Flows," NASA TM 101347, 1989.
- [25] Rao, K. V., and Delaney, R. A., 1990, "Investigation of Unsteady Flow Through a Transonic Turbine Stage: Part I- Analysis", AIAA Paper 90-2408.
- [26] Bushnell, P., "Measurement of the Steady Surface Pressure on a Single Rotation Large Scale Advanced Prop-Fan Blade at Mach Numbers from 0.03 to 0.78," NASA CR 182124, 1988.
- [27] Bushnell, P., Gruber, M., and Parzych, D., "Measurement of Unsteady Blade Surface Pressure on a Single Rotation Large Scale Advanced Prop-Fan with Angular and Wake Inflow at Mach Numbers from 0.02 to 0.70", NASA CR-182123, NASA Contract NAS3-23051, 1988.
- [28] Steffen, F. W., "Cruise Performance of an Isolated 1.15 Pressure Ratio Turbofan Propulsion Simulator at Mach Numbers from 0.6 to 0.85," NASA TM X-3064, 1974.
- [29] Wesoky, H. L., Abbott, J. M., Albers, J. A., and Dietrich, D. A., "Low-Speed Wind Tunnel Tests of a 50.8 Centimeter (20-in.) 1.15 Pressure Ratio Fan Engine Model," NASA TM X-3062, 1974.
- [30] Wesoky, F. L., and Steffen, F. W., "Wind Tunnel Tests of a 20 in. Diameter 1.15 Pressure Ratio Fan Engine Model," NASA TM X-71445, 1973.
- [31] Osborn, W. M., and Steinke, R. J., "Performance of a 1.15 Pressure-Ratio Axial-Flow Fan Stage with a Blade Tip Solidity of 0.5," NASA TM X-3052, 1974.

APPENDIX A. ADPAC DISTRIBUTION LIST

ADPAC DISTRIBUTION LIST

NASA Contract NAS3-25270

Task Order #2

User's Manual CR-187105

Final Report CR-187106

GOVERNMENT AGENCIES:

NASA Headquarters
600 Independence Avenue, SW
Washington, DC 20546

Attn: RJ/C. C. Rosen
RP/S. Wander
RP/J. R. Facey

NASA Lewis Research Center
21000 Brookpark Road
Cleveland, OH 44135

Attn: J. J. Adamczyk	M.S. 5-9	(2 copies)
C. L. Ball	M.S. 86-1	
L. J. Bober	M.S. 77-6	
D. R. Boldman	M.S. 86-7	
B. Clark	M.S. 77-6	
R. W. Claus	M.S. 142-5	
J. H. Dittmar	M.S. 77-6	
J. F. Groeneweg	M.S. 77-6	(2 copies)
C. E. Hughes	M.S. 77-6	
R. J. Jeracki	M.S. 77-6	
C. M. Kim	M.S. 77-6	
J. Lytle	M.S. AAC-1	

A. J. Mahajan	M.S. 23-3	
C. J. Miller	M.S. 77-6	(15 copies)
D. P. Miller	M.S. 77-6	
R. D. Moore	M.S. 77-6	
L. D. Nichols	M.S. 142-5	
C. W. Putt	M.S. 142-2	(2 copies)
D. R. Reddy	M.S. 5-11	
T. S. Reddy	M.S. 23-3	
R. Srivastava	M.S. 23-3	
G. L. Stefko	M.S. 23-3	
R. P. Woodward	M.S. 77-6	
J. A. Ziemianski	M.S. 86-1	
Report Control Office	M.S. 60-1	(4 copies)
Tech. Utilization Office	M.S. 7-3	
AFSC Liaison Office	M.S. 501-3	

NASA Ames Research Center
Moffett Field, CA 94035

Attn: Library M.S. 202-3

NASA Langley Research Center
Hampton, VA 23665

Attn: F. Farassat	M.S. 461
M. H. Dunn	M.S. 904
Library	M.S. 185

NASA Scientific and Technical Information Facility
P.O. Box 8757
BWI Airport, MD 21240

Attn: Accession Dept. (6 copies and the FF427 form)

Sverdrup Technology, Inc.
2001 Aerospace Parkway
Brookpark, OH 44142

Attn: J. Bridges	M.S. 77-6
E. Envia	SVR-3
R. M. Nallasamy	SVR-3
S. M. Ramachandra	SVR-3
O. Yamamoto	SVR-3

ENGINE MANUFACTURERS

Allison Gas Turbine Division, GMC Corp.
 P.O. Box 420
 Indianapolis, IN 46206-0420

Attn: (Handled internally at AGT.)

General Electric Company
 Aircraft Engine Group
 1 Neumann Way
 Evendale, OH 45215

Attn: P. Gliebe	Mail Drop A-304
C. Lenhardt	Mail Drop A-330
M. Majjigi	Mail Drop A-319
M. Pearson	Mail Drop A-317
L. Smith	Mail Drop H-4
C. Whitfield	Mail Drop A-304

Hamilton Standard Division - UTC
 Windsor Locks, CT 06096

Attn: D. B. Hanson	M.S. 1A-3-6
F. B. Metzger	M.S. 1A-3-6

Pratt & Whitney Aircraft - UTC
 Commercial Products Division
 400 Main Street
 East Hartford, CT 06108

Attn: D. Hopwood	M.S. 162-07 (3 copies)
D. Mathews	M.S. 165-11
W. Lord	M.S. 169-23
T. Wynosky	M.S. 169-23

United Technologies Corporation Research Center
 Silver Lane
 E. Hartford, CT 06108

Attn: M. Barnett	M.S. 20
R. Davis	M.S. 20
D. Dorney	M.S. 20

AIRFRAME MANUFACTURERS

Boeing Commercial Airplane Company (BCAC)

P.O. Box 3707

Seattle, WA 98124-2207

Attn: B. W. Farquhar

M.S. 0L-22

W-H. Jou

M.S. 7H-96

R. Cuthbertson

M.S. 79-84

Douglas Aircraft Company Division

McDonnell Douglas Corporation

3855 Lakewood Blvd.

Long Beach, CA 90846

Attn: M. Joshi

M.S. 36-60

F. Lynch

M.S. 36-60

G. Page

M.S. 35-86

W. Siegele

M.S. 202-15

General Dynamics Convair

P.O. Box 80844

San Diego, CA 92138

Attn: B. Bergman

M.Z. 36-1240

S. Strande

M.Z. 55-6950

K. Taylor

M.Z. 54-6890

UNIVERSITIES

Georgia Institute of Technology

School of Aerospace Engineering

Atlanta, GA 30332-0800

Attn: Dr. L. N. Sankar

Lockheed-California Company

P.O. Box 551

Burbank, CA 91520

Attn: Library

Ohio State University

Department of Aeronautical

and Astronautical Engineering

Columbus, OH 43220

Attn: Prof. G. M. Gregorek

Pennsylvania State University
Department of Aerospace Engineering
233 Hammond Building
University Park, PA 16802

Attn: Dr. B. Lakshminarayana

Purdue University
School of Aeronautics and Astronautics
W. Lafayette, IN 47907

Attn: Dr. J. P. Sullivan
Dr. M. Williams

Purdue University
School of Mechanical Engineering
W. Lafayette, IN 47907

Attn: Dr. S. Fleeter

Rohr Industries, Inc.
P.O. Box 878
Chula Vista, CA 92012-0878

Attn: Library

Texas A&M University
Aerospace Engineering Department
College Station, TX 77843-3141

Attn: Dr. K. D. Korkan

University of Arizona
Aerospace and Mechanical Engineering Department
Aero Building #16
Tucson, AZ 85721

Attn: Dr. E. J. Kerschen

University of Missouri-Rolla
Mechanical Engineering Department
Rolla, MO 65401-0249



Report Documentation Page

1. Report No. NASA CR-187106		2. Government Accession No.		3. Recipient's Catalog No.	
4. Title and Subtitle Investigation of Advanced Counterrotation Blade Configuration Concepts for High Speed Turboprop Systems, Task II - Unsteady Ducted Propfan Analysis (Final Report)			5. Report Date May 1991		
			6. Performing Organization Code		
7. Author(s) Edward J. Hall Robert A. Delaney James L. Bettner			8. Performing Organization Report No.		
			10. Work Unit No. 535-03-10		
9. Performing Organization Name and Address Allison Gas Turbine Division General Motors Corporation P.O. Box 420 Indianapolis, IN 46206-0420			11. Contract or Grant No. NAS3-25270		
12. Sponsoring Agency Name and Address National Aeronautics and Space Administration Lewis Research Center Cleveland, OH 44135-3191			13. Type of Report and Period Covered Contractor Report Final		
			14. Sponsoring Agency Code		
15. Supplementary Notes Prepared in cooperation with NASA Project Manager Christopher J. Miller, NASA Lewis Research Center, Cleveland, OH					
16. Abstract <p>The primary objective of this study was the development of a time-dependent three-dimensional Euler/Navier-Stokes aerodynamic analysis to predict unsteady compressible transonic flows about ducted and unducted propfan propulsion systems at angle of attack. The computer codes resulting from this study are referred to as Advanced Ducted Propfan Analysis Codes (ADPAC). This report is intended to serve as a computer program user's manual for the ADPAC developed under Task II of NASA Contract NAS3-25270, Unsteady Ducted Propfan Analysis.</p> <p>Aerodynamic calculations were based on a four-stage Runge-Kutta time-marching finite volume solution technique with added numerical dissipation. A time-accurate implicit residual smoothing operator was utilized for unsteady flow predictions. For unducted propfans, a single H-type grid was used to discretize each blade passage of the complete propeller. For ducted propfans, a coupled system of five grid blocks utilizing an embedded C-grid about the cowl leading edge was used to discretize each blade passage. Grid systems were generated by a combined algebraic/elliptic algorithm developed specifically for ducted propfans. Numerical calculations were compared with experimental data for both ducted and unducted propfan flows. The solution scheme demonstrated efficiency and accuracy comparable with other schemes of this class.</p>					
17. Key Words (Suggested by Author(s)) Euler Navier-Stokes Ducted Propfan			18. Distribution Statement Unclassified-Unlimited		
19. Security Classif. (of this report) Unclassified		20. Security Classif. (of this page) Unclassified		21. No. of pages	
				22. Price	

